Effective Medium Approximations For Light Scattering by Heterogeneous Particles

by

I Wayan Sudiarta

Submitted in partial fulfillment of the requirements
for the degree of Doctor of Philosophy

at

Dalhousie University
Halifax, Nova Scotia
2003

DALHOUSIE UNIVERSITY

FACULTY OF GRADUATE STUDIES

The undersigned hereby certify that they have read and recommend to the Faculty of Graduate Studies for acceptance a thesis entitled "Effective Medium Approximations For Light Scattering by Heterogeneous Particles" by I. Wayan Sudiarta in partial fulfillment for the degree of Doctor of Philosophy.

Dated: March 25, 2003

External Examiner:

Research Supervisors:

Examining Committee:

Departmental Representative:

DALHOUSIE UNIVERSITY

DATE: April 03, 2003

AUTHOR: I Wayan Sudiarta

TITLE: "Effective Medium Approximations for Light Scattering by Heterogeneous Particles"

DEPARTMENT: Physics and Atmospheric Science

DEGREE: Ph.D.

Permission is herewith granted to Dalhousie University to circulate and to have copied for non-commercial purposes, at its discretion, the above title upon the request of individuals or institutions.

Signature of Author

To my parents,

I N. Rusta and Ni K. Merni

For all the love I received.

Terima Kasih

In memory of my grandfather, I K. Jata

Contents

List of Tables

List of Figures

Abstract

Atmospheric particles, such as aerosols, have a wide range of sizes, shapes, and compositions. It is difficult to determine the single scattering properties of an aerosol taking account of all its possible physical properties. A numerical method, known as the finite difference time domain (FDTD) method, can be used for this purpose. However, because aerosol compositions are complicated, the effective medium approximation (EMA) is usually employed. In this thesis, various EMAs are discussed and numerically tested using the FDTD method. A composite particle modeled by a spherical particle with multiple spherical inclusions is used to test the EMAs. It is found that the applicability of the EMAs depends on the physical properties, the spatial arrangement, and the number of the inclusions inside the host sphere. It is found that the Bruggeman and the quasi-crystalline approximation with coherent potential and Percus-Yevick (PY) pair distribution (QCA-CP-PY) mixing rules show better accuracy than other analytical EMAs for an inclusion size much smaller than the wavelength and for a volume fraction less than 10%. For a larger inclusion, the extended Bruggeman method and the QCA-CP-PY give more accurate results. When only one inclusion is inside the host sphere, the extended Maxwell-Garnett is more accurate. Effective refractive indices obtained from the Bruggeman mixing rule show a good agreement with the FDTD results for very small inclusions. For a larger inclusion, a combination of Bruggeman and the Maxwell-Garnett mixing rules shows a good agreement.

Atmospheric particles may be found in an absorbing atmospheric medium. In the past the light scattering by a particle in a non-absorbing medium is generally considered. The simplest shape for approximating an atmospheric particle is a sphere. A new formulation of light scattering by a spherical particle (the Mie theory) in an absorbing medium is also presented. Numerical results show that the absorbing medium can affect the single scattering properties only for large particles or in highly absorbing host media. For atmospheric applications, the effect is generally small and therefore can be neglected.

List of Symbols

<> : a spatial averaging

a : radius of a sphere

a_n, b_n, c_n, d_n : scattering coefficients

α : angle in Higdon's operator

α_c : polarizability of a cube

α_j, β_j : MAS parameters

A_n, B_n : coefficients in the coated sphere scattering coefficients

ABC: absorbing boundary condition

β is nonnegative number introduced to ensure stability in the Higdon's operator

B : magnetic induction

BR: Bruggeman mixing rule

c : speed of wave in a medium

$\delta(t)$: the Dirac delta function.

Δt : a temporal increment.

$\Delta x, \Delta y, \Delta z, \Delta s$: spatial increments

D : electric displacement

DDA: discrete dipole approximation

D_x, D_y, D_z, D_t : operators $\partial/\partial x$, $\partial/\partial y$, $\partial/\partial z$, and $\partial/\partial t$

$\mathbf{E}$: electric field vectors

EMA: effective medium approximation

$E_n = i^n(2n+1)E_0 / n(n+1)$

$\mathbf{E}_1, \mathbf{H}_1$: electric field and magnetic field inside a sphere

$\mathbf{E}_2, \mathbf{H}_2$: electric field and magnetic field outside a sphere

ε : permittivity of a medium

ε_c : permittivity of a cubic material

ε_h : dielectric constant of a host medium

ε_{eff} : dielectric constant of effective medium

ε_h : dielectric constant of inclusion medium

EBR: Extended Bruggemann mixing rule

EFA: effective field approximation

EMG: Extended Maxwell-Garnett mixing rule

f_n : field in time domain at time step n

f_1, f_2 : volume fraction of medium 1 and medium 2

$F(\omega)$: field in frequency domain

FDTD: finite difference time domain

g : asymmetry factor

$\mathbf{H}$: magnetic field vectors

$H_{\min}, H_{\max}$: minimum and maximum height of an atmospheric layer

I : intensity of incident field

I, J, K : grid indices

Im : imaginary part of

IMG: inverted Maxwell-Garnett mixing rule

$j_n(\rho)$: spherical Bessel functions of first kind of order n

$\mathbf{J}_m$: equivalent magnetic current

$\mathbf{J}_e$: free electric current.

$J(T)$: a radiance source term

$k_{0,I}$: imaginary part of wave number k_0 in host medium.

$k_x = k_{x,re} + ik_{x,im}$: $k_{x,re}$ and $k_{x,im}$ are real and imaginary parts.of a wave number.

$k_0 = 2\pi m_{med}/\lambda$: wave number in medium

$k_1 = 2\pi m_{sph}/\lambda$: wave number in spherical particle

λ : wavelength in vacuum

L_z^+, L_z^- : OWWE operators for wave travelling in positive and negative z direction.

LBL : line by line

μ : permeability of a medium

μ_0, μ : cosines of solar and observer zenith angles respectively

m_r : complex relative refractive index of spherical particle

m_{sph} : refractive indices of a sphere

m_{med} : refractive indices of the host medium

M1, M2, M3, M1&3: EMA based on numerical methods

MG: Maxwell-Garnett mixing rule

$\mathbf{M}$, $\mathbf{N}$: vector spherical harmonic functions

$n_j = f_j/(\frac{4}{3}\pi R_j^3)$: number concentration of the jth sphere (radius R_j).

OWWE: one way wave equation

ω : angular frequency,

P_n^1 is the associated Legendre function of first kind of degree n and order 1.

p, q, r : coefficients for approximating function

PML: perfectly matched layer

PY: Percus-Yevick pair distribution function

$\psi_n(\rho)$, $\psi_n'(\rho)$, $\xi_n(\rho)$ and $\xi_n'(\rho)$: Riccati-Bessel functions and their derivatives with respect to the argument ρ,

$\pi_n(\cos(\theta)) = P_n^1(\cos(\theta))/\sin(\theta)$: Legendre function

ϕ : solar azimuth angle

$Q = W / I\pi a^2$: efficiency

QCA: quasi-crystalline approximation

QCA-CP: QCA with coherent potential

QCA-CP-PY: QCA-CP with Percus-Yevick pair distribution.

R_1 and R_2 : radii of sphere 1 and 2

Re : real part of

$R(0^o)$: normal reflectance

$r_{m,j}$: mean radius of polydisperse particles

ρ : free electric charge

σ : electric conductivity of a medium

$\sigma = W / I$: cross section

σ_{ext} , σ_{sca} , σ_{abs} : extinction, scattering, absorption cross sections or coefficients

σ_m : equivalent magnetic conductivity of a medium

$S(0)$: total forward scattering amplitudes

S_{11} : phase matrix

$\tau_n(\cos(\theta)) = \mathrm{d}P_n^1(\cos(\theta))/\mathrm{d}\theta$: Legendre function

$T(+)$, $T(-)$: transmission of a wave travelling in the positive and negative x direction.

UEBR: Uncorrected Bruggemann mixing rule

UEBR: Uncorrected Extended MG

$W_{ext}, W_{sca}, W_{abs}$: net rate of the extinct, scattered, absorbed energy by a sphere

$x = k_0 a$: size parameter

$\xi_n(\rho) = \rho(j_n(\rho) + iy(\rho))$: Riccati-Bessel functions

$y_n(\rho)$: spherical Bessel functions of second kind of order n.

Acknowledgements

I would like to thank especially to Dr. Petr Chýlek. I am grateful for his supervision, guidance, understanding some of my situations, providing support and a wide range of ideas. Special thanks to Dr. Ulrike Lohmann, Dr. Ian Folkins, and Dr. John Cordes for reading of my thesis and for giving many helpful comments and suggestions. I am indebted to Dr. Glen Lesins for much help and suggestions during my research. I also thank Dr. Wally Geldart for reading my thesis and letting me borrow his books which helped me developed some ideas for my thesis.

Many thanks to Xiaobo Chen for his support and friendship during the PhD program. I would like to thank also all the people in the Department of Physics and Atmospheric Science at Dalhousie University for providing an excellent atmosphere and hospitality. Many thanks to the late Gloria Tweedy, Barbara Gauvin, Judith Hollett, Bridget Trim, Anne Murphy, and Anne-marie Jeffrey for providing some administrative support and much help during my studies.

I would like to thank all the people that supported me while studying in Halifax, N.S., Canada, especially to Sila Dharma's family, Herawaty Abbas, Yusran, Melati Cahyono, Angella, Ibnu's family, Aries's Family, Tomoko, Rukmi's family and many others. Thanks to G. Mandia's family for their hospitality during my stay in Lombok, Indonesia.

I would like to thank my parents, I N. Rusta and K. Merni, my brother and sisters, N. Sumiarta, N. Suci and K.B. Juniasti, for all the encouragement to work on my thesis and for understanding many problems I faced during the process of my study and also in life. I would like to thank Putu Utami for her patient, support, encouragement, and help during my studies and the writing process of my thesis.

Chapter 1

Introduction

Solar radiation is mainly in the form of short wave radiation with wavelengths less than 3 μm. Its spectrum indicates a temperature of about 6000 K. The amount of solar radiation received by the Earth is dependent on how much radiation is absorbed and reflected (or scattered) by the Earth's surface and atmospheric constituents. Some of the absorbed radiation is then re-emitted by the Earth's surface and the atmosphere in the form of long wave radiation (wavelengths larger than 3 μm).

Atmospheric particles such as aerosols play significant roles in reflecting and absorbing short wave and long wave radiation. There are two contributions of the aerosols that can affect the Earth's climate. The aerosols can directly modify the incoming solar and outgoing long wave radiation by scattering and absorption processes. This is known as the direct effect of aerosols (Seinfeld and Pandis, 1998). The aerosols can also affect the climate indirectly by modifying the properties of cloud droplets in which the aerosols play as cloud condensation nuclei (Seinfeld and Pandis, 1998; Pruppacher and Klett, 1997).

The effect of aerosols on climate is usually assessed by the radiative forcing of aerosols, which is defined as the change in solar irradiance absorbed by the surface-

atmosphere system due to the presence of aerosols (Kiehl and Rodhe, 1995). The radiative forcing of aerosols can be positive or negative depending on the optical properties of aerosols. These properties are affected by the geometrical shape, size distribution, chemical composition and refractive index of aerosols. These properties can be modified further when the aerosols are hygroscopic. In this case the aerosols can take up water and grow in size with increasing relative humidity (Pruppacher and Klett, 1997).

One important type of aerosols is the carbonaceous aerosols. These aerosols are mainly produced by anthropogenic activities. They are comprised of two classes of materials, black carbon (soot) and organic carbon. The black carbon is produced by the incomplete combustion of fossil fuel and biomass burning (Seinfeld and Pandis, 1998). The organic carbon is produced by combustion and natural sources, or may be also by gas-to-particle conversion of hydrocarbons (Seinfeld and Pandis, 1998). The organic carbon particles are mainly scattering (Seinfeld and Pandis, 1998), whereas the black carbon particles are mainly absorbing (Horvath, 1993).

Because of the absorbing nature of black carbon, it contributes mainly to a positive radiative forcing and consequently to a net heating of the atmosphere (Horvath, 1993). The radiative properties of aerosols are sensitive to how different aerosol components are externally or internally mixed (Lesins et al., 2002). Black carbon may exist in the form of several mixing states, but there are only three mixing states commonly used: (a) the black carbon is completely separated from other aerosol particles (external mixture), (b) the black carbon is embedded in other aerosols (internal mixture) and (c) the black carbon is a core with a coating shell of other aerosol species (Jacobson, 2001). Consequently the radiative forcing of the black carbon is also sensitive to the aerosol mixing states. It is known that the internal mixture gives a higher radiative forcing than the external mixture. In a study by Haywood and Boucher (2000), the radiative forcing for fossil fuel black carbon is estimated by $+0.16\ \mathrm{W/m^2}$ for external mixture and $+0.42\ \mathrm{W/m^2}$ for internal mixture with sulfate aerosol. The value of radiative forcing for a core with coating shell model of aerosols is in between those of the external and internal mixtures (Jacobson, 2000, Lesins, 2002). In a recent study, Jacobson (2001) simulated the evolution of the chemical composition of aerosols. This author found that the mixing state and radiative

forcing of the black carbon component are close to those of the internal mixture. Therefore it is important to study the optical properties of the internally mixed aerosols.

To determine the optical properties of internally mixed aerosol and consequently its radiative forcing, the problem of light scattering by a particle with inclusions needs to be solved. This is a complicated problem. The properties of inclusions could complicate finding an analytical solution. Many researchers have developed analytical solutions for a spherical particle with spherical inclusions or with irregular inclusions (Fikioris & Uzunoglu, 1979; Fuller, 1995; Borghese et al., 1992; Ioannidou and Chrissoulidis, 2002; Videen et al., 1995). For this problem, the finite difference time domain (FDTD) method, the discrete dipole approximation (DDA) and the extended boundary condition method (EBCM) may also be used. It is generally considered to be impossible to calculate a large set of particles with various compositions. Therefore an approximate method to estimate the light scattering properties of composite particles is needed. Such an approximate method is the effective medium approximation (EMA). If the size of inclusions is on average small compared to the incident wavelength, it is possible to treat the particle as homogenous. Therefore, the optical properties of a composite particle can be replaced by optical properties of a homogenous particle.

In all the radiative forcing studies, it is assumed that an internally mixed aerosol can be modeled by a homogeneous sphere with appropriate effective refractive index. It is common to obtain the effective refractive index by simply taking the volume-weighted average of refractive indices of the aerosol components (Haywood et al. 1997; Myhre et al.,1998; Seinfeld and Pandis, 1998). Other EMAs, such as the Bruggeman and the Maxwell-Garnett mixing rules (see e.g. Chýlek et al.(2000)), may also be used for this purpose. Depending on the choice of EMA, one could obtain different optical properties of internally mixed aerosols.

It is uncertain which of the EMAs provide the accurate optical properties of internally mixed aerosol. Various experiments and numerical tests for the applicability of the EMAs for atmospheric applications were reported by several researchers (Chylek et al., 1988 and 2000; Doicu & Wriedth, 2001; Kolokolova & Gustafson, 2001). However, further tests are still needed to determine which of the EMAs is appropriate for estimating the effective refractive indices of aerosol. Motivated by this need, various EMAs are

developed and examined in this thesis. For this study the FDTD method is developed and used to test the EMAs. In this thesis, to enhance differences in the values of the effective refractive indices obtained from various EMAs, a mixture of ice and water at 3.21 cm wavelength is considered. The refractive indices of water and ice are $m_w = 7.14 + 2.89i$ and $m_{ice} = 1.78 + 0.0024i$ respectively. The water is highly absorbing and the ice has a small imaginary part of refractive index, hence it can be considered non-absorbing. For a black carbon – sulfate mixture, we have a black carbon (absorbing material) is mixed inside a sulfate (non-absorbing) particle. Therefore a model of an ice sphere with multiple spherical water inclusions is considered here. Using the FDTD method the optical properties of this sphere are obtained and then compared with the optical properties calculated using the Mie theory with effective refractive indices obtained from various EMAs.

By testing a wide variety of EMAs, it is hoped that criteria can be determined for selecting the most appropriate EMAs for a particular application. The choice of the most appropriate EMAs requires consideration of the physical properties of the heterogeneous particle in question. It is expected that some EMAs may be accurate for only a particular structure of the heterogeneous particle, but not for other structures. For testing purposes, we consider various sizes of inclusions, spatial arrangements and topologies of a mixture. In this thesis, the numerical tests are limited to spherical inclusions. For computations the refractive indices of water and ice at a wavelength of 3.21 cm are chosen in order to compare the accuracy of various EMAs. With this choice, the different EMAs show substantial differences in the computed properties. By examining the accuracy of EMAs for the specified geometrical structure, we then can decide on criteria for choosing the most appropriate EMA based on the structural properties of the particle. It is expected that the conclusions given in this thesis regarding structures will also be applicable to other set of refractive indices, particularly for atmospheric applications when the difference in refractive index of the components of the mixture is smaller than that of water and ice.

Beside the need for testing the EMAs, it was stated by Chýlek et al (2000) that there is also a need to explore a different criterion for EMA especially to improve the accuracy for the absorption properties of a particle. Chýlek et al. (2000) proposed to employ

average of dielectric constant and refractive index weighted by $|\mathbf{E}|^2$, where $\mathbf{E}$ is the local electric field. We can think of the average of dielectric constant weighted by the $|\mathbf{E}|^2$ based on the conservation of energy content in the medium. This averaging method has not been explored in the past. The validity of this method is unknown. Because the FDTD method is based on direct discretization of Maxwell's equations, we can obtain easily the distribution of electric fields inside a heterogeneous particle. This creates an opportunity to explore various averaging schemes. Instead of energy content, another criterion for EMA based on the extinction or the attenuation of fields in the heterogeneous medium is also examined in this thesis.

In the FDTD method, an absorbing boundary condition (ABC) is used for truncating the FDTD computational space. The ABC is important since the accuracy of the FDTD method depends on the properties of the ABC. In the past decade a method known as the perfectly matched layer (PML) is frequently used. In the process of developing the FDTD method, a new ABC, which is called multiple absorbing surfaces (MAS), is also developed in this thesis.

In the past, a medium surrounding a particle is always considered to be non-absorbing. However, a medium, in general, is absorbing. The absorption of the host medium can, in some cases affect the scattering properties of a particle. It is therefore important to treat the absorbing host medium. In a formulation of EMA the assumption of a non-absorbing host medium is also used, even though the resulting effective medium is an absorbing medium. A new formalism for the scattering by a spherical particle (Mie scattering) in an absorbing host medium is developed in this thesis and a corrected formalism of EMA is also given.

Before continuing to discuss EMA, a review of the FDTD method is presented in chapter 2. In chapter 3, a new ABC for the FDTD method is presented. A new formalism of Mie scattering in absorbing medium is presented in chapter 4. A review of EMAs and a corrected EMA is presented in chapter 5. Numerical results of the FDTD calculations and discussions are presented in chapter 6. Finally, conclusions are given in chapter 7.

Chapter 2

The Finite-Difference Time-Domain Method

2.1 Maxwell's Equations

To solve a light scattering problem we begin with the fundamental equations that govern the electromagnetic wave propagation for macroscopic scale i.e. Maxwell's equations. The time-dependent Maxwell equations (Jackson, 1999) are

$$\nabla \cdot \mathbf{D} = \rho \tag{2.1}$$

$$\nabla \cdot \mathbf{B} = 0 \tag{2.2}$$

$$\nabla \times \mathbf{E} + \frac{\partial \mathbf{B}}{\partial t} = 0 \tag{2.3}$$

$$\nabla \times \mathbf{H} - \frac{\partial \mathbf{D}}{\partial t} = \mathbf{J}_e \tag{2.4}$$

where $\mathbf{E}$ and $\mathbf{H}$ are the electric and magnetic field vectors, $\mathbf{D}$ and $\mathbf{B}$ are the electric displacement and magnetic induction, ρ and $\mathbf{J}_e$ are the free electric charge and free electric current.

Beside the above equations (Eq. (2.1)-(2.4)) we also need to know relationships between the vectors $\mathbf{E}$ and $\mathbf{D}$, and between $\mathbf{H}$ and $\mathbf{B}$ which constitute the properties of a medium. For a linear, homogenous and isotropic medium the relationships are

$$\mathbf{D} = \varepsilon \mathbf{E} \tag{2.5}$$

$$\mathbf{B} = \mu \mathbf{H} \tag{2.6}$$

and for a conducting medium, the electric current is given by

$$\mathbf{J}_e = \sigma \mathbf{E} \tag{2.7}$$

where ε , μ and σ are permittivity, permeability and conductivity of a medium respectively.

In the FDTD method, a magnetic current source $\mathbf{J}_m$ is usually added in Eq (2.3) (Taflove, 1995). This addition is very useful since a magnetic loss contribution or a magnetic source can be accounted for. This is also needed for development of the PML-ABC and the MAS-ABC. A magnetic loss term is introduced in a similar way as adding conductivity of the medium that is

$$\mathbf{J}_m = \sigma_m \mathbf{H}. \tag{2.8}$$

With a magnetic current term Eq. (2.3) is now given by

$$\nabla \times \mathbf{E} + \frac{\partial \mathbf{B}}{\partial t} = -\mathbf{J}_m \tag{2.9}$$

A material which has a small value of conductivity is known as an insulator or a dielectric (Harrington, 1961). In a general problem a dielectric constant ε_r and a refractive index m are often used. The dielectric constant is defined as the ratio of permittivity of a medium to the permittivity of a free-space or a vacuum i.e. $\varepsilon_r = \varepsilon / \varepsilon_0$. In frequency domain the dielectric constant generally has a complex value ($\varepsilon_r = \varepsilon_R + i\varepsilon_I$). The dielectric constant is related to the refractive index by $\varepsilon_r = m^2$.

In general, a medium can be considered absorbing. The absorption of the medium in frequency domain is usually included in the imaginary part of the complex dielectric constant. Because the FDTD method uses real fields, the complex quantity cannot be used. It is possible, however, to include the absorption of the medium by introducing a conductivity of the medium. It can be shown that the value of conductivity needed to account for a non-zero imaginary part of the complex dielectric constant is given by $\sigma = \omega \varepsilon_I \varepsilon_0$; where $\omega = 2\pi f$, f is the frequency of a field (Jackson, 1999, page 312).

2.2 The Finite-Difference Time-Domain Method

The FDTD technique is based on the curl Maxwell differential equations (Eq. (2.3) and (2.4)). Taking the divergence of the curl equations can prove that the divergence equations (Eq. (2.1) and (2.2)) are already included in the curl equations (Taflove, 1995).

Substituting Eq. (2.7) and (2.8) into Eq. (2.4) and (2.9), and after rearrangement Eq. (2.4) and (2.9) become:

$$\frac{\partial \mathbf{H}}{\partial t} = -\frac{1}{\mu}[\nabla \times \mathbf{E} + \sigma_m \mathbf{H}] \tag{2.10}$$

$$\frac{\partial \mathbf{E}}{\partial t} = \frac{1}{\varepsilon}[\nabla \times \mathbf{H} - \sigma \mathbf{E}]. \tag{2.11}$$

We can note here that we have two coupled vector equations. To solve Eq. (2.10) and (2.11), we can think of these differential equations as an initial value problem where propagation of electromagnetic fields can be simulated by time marching of the above equations. We can set initial fields to zero, then a wave source is generated in the computational space by adding a current source. The propagation of the generated waves is simulated in time, which then interact with an inhomogeneous medium. This time marching scheme is the basis of the FDTD method.

In a Cartesian coordinate system the above vector differential equations are expanded to

$$\frac{\partial E_x}{\partial t} = \frac{1}{\varepsilon}\left[\frac{\partial H_z}{\partial y} - \frac{\partial H_y}{\partial z} - \sigma E_x\right] \tag{2.12}$$

$$\frac{\partial E_y}{\partial t} = \frac{1}{\varepsilon}\left[\frac{\partial H_x}{\partial z} - \frac{\partial H_z}{\partial x} - \sigma E_y\right] \tag{2.13}$$

$$\frac{\partial E_z}{\partial t} = \frac{1}{\varepsilon}\left[\left(\frac{\partial H_y}{\partial x} - \frac{\partial H_x}{\partial y}\right) - \sigma E_z\right] \tag{2.14}$$

$$\frac{\partial H_x}{\partial t} = \frac{1}{\mu}\left[\frac{\partial E_y}{\partial z} - \frac{\partial E_z}{\partial y} - \sigma_m H_x\right] \tag{2.15}$$

$$\frac{\partial H_y}{\partial t} = \frac{1}{\mu}\left[\frac{\partial E_z}{\partial x} - \frac{\partial E_x}{\partial z} - \sigma_m H_y\right] \tag{2.16}$$

$$\frac{\partial H_z}{\partial t} = \frac{1}{\mu}\left[\frac{\partial E_x}{\partial y} - \frac{\partial E_y}{\partial x} - \sigma_m H_z\right] \tag{2.17}$$

Equations (2.12)-(2.17) are approximated by a central finite difference scheme in both space and time. We follow a notation given by Yee (1966) where grid points in Cartesian coordinate is denoted by $(I,J,K) = (I\Delta x, J\Delta y, K\Delta z)$ and fields that are a function of space and time are denoted by $F^n(I,J,K) = F(I\Delta x, J\Delta y, K\Delta z, n\Delta t)$ where $\Delta x, \Delta y$ and Δz are spatial increments and Δt is a temporal increment. The FDTD algorithm employs a leapfrog time stepping scheme. In this scheme the electric fields are evaluated at time t and the magnetic fields are evaluated at time $t + \Delta t/2$.

To discretize the above equations in time, let us consider Eq. (2.12). Using a central difference approximation of derivative at time $t + \Delta t/2$, we have

$$\frac{1}{\Delta t}[E_x^{n+1}(I+\tfrac{1}{2},J,K) - E_x^n(I+\tfrac{1}{2},J,K)] = \frac{1}{\varepsilon}\left[\left(\frac{\partial H_z^{n+\frac{1}{2}}}{\partial y} - \frac{\partial H_y^{n+\frac{1}{2}}}{\partial z}\right) - \sigma E_x^{n+\frac{1}{2}}\right] \tag{2.18}$$

where ε and σ are evaluated at grid position of the electric field which in this case $(I+\frac{1}{2},J,K)$.

The electric fields at $(n+\frac{1}{2})$ is approximated by average of electric fields at n and $(n+1)$, that is

$$E_x^{n+\frac{1}{2}} = (E_x^{n+1} + E_x^n)/2 \tag{2.19}$$

After a manipulation we have

$$E_x^{n+1}(I+\tfrac{1}{2},J,K) = \frac{1-\Delta t\sigma/2\varepsilon}{1+\Delta t\sigma/2\varepsilon}E_x^n(I+\tfrac{1}{2},J,K) + \frac{\Delta t}{\varepsilon(1+\Delta t\sigma/2\varepsilon)}\left[\frac{\partial H_z^{n+\frac{1}{2}}}{\partial y} - \frac{\partial H_y^{n+\frac{1}{2}}}{\partial z}\right] \tag{2.20}$$

Similarly for Eq. (2.13)-(2.17), for example for the x component of magnetic field (Eq. (2.15)),

$$H_x^{n+\frac{1}{2}}(I,J+\tfrac{1}{2},J+\tfrac{1}{2}) = \frac{1-\Delta t\sigma_m/2\mu}{1+\Delta t\sigma_m/2\mu}H_x^{n-\frac{1}{2}}(I,J+\tfrac{1}{2},K+\tfrac{1}{2}) + \frac{\Delta t}{\mu(1+\Delta t\sigma_m/2\mu)}\left[\frac{\partial E_y^n}{\partial z} - \frac{\partial E_z^n}{\partial y}\right] \tag{2.21}$$

where μ and σ_m are evaluated at grid position of the magnetic field which in this case $(I, J+\frac{1}{2}, K+\frac{1}{2})$.

The spatial discretizations are done by considering a staggered arrangement of electric and magnetic fields in a cubic cell as suggested by Yee (1966) (see Fig. 2.1). The components of electric fields are placed in such a way that they are surrounded by four components of magnetic fields. Similarly for the components of magnetic fields are surrounded by four components of electric fields (Taflove, 1995; Sadiku, 1992). With this arrangement Faraday's law and Ampere's law are satisfied (Taflove, 1995; Sadiku, 1992).

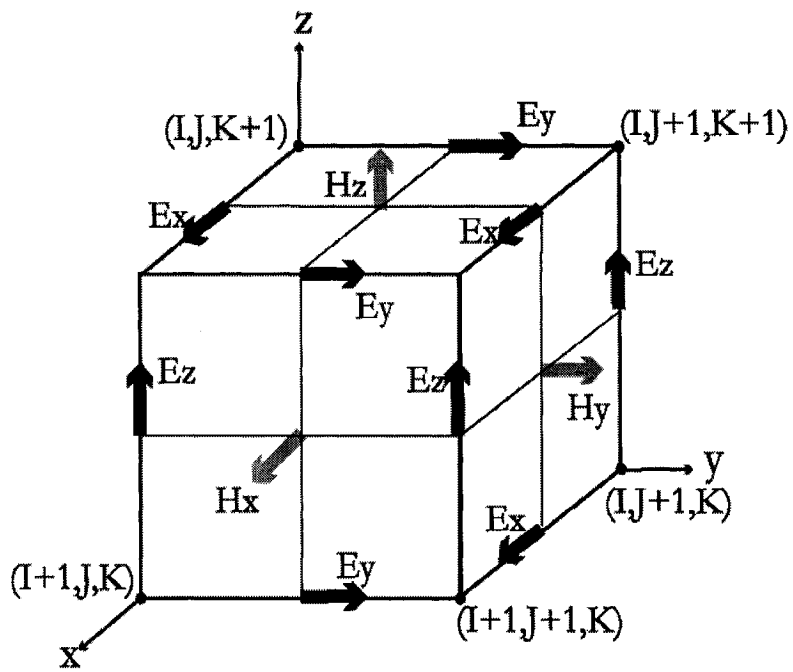

Figure 2.1: A staggered arrangement of electric and magnetic fields.

With this staggered spatial arrangement, Eq. (2.20) and (2.21) become

$$E_x^{n+1}(I+\tfrac{1}{2},J,K)=\frac{1-\Delta t\sigma/2\varepsilon}{1+\Delta t\sigma/2\varepsilon}E_x^{n}(I+\tfrac{1}{2},J,K)+$$
$$\frac{\Delta t}{\varepsilon(1+\Delta t\sigma/2\varepsilon)}\{\frac{1}{\Delta y}[H_z^{n+\frac{1}{2}}(I+\tfrac{1}{2},J+\tfrac{1}{2},K)-H_z^{n+\frac{1}{2}}(I+\tfrac{1}{2},J-\tfrac{1}{2},K)] \qquad (2.22)$$
$$-\frac{1}{\Delta z}[H_y^{n+\frac{1}{2}}(I+\tfrac{1}{2},J,K+\tfrac{1}{2})-H_y^{n+\frac{1}{2}}(I+\tfrac{1}{2},J,K-\tfrac{1}{2})]\}$$

$$H_x^{n+\frac{1}{2}}(I,J+\tfrac{1}{2},K+\tfrac{1}{2})=\frac{1-\Delta t\sigma_m/2\mu}{1+\Delta t\sigma_m/2\mu}H_x^{n-\frac{1}{2}}(I,J+\tfrac{1}{2},K+\tfrac{1}{2})+\frac{\Delta t}{\mu(1+\Delta t\sigma_m/2\mu)}\times$$

$$\{\frac{1}{\Delta z}[E_y^n(I,J+\tfrac{1}{2},K+1)-E_y^n(I,J+\tfrac{1}{2},K)]-\frac{1}{\Delta y}[E_z^n(I,J+1,K+\tfrac{1}{2})-E_z^n(I,J,K+\tfrac{1}{2})]\} \tag{2.23}$$

Discretizations of the other components of electric and magnetic fields can be obtained in a similar way. We note here that the electric and magnetic fields are interlaced in time and these are explicit equations. We can use these finite difference equations to update electric and magnetic fields alternately. We can inject incident fields and then propagation of fields can be determined by iteration in time.

To maintain stability of the FDTD iteration the spatial spacings and the temporal spacing must satisfy a stability condition given by (Taflove, 1995)

$$\Delta t \le \frac{1}{c\sqrt{\frac{1}{\Delta x^2}+\frac{1}{\Delta y^2}+\frac{1}{\Delta z^2}}} \tag{2.24}$$

For FDTD simulations, the FDTD cell is usually taken to be a cubic cell where $\Delta x = \Delta y = \Delta z = \Delta s$. Therefore the stability condition is given by

$$\Delta t \le \Delta s / c\sqrt{3}. \tag{2.25}$$

For simplicity, we use in our FDTD simulations the temporal step $\Delta t = \Delta s / 2c$.

In the FDTD method, a particle is modeled by assigning appropriate permittivities, conductivities and permeabilities at the appropriate spatial grids. Yang and Liou (1996, 2000) assumed the dielectric properties within each FDTD cell are homogeneous. In order to reduce staircasing errors Yang and Liou (1996 and 2000) used the Maxwell-Garnett mixing rule to evaluate the averaged permittivity properties of each FDTD cell. However, it was shown by Sun and Fu (2000) that the use of average value could introduce some errors. Therefore, in this study, the local value of permittivity at the grid point is used.

2.3 Absorbing Boundary Conditions

A scattering problem is an open space problem. In dealing with the open space problem we need a method to truncate an FDTD computational domain such that there are no

outgoing waves reflected back to the computational domain. This truncation method is known as an absorbing boundary condition (ABC) or a radiation boundary condition. This ABC is very important since the accuracy of the FDTD technique depends on the choice of ABC. There are many methods can be used to truncate the outer boundaries including one-way wave equations (OWWE), Higdon's operator, space-time extrapolations and absorbing materials method. The most popular method is the perfectly matched layer (PML)-ABC that is based on absorbing material method.

2.3.1 One-Way Wave Equations

The OWWE is derived from the scalar wave equation, that is

$$[\frac{1}{c^2}\frac{\partial^2}{\partial t^2} - \nabla^2]U = 0. \tag{2.26}$$

The wave equation can be split into two pseudo operators, such as:

$$L_z^+ L_z^- U = 0 \tag{2.27}$$

where L_z^+ and L_z^- are the OWWE operators for wave travelling in positive and negative z direction. The operators are given by (Engquist & Majda, 1977; Taflove, 1995, Yang & Liou, 2000).

$$L_z^{\pm} = D_z \pm \frac{D_t}{c}\sqrt{1 - \frac{c^2(D_x^2 + D_y^2)}{D_t^2}} \tag{2.28}$$

where D_x, D_y, D_z and D_t represent operators $\partial/\partial x$, $\partial/\partial y$, $\partial/\partial z$, and $\partial/\partial t$ respectively.

The operator L_z^- can absorb waves in the negative z direction without reflection if the following OWWE is satisfied

$$L_z^- U = 0 \tag{2.29}$$

It seems that this would be the perfect ABC. However, since operators L_z^+ and L_z^- are pseudo operators, they cannot be used in a numerical computation. We need to approximate the OWWE operators. The OWWE can be expanded using second order Taylor expansion to

$$L_z^- = D_z - \frac{D_t}{c}\sqrt{1 - \frac{c^2(D_x^2 + D_y^2}{D_t^2}} \approx D_z - \frac{D_t}{c} - \frac{1}{2}\frac{c(D_x^2 + D_y^2}{D_t} \tag{2.30}$$

The second order approximation of the OWWE can be expressed after a manipulation as (Taflove, 1995, Yang & Liou, 2000)

$$\left[\frac{1}{c}\frac{\partial^2}{\partial t \partial z} - \frac{1}{c^2}\frac{\partial^2}{\partial t^2} + \frac{1}{2}\left(\frac{\partial^2}{\partial x^2} + \frac{\partial^2}{\partial y^2}\right)\right]U = 0 \tag{2.31}$$

A first order approximation of the OWWE is

$$\left[\frac{1}{c}\frac{\partial}{\partial t} - \frac{\partial}{\partial z}\right]U = 0 \tag{2.32}$$

Many different expansions can be used to approximate the pseudo OWWE operators including Padé approximation, least square approximation and Chebyshev approximation (Taflove, 1995). Eqs. (2.31) and (2.32) can be discretized and then can be used for truncating the FDTD computational domain.

2.3.2 Higdon's Annihilation Operators

Another important one way operator is Higdon's annihilation operator. Higdon proposed a differential operator that absorbs waves exactly in certain incident angles α_j which is of the form

$$\prod_{j=1}^{N}\left(\cos\alpha_j \frac{\partial}{\partial t} - c_j \frac{\partial}{\partial z} + \beta_j\right)U = 0 \tag{2.33}$$

where N represents the order of the Higdon operator, c_j is the speed in the medium, and β_j is a constant. It can be shown that by choosing appropriate values of α_j , β_j and c_j, the second order Higdon operator is the same as the second order OWWE (Eq. (2.31)). Other properties of the Higdon operators are discussed further in chapter 3.

2.3.3 Perfectly Matched Layer ABC

The perfectly matched layer (PML) method was introduced by Berenger in 1994. The PML is based on the use of an absorbing layer to absorb outgoing waves. The main advantage in using the PML layer is that the impedance of the PML is matched with a medium. As consequence the PML provides a layer that produces very small reflection suitable for many applications.

To match the impedance of a medium and the PML, the six scalar Maxwell's equations are split into twelve differential equations. Each Cartesian coordinate is split into two components as follows (Berenger, 1994, 1996; Katz et al., 1994; Taflove, 1995).

$$E_x = E_{xy} + E_{xz}, E_y = E_{yx} + E_{yz}, E_z = E_{zx} + E_{zy}$$

$$H_x = H_{xy} + H_{xz}, H_y = H_{yx} + H_{yz}, H_z = H_{zx} + H_{zy} \tag{2.34}$$

The resulting equations with appropriate loss terms are

$$\frac{\partial H_{xy}}{\partial t} = \frac{1}{\mu}\left[-\frac{\partial E_z}{\partial y} - \sigma_{m,y} H_{xy}\right], \frac{\partial H_{xz}}{\partial t} = \frac{1}{\mu}\left[\frac{\partial E_y}{\partial z} - \sigma_{m,z} H_{xz}\right]$$

$$\frac{\partial H_{yx}}{\partial t} = \frac{1}{\mu}\left[\frac{\partial E_z}{\partial x} - \sigma_{m,x} H_x\right], \frac{\partial H_{yz}}{\partial t} = \frac{1}{\mu}\left[-\frac{\partial E_x}{\partial z} - \sigma_{m,z} H_{yz}\right]$$

$$\frac{\partial H_{zx}}{\partial t} = \frac{1}{\mu}\left[-\frac{\partial E_y}{\partial x} - \sigma_{m,x} H_{zx}\right], \frac{\partial H_{zy}}{\partial t} = \frac{1}{\mu}\left[\frac{\partial E_x}{\partial y} - \sigma_{m,y} H_{zy}\right]$$

$$\frac{\partial E_{xy}}{\partial t} = \frac{1}{\varepsilon}\left[\frac{\partial H_z}{\partial y} - \sigma_y E_{xy}\right], \frac{\partial E_{xz}}{\partial t} = \frac{1}{\varepsilon}\left[-\frac{\partial H_y}{\partial z} - \sigma_z E_{xz}\right]$$

$$\frac{\partial E_{yx}}{\partial t} = \frac{1}{\varepsilon}\left[-\frac{\partial H_z}{\partial x} - \sigma_x E_{yx}\right], \frac{\partial E_{yz}}{\partial t} = \frac{1}{\varepsilon}\left[\frac{\partial H_x}{\partial z} - \sigma_z E_{yz}\right]$$

$$\frac{\partial E_{zx}}{\partial t} = \frac{1}{\varepsilon}\left[\frac{\partial H_y}{\partial x} - \sigma_x E_{zx}\right], \frac{\partial E_{zy}}{\partial t} = \frac{1}{\varepsilon}\left[-\frac{\partial H_x}{\partial y} - \sigma_y E_{zy}\right] \tag{2.35}$$

These equations can be discretized in similar way as before. Because we have introduced loss terms in the split equations, the waves that propagate in the PML region are attenuated. The rate of attenuation depends on the value of conductivities. In order that there is no reflection caused by the interface between the PML region and the FDTD region the conductivity must satisfy the following matching condition

$$\frac{\sigma}{\varepsilon_0} = \frac{\sigma_m}{\mu_0} \tag{2.36}$$

For a wave traveling in the z direction we need only to satisfy the matching condition for $\sigma_{m,z}$ and σ_z, other conductivities are set to zero. For waves in other directions such

as the x or y direction, the matching condition is required only for the conductivity in the direction of propagation. In the corner region, there is an overlap between the PML layers. It was shown that the overlap region does not cause any reflections (Berenger, 1994).

For a continuous space, the interface between the PML layer and the FDTD region does not cause a reflection (Berenger, 1994). However, in a discrete space the PML causes considerable reflections. To reduce reflection the conductivity values are generally chosen as small as possible at the PML and FDTD interface and the conductivity values are then increased to a maximum value at the outer most layers. A polynomial conductivity profile is generally used which is in the form of

$$\sigma(r) = \sigma_{\max}(r/d)^p \tag{2.37}$$

where r and d are the distance from the interface of PML and FDTD medium, and the length of the PML layer respectively. The maximum conductivity can be specified by the normal reflectance $R(0^o)$ of the interface boundary as (Berenger, 1994; Taflove, 1995; Gedney, 1998)

$$\sigma_{\max} = -(p+1)\varepsilon c \ln(R(0^o))/2d\,. \tag{2.38}$$

Many comparison studies between the PML-ABC and the analytical ABCs, such as one way differential equations, showed that the reflection produced by PML is much smaller than the analytical ABCs (Berenger, 1994; Katz et al., 1994). Because of this superiority, the PML method is now considered as the standard method for truncating the FDTD computational space (Shlager & Schneider, 1998).

Another type of ABC is called the multiple absorbing surfaces (MAS). This is a new type of ABC developed in this thesis. The MAS method has a comparable reflection to the PML method. This new ABC is discussed in the next chapter.

2.4 Incident Field

The incident fields are injected into an FDTD computational domain by using a virtual surface or a Huygens surface surrounding the particle or a total-field/scattered-field method. The virtual surface divides an FDTD spatial domain into two regions: inner region and outer region. In the inner region only total fields are calculated and in the

outer region only scattered fields are calculated. The total fields are the sum of the incident fields and the scattered fields. In order to satisfy consistency between two regions a connecting condition is imposed at the virtual surface. A discussion on this topic is discussed in chapter 3, and further discussion can be found in Taflove (1995, chapter 6).

2.5 Time Domain to Frequency Domain Transformation

In order to determine optical scattering properties we need to transform the time domain values obtained by the FDTD method to the corresponding frequency domain values. In this report we use an incident Gaussian pulse for initial excitation and the discrete Fourier transform to obtain the frequency response.

Let us consider a field in time domain at time step n denoted by f_n and the field is (Yang & Liou, 2000)

$$f(t) = \sum_{n=0}^{N} f_n \delta(t - n\Delta t) \tag{2.39}$$

where $\delta(t)$ is the Dirac delta function. The discrete Fourier transform of Eq. (2.39) is given by (Yang & Liou, 2000)

$$F(\omega) = \int_{-\infty}^{\infty} \sum_{n=0}^{N} f_n \delta(t - n\Delta t) \exp(i\omega t) dt = \sum_{n=0}^{N} f_n \exp(i\omega n\Delta t) . \tag{2.40}$$

The maximum time step N is chosen large enough such that the fields in computational domain after time step N are very small values.

2.5 Optical Scattering Properties

The optical scattering properties of a particle can be calculated by a surface- or a volume-integration method. The absorption cross section σ_{abs} is obtained by

$$\sigma_{abs} = -\frac{1}{2I_0} \mathrm{Re}\{\oiint_S [\mathbf{E}(\mathbf{r}') \times \mathbf{H}^*(\mathbf{r}')] \cdot \hat{\mathbf{n}}\, d^2 r'\} \tag{2.41}$$

where the above integration is around surface enclosing a particle, $\hat{\mathbf{n}}$ is the unit vector outward normal to the enclosing surface, $\mathbf{E}$ and $\mathbf{H}$ are the total fields outside the particle, the asterisk represents complex conjugate, and $I_0 = \varepsilon_0 c|E_0|^2/2$ where E_0 is the magnitude of incident field. Similarly the scattering cross section is obtained by

$$\sigma_{sca} = \frac{1}{2I_0}\mathrm{Re}\{\oiint_S [\mathbf{E}_{sca}(\mathbf{r}') \times \mathbf{H}^*_{sca}(\mathbf{r}')] \cdot \hat{\mathbf{n}}\, d^2 r'\} \tag{2.42}$$

where $\mathbf{E}_{sca}$ and $\mathbf{H}_{sca}$ are the scattered fields outside the particle

Instead of the above surface integration the optical properties can also be computed using a volume-integration. It can be shown (see chapter 4) that σ_{abs} is given by

$$\sigma_{abs} = \frac{k_0}{|E_0|^2}\iiint_V \varepsilon_I(\mathbf{r}')|\mathbf{E}(\mathbf{r}')|^2 d^3 r', \tag{2.43}$$

where ε_I is the imaginary part of dielectric constant, k_0 is the wave number in the host medium and the integration is over the volume of a particle. It can be shown also that the extinction cross section σ_{ext} is given by

$$\sigma_{ext} = \frac{1}{2I_0}\varepsilon_0 \omega[\mathrm{Im}\{\iiint_V (\varepsilon_r - \varepsilon_h^*)\mathbf{E}(\mathbf{r}') \cdot \mathbf{E}_i^*(\mathbf{r}') d^3 r'\} - \iiint_V \varepsilon_{hI}|\mathbf{E}_i(\mathbf{r}')|^2 d^3 r'] \tag{2.44}$$

where $\mathbf{E}_i(\mathbf{r})$ is the incident fields, the asterisk means complex conjugate, $\varepsilon_h = \varepsilon_{hR} + \varepsilon_{hI} i$ is the complex dielectric constant of the host medium.

The scattered far field can obtained by a surface integration (Jackson, 1999; Maloney & Smith, 1998):

$$\mathbf{E}_s(\mathbf{r}) = \frac{\exp(ik_0 r)}{-ik_0 r}\frac{k_0^2}{4\pi}\oiint_S \{\hat{\mathbf{r}} \times [\hat{\mathbf{n}} \times \mathbf{E}(\mathbf{r}')] - \eta_0 \hat{\mathbf{r}} \times \hat{\mathbf{r}} \times [\hat{\mathbf{n}} \times \mathbf{H}(\mathbf{r}')]\} \exp(-ik_0 \hat{\mathbf{r}} \cdot \mathbf{r}') d^2 \mathbf{r}' \tag{2.45}$$

where $\eta_0 = \sqrt{\mu_0/\varepsilon_0}$, and the corresponding volume integration for non-absorbing host medium is (Yang and Liou, 2000)

$$\mathbf{E}_s(\mathbf{r}) = \frac{\exp(ik_0 r)}{-ik_0 r}\frac{k_0^3}{4\pi}\iiint_V [\varepsilon(\mathbf{r}') - 1]\{\mathbf{E}(\mathbf{r}') - \hat{\mathbf{r}}[\hat{\mathbf{n}} \cdot \mathbf{E}(\mathbf{r}')]\} \exp(-ik_0 \hat{\mathbf{r}} \cdot \mathbf{r}') d^3 \mathbf{r}' \tag{2.46}$$

2.6 Amplitude Scattering Matrix

To obtain the amplitude scattering matrix, we follow here the convention given in Bohren and Huffman (1983) where the direction of the incident field is in the z direction. The far field vector $\mathbf{E}_s$ can be decomposed into two components (parallel and perpendicular to the scattering plane) in the form

$$\mathbf{E}_s = E_{s,\parallel}\hat{\mathbf{e}}_\parallel + E_{s,\perp}\hat{\mathbf{e}}_\perp \tag{2.47}$$

where in the spherical coordinate basis vectors, the parallel basis vector is $\hat{\mathbf{e}}_\parallel = \hat{\mathbf{e}}_\theta$ and the perpendicular is $\hat{\mathbf{e}}_\perp = -\hat{\mathbf{e}}_\phi$. The incident field can also be decomposed into the two components,

$$\mathbf{E}_i = E_{i,\parallel}\hat{\mathbf{e}}_\parallel + E_{i,\perp}\hat{\mathbf{e}}_\perp . \tag{2.48}$$

The amplitude of scattered fields Eq. (2.47) can be expressed as a linear function of the amplitude of incident fields Eq. (2.48) in the form of

$$\begin{bmatrix} E_{s,\parallel} \\ E_{s,\perp} \end{bmatrix} = \frac{\exp(ik(r-z))}{-ikr} \begin{bmatrix} S_2 & S_3 \\ S_4 & S_1 \end{bmatrix} \begin{bmatrix} E_{0,\parallel} \\ E_{0,\perp} \end{bmatrix} \tag{2.49}$$

where S_j is the component of amplitude scattering matrix. The amplitude of scattered fields can be re-expressed as

$$\begin{bmatrix} E_{s,\parallel} \\ E_{s,\perp} \end{bmatrix} = \frac{\exp(ik(r-z))}{-ikr} \begin{bmatrix} F_\parallel \\ F_\perp \end{bmatrix}. \tag{2.50a}$$

where

$$\begin{bmatrix} F_\parallel \\ F_\perp \end{bmatrix} = \begin{bmatrix} S_2 & S_3 \\ S_4 & S_1 \end{bmatrix} \begin{bmatrix} E_{0,\parallel} \\ E_{0,\perp} \end{bmatrix} \tag{2.50b}$$

For an FDTD computation, the incident fields can be expressed in a Cartesian coordinate system by

$$E_i = E_{i,x}\hat{\mathbf{x}} + E_{i,y}\hat{\mathbf{y}} \tag{2.51}$$

The relationship between components of the incident field in the Cartesian basis vector, and the basis vectors $\hat{\mathbf{e}}_\parallel$ and $\hat{\mathbf{e}}_\perp$ is

$$\begin{bmatrix} E_{i,\parallel} \\ E_{i,\perp} \end{bmatrix} = \begin{bmatrix} \cos\phi & \sin\phi \\ \sin\phi & -\cos\phi \end{bmatrix} \begin{bmatrix} E_{i,x} \\ E_{i,y} \end{bmatrix}. \tag{2.52}$$

Therefore

$$\begin{bmatrix} F_{\parallel} \\ F_{\perp} \end{bmatrix} = \begin{bmatrix} S_2 & S_3 \\ S_4 & S_1 \end{bmatrix} \begin{bmatrix} \cos\phi & \sin\phi \\ \sin\phi & -\cos\phi \end{bmatrix} \begin{bmatrix} E_{i,x} \\ E_{i,y} \end{bmatrix} \tag{2.53}$$

By selecting the scattered fields for two polarizations of incident fields (x-polarized ($E_{i,x} = 1, E_{i,y} = 0$) and y-polarized ($E_{i,x} = 0, E_{i,y} = 1$), we can determine the amplitude scattering matrix by

$$\begin{bmatrix} S_2 & S_3 \\ S_4 & S_1 \end{bmatrix} = \begin{bmatrix} F_{\parallel,x} & F_{\parallel,y} \\ F_{\perp,x} & F_{\perp,y} \end{bmatrix} \begin{bmatrix} \cos\phi & \sin\phi \\ \sin\phi & -\cos\phi \end{bmatrix} \tag{2.54}$$

where subscripts x and y represents the quantity F obtained for x- and y-polarized incident fields.

The Stokes phase matrix can be computed using the expressions given in Bohren and Huffman (1983, page 65). An example of expression for phase matrix S_{11} is given by

$$S_{11} = \tfrac{1}{2}(|S_1|^2 + |S_2|^2 + |S_3|^2 + |S_4|^2) \tag{2.55}$$

A C language computer program was written to calculate the cross-sections, asymmetry factor and phase function using the FDTD method with the PML- and the MAS-ABC is given in Sudiarta (2003a).

2.7 Validations of the FDTD method

To validate the FDTD computer program developed here, we consider a spherical water droplet with a radius a and refractive index $1.33 + 0.01i$ and we used the FDTD parameter $\lambda / \Delta s = 30$, where λ is the wavelength in vacuum. We computed the single scattering properties for two size parameters, $x = 2\pi a / \lambda = 1$ and $x = 5$. The results for efficiencies and asymmetry factors are given in Table 2.1 and 2.2. The FDTD results show good agreement with the Mie results. For a small size particle ($x = 1$), the relative differences between the FDTD and the Mie results are less than 1% for scattering and extinction efficiencies, and about 6% for absorption efficiency. By increasing the FDTD parameter $\lambda / \Delta s$, this relative error can be reduced. For a larger particle ($x = 5$) all the relative errors are less than about 1%. The FDTD results for phase function, as shown in Fig. 2.2 and 2.3, generally have relative errors less than about 5%.

Table 2.1: A comparison between the FDTD method ($\lambda / \Delta s = 30$, λ is the wavelength in vacuum) and the Mie solution for spherical particle with radius a, size parameter $x = 2\pi a / \lambda = 1$ and refractive index $m = 1.33 + 0.01i$.

$x = 1$	Q_{ext}	Q_{sca}	Q_{abs}	g
Mie results	0.1218	0.0933	0.0285	0.1852
FDTD	0.1208	0.0939	0.0269	0.1817
Relative Error (%)	-0.8	0.6	-5.7	-1.9

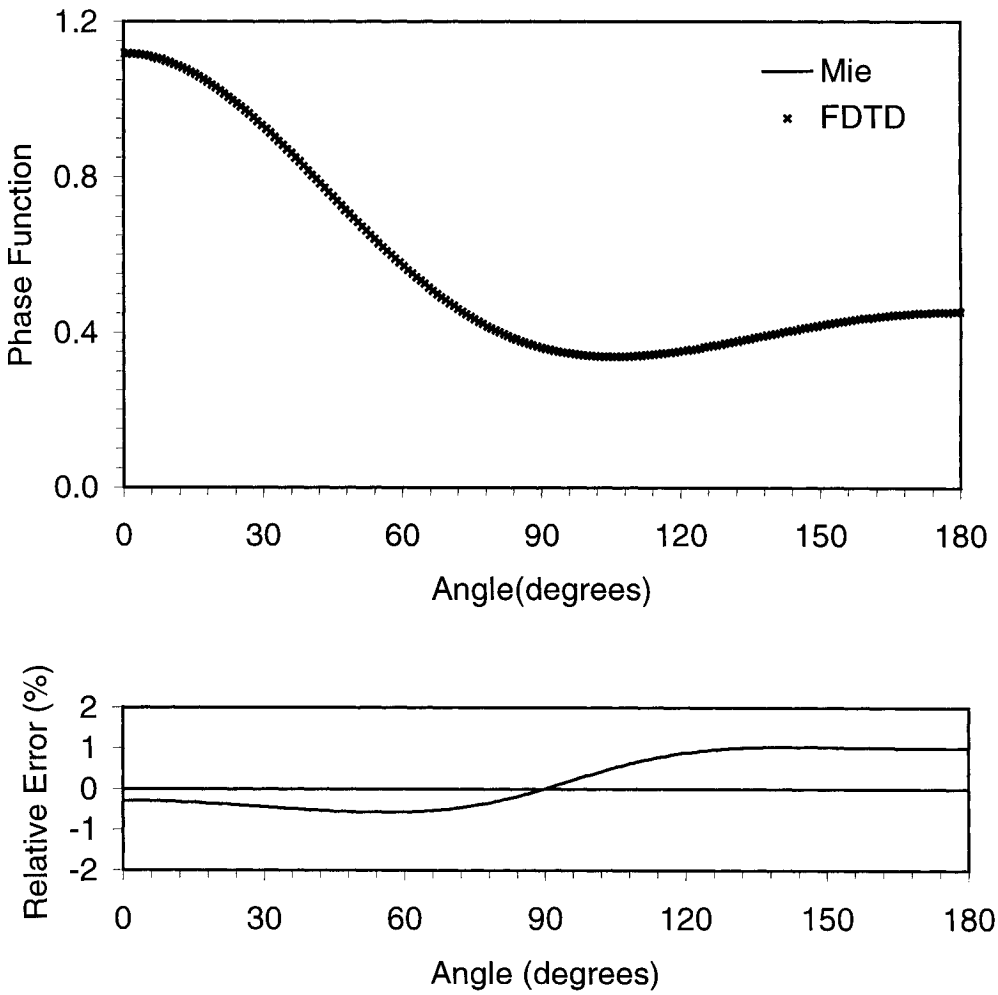

Figure 2.2: A comparison of the FDTD and the Mie phase functions for radius a, size parameter $x = 2\pi a / \lambda = 1$ and refractive index $m = 1.33 + 0.01i$. The FDTD parameter is $\lambda / \Delta s = 30$, where λ is the wavelength in vacuum.

Table 2.2: A comparison between the FDTD method ($\lambda / \Delta s = 30$) and the Mie solution for spherical particle with size parameter $x = 5$ and refractive index $m = 1.33 + 0.01i$.

$x = 5$	Q_{ext}	Q_{sca}	Q_{abs}	g
Mie results	3.4842	3.2889	0.19524	0.8529
FDTD results	3.4834	3.2868	0.19661	0.8544
Relative Error (%)	-0.02	-0.06	0.70	0.17

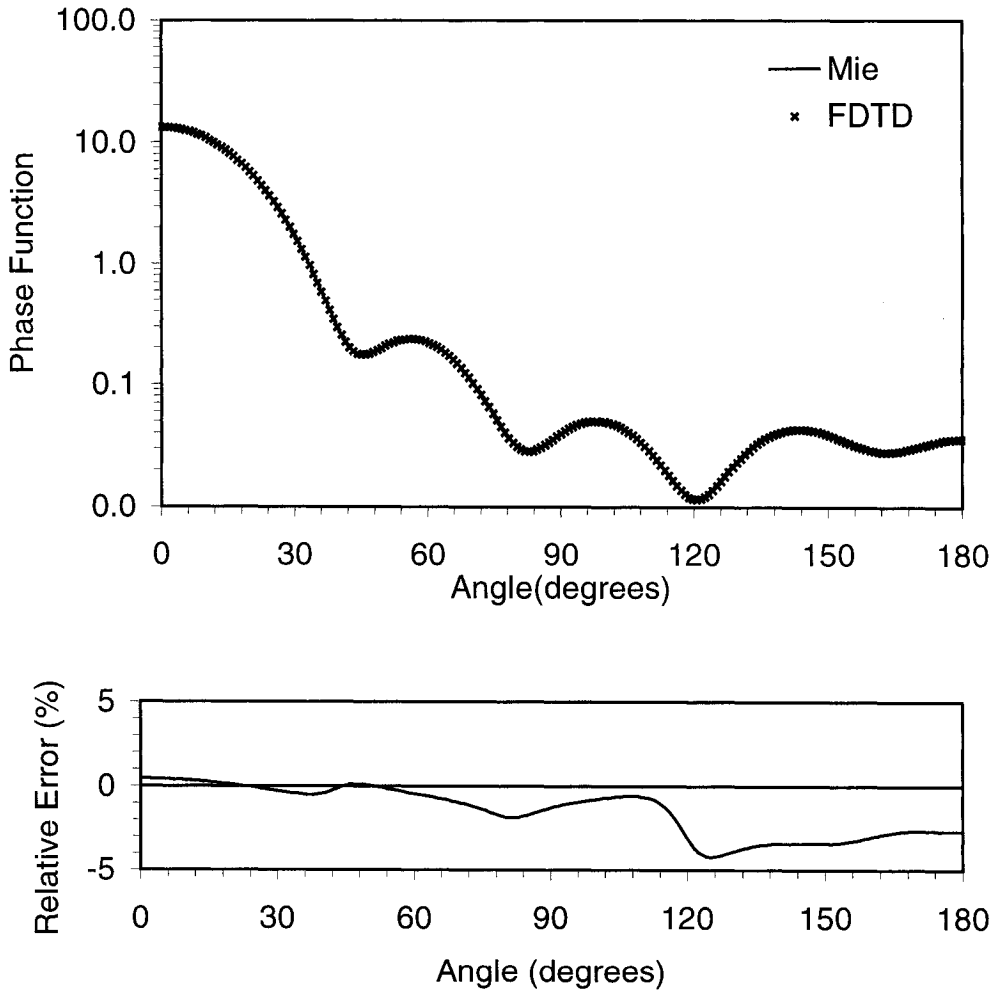

Figure 2.3: A comparison of the FDTD and the Mie phase function for size parameter $x = 5$ and refractive index $m = 1.33 + 0.01i$. The FDTD parameter is $\lambda / \Delta s = 30$.

2.8 The FDTD Method for a Very Small Sphere

It has been shown that the FDTD method gives accurate results provided that appropriate FDTD parameter is used. The FDTD accuracy is highly dependent on the grid spacing used. In this study we have employed a rectangular grid for our FDTD method. The reason for this choice is that the rectangular grid offers simplicity in computational code and flexibility for approximating an arbitrary shaped object. However, the rectangular grid can also introduce a truncation error especially for approximating a curved boundary.

For atmospheric applications, scattering particles, such as aerosols, are composed of many different components. The components may have dimensions much smaller than the wavelength. In this study we use the FDTD method for solving a scattering by this kind of particle. Therefore we need to investigate the validity of the FDTD method for a small particle. Another reason for considering the small particle is the application of the FDTD method for testing various effective medium approximations (EMAs). The commonly used EMAs, such as the Maxwell-Garnett and the Bruggeman mixing rules, assume the size parameter of composite grains are much smaller than 1 (Chýlek et al., 2000).

As mentioned previously a scatterer is approximated by assigning appropriate dielectric properties at FDTD grid points. In this study we use local dielectric properties of the scatterer at the grid points. If a FDTD grid point is located inside the scatterer, the dielectric properties of the scatterer are used. If it is outside the scatterer, then the dielectric properties of a host medium are used. This is an "in or out" approach.

To study the FDTD accuracy, the parameter $\lambda/\Delta s = 400$ is used. We performed FDTD simulations for scattering by a spherical particle with a size parameter less than 1 and the refractive index of water $m_w = 7.14 + 2.89i$ at 3.21 cm wavelength. This refractive index is used in chapter 6 to test various EMAs. The FDTD results for efficiencies and asymmetry factor are given in Table 2.3.

Table 2.3: Efficiencies and asymmetry factor of a spherical particle ($m = 7.14 + 2.89i$, radius = a) computed using the Mie theory and the FDTD method. The FDTD parameter is $\lambda / \Delta s = 400$ where λ is wavelength in vacuum. The size parameter of the sphere is $x = 2\pi a / \lambda$.

			Mie					
x	Qext	Qsca	Qabs	g				
0.01	1.35E-03	2.48E-08	1.35E-03	1.54E-04				
0.02	2.73E-03	3.97E-07	2.73E-03	6.15E-04				
0.05	7.44E-03	1.55E-05	7.43E-03	3.84E-03				
0.1	1.98E-02	2.51E-04	1.96E-02	1.53E-02				
0.2	9.32E-02	4.19E-03	8.90E-02	5.65E-02				
0.4	7.57E-01	8.65E-02	6.71E-01	-6.40E-02				
0.5	9.75E-01	2.25E-01	7.50E-01	-1.66E-01				
			FDTD		Relative Error (%)			
x	Qext	Qsca	Qabs	g	δQ_{ext}	δQ_{sca}	δQ_{abs}	δg
0.01	6.00E-03	3.76E-07	6.00E-03	-3.00E-06	346	1417	346	-102
0.02	3.25E-03	8.52E-07	3.25E-03	7.51E-04	19	115	19	22
0.05	7.84E-03	1.49E-05	7.82E-03	2.98E-03	5	-4	5	-22
0.1	2.28E-02	2.98E-04	2.25E-02	1.38E-02	15	19	15	-9
0.2	9.45E-02	4.39E-03	9.01E-02	5.41E-02	1	5	1	-4
0.4	7.58E-01	8.80E-02	6.70E-01	-6.11E-02	0.1	2	-0.1	-4
0.5	9.83E-01	2.30E-01	7.53E-01	-1.63E-01	1	2	0.4	-2

We can note in Table 2.3 that the FDTD method with $\lambda / \Delta s = 400$ is appropriate only for size parameter 0.05 and larger than 0.2. Smaller grid spacing might be used to increase the FDTD accuracy. This can only be done for a single particle. When a particle with small inclusions is considered, the FDTD method with very small spacing requires large computational resources. However, as the spacing becomes finer the FDTD error increases due to a round-off error. Therefore the "in or out" approach for dielectric assignment is not appropriate for approximating a small particle. An alternative method for modeling a small particle in the FDTD method is needed.

When we have a very small particle ($x << 1$), in this case a sphere, we do not need a high-resolution computation to resolve the particle since the fields are almost constants inside the particle. This means that the inside fields can be approximated by a single average field. Therefore, the particle can be approximated by assigning dielectric properties at one FDTD cubic cell. Because of the staggered structure of an FDTD mesh, we can only position the cube center at a position of a component of electric fields. Other positions may cause a non-trivial assignment of dielectric properties.

Let us consider a cubic cell of dielectric material centered at the position of electric field $E_x(I+\frac{1}{2},J,K)$. A cross section of the cube in rectangular mesh is shown in Fig. 2.4. Because the cubic material is affected only by the field $E_x(I+\frac{1}{2},J,K)$, this cube represents a dipole with polarization in the x direction.

When an FDTD grid spacing is much smaller than the wavelength in the medium, the cube can be approximated by an equal-volume sphere. The size of the cube is Δs. The radius of equal-volume sphere is $r_V = \Delta s\sqrt[3]{3/4\pi}$. The polarizability of the cube is approximated in the static limit by

$$\alpha_c = 3(\Delta s)^3 \frac{\varepsilon_c - \varepsilon_m}{\varepsilon_c + 2\varepsilon_m} \tag{2.56}$$

where ε_c and ε_m are the dielectric constant of the cube and the host medium respectively. In the static limit, the absorption cross section of the cube is given by

$$\sigma_{abs} = k\,\mathrm{Im}\{\alpha_c\} = 3(\Delta s)^3 k\,\mathrm{Im}\left\{\frac{\varepsilon_c - \varepsilon_m}{\varepsilon_c + 2\varepsilon_m}\right\}. \tag{2.57}$$

and scattering cross section is

$$\sigma_{sca} = \frac{k^4}{6\pi}|\alpha_c|^2 = 9(\Delta s)^6 \frac{k^4}{6\pi}\left|\frac{\varepsilon_c - \varepsilon_m}{\varepsilon_c + 2\varepsilon_m}\right|^2. \tag{2.58}$$

The phase function is given by

$$p(\theta) = \frac{3}{4}[1+\cos^2(\theta)] \tag{2.59}$$

The absorption and scattering cross sections can also be calculated exactly using the Mie theory.

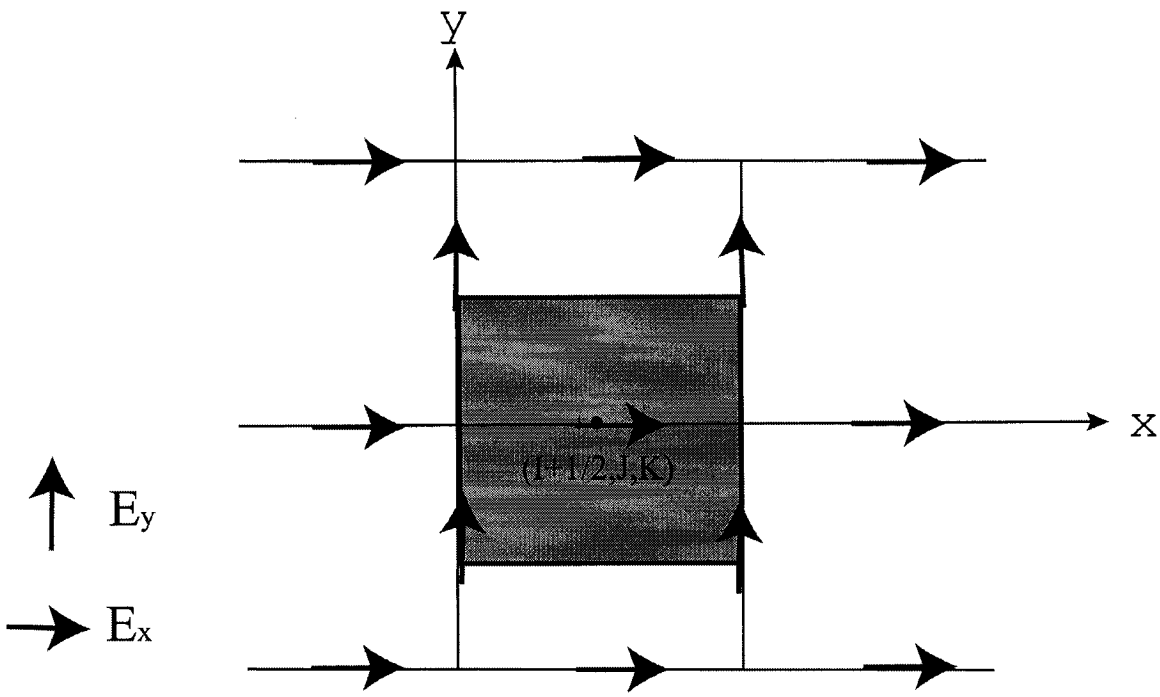

Figure 2.4: A cross section of a cube located at grid $(I+\frac{1}{2},J,K)$ in a FDTD mesh.

To investigate whether the approximation of a cube by a sphere is appropriate, we performed FDTD simulations for different grid spacing. We use the same refractive index as previous simulations ($m = 7.14+2.89i$). We consider a plane wave incident in the z-axis direction, and polarized in x and y. The results for cross-sections of a dielectric cube (size $\Delta s = \lambda/150$) are shown in Table 2.4. Table 2.4 shows clearly the anisotropic nature of the cube where the cross sections depend on the polarization of the incident field. The cross sections are larger for x-polarized incident field than the y-polarized incident field. This confirms that the cube represents an electric dipole.

Comparisons of FDTD results with Mie theory (equal-volume sphere) for x-polarized incident field are shown in Fig. 2.5-2.7. The FDTD results are in agreement with the Mie results for grid spacing less than 0.007λ. The relative errors are generally less than or about 2% for grid spacing $\Delta s < 0.007\lambda$. We also note that the FDTD results and the static limit results show similar values. This indicates that the FDTD method treats the field in the cubic cell as a static field.

Table 2.4: Cross sections of a cube centered at position of electric field $E_x(I+\frac{1}{2},J,K)$ using the FDTD method ($\lambda/\Delta s=150$). The incident field propagates in a positive z-axis direction.

Polarization of incident field	σ_{ext} (in unit λ^2)	σ_{sca} (in unit λ^2)	σ_{abs} (in unit λ^2)
x-polarized	1.87486×10^{-7}	6.08529×10^{-11}	1.87466×10^{-7}
y-polarized	6.04606×10^{-21}	2.82012×10^{-18}	6.35856×10^{-22}

Numerical results for phase functions are shown in Fig. 2.8. It is shown that the phase function of the cube can be represented well by the phase function of a small sphere.

We also perform another FDTD simulations for different refractive indices in order to study the effect of refractive index of the cube. The results, as shown in Table 2.5, indicate that the approximation of a cube particle with an equal-volume sphere is justified. Conversely, we can also say that a small spherical particle can be approximated in the FDTD method by a cubic cell provided that an appropriate grid spacing is used.

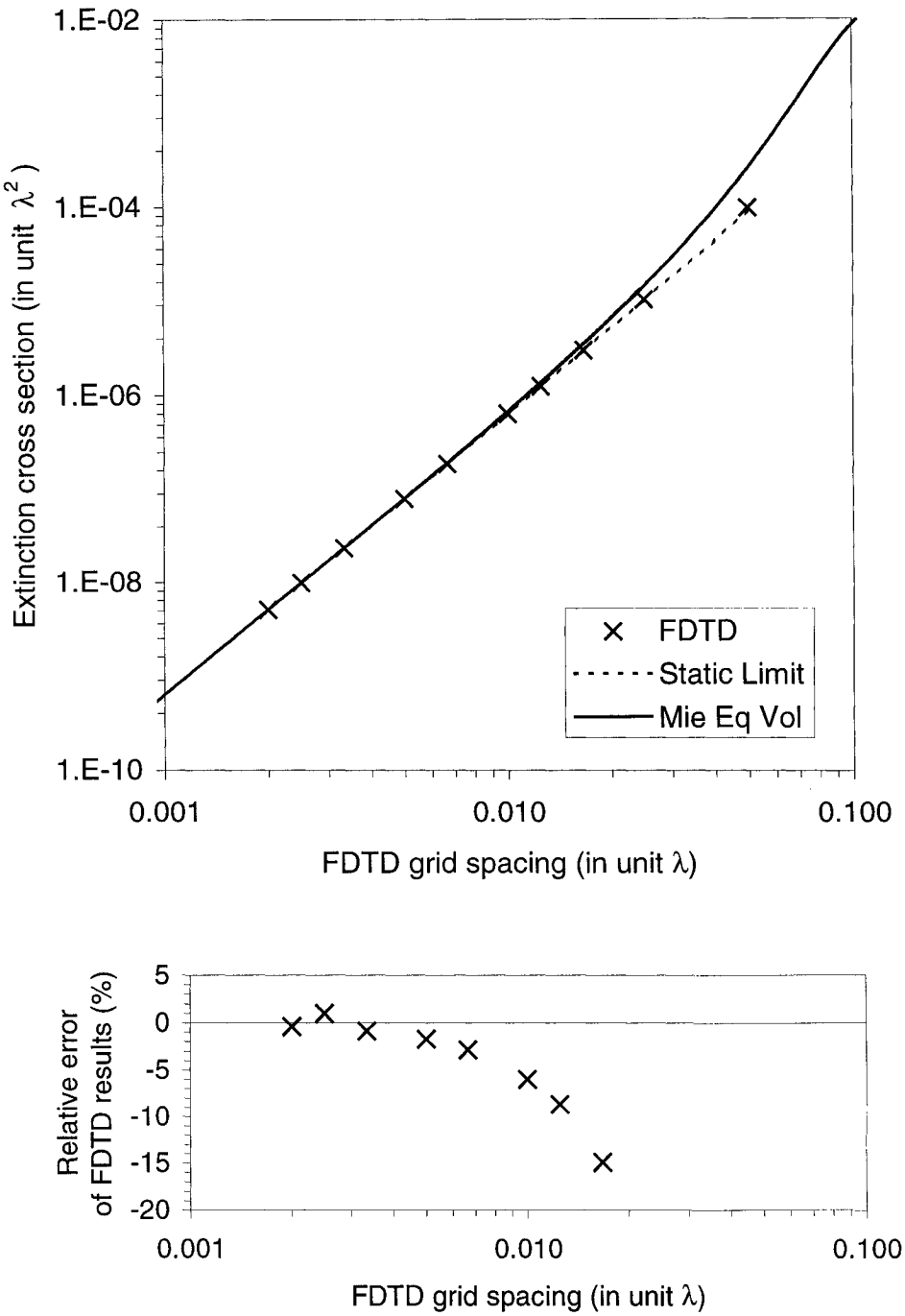

Figure 2.5: Extinction cross section and relative error of a cube. The Mie results are computed using an equal-volume sphere radius. The static limit results are calculated by using Eq. 2.57 and Eq. 2.58.

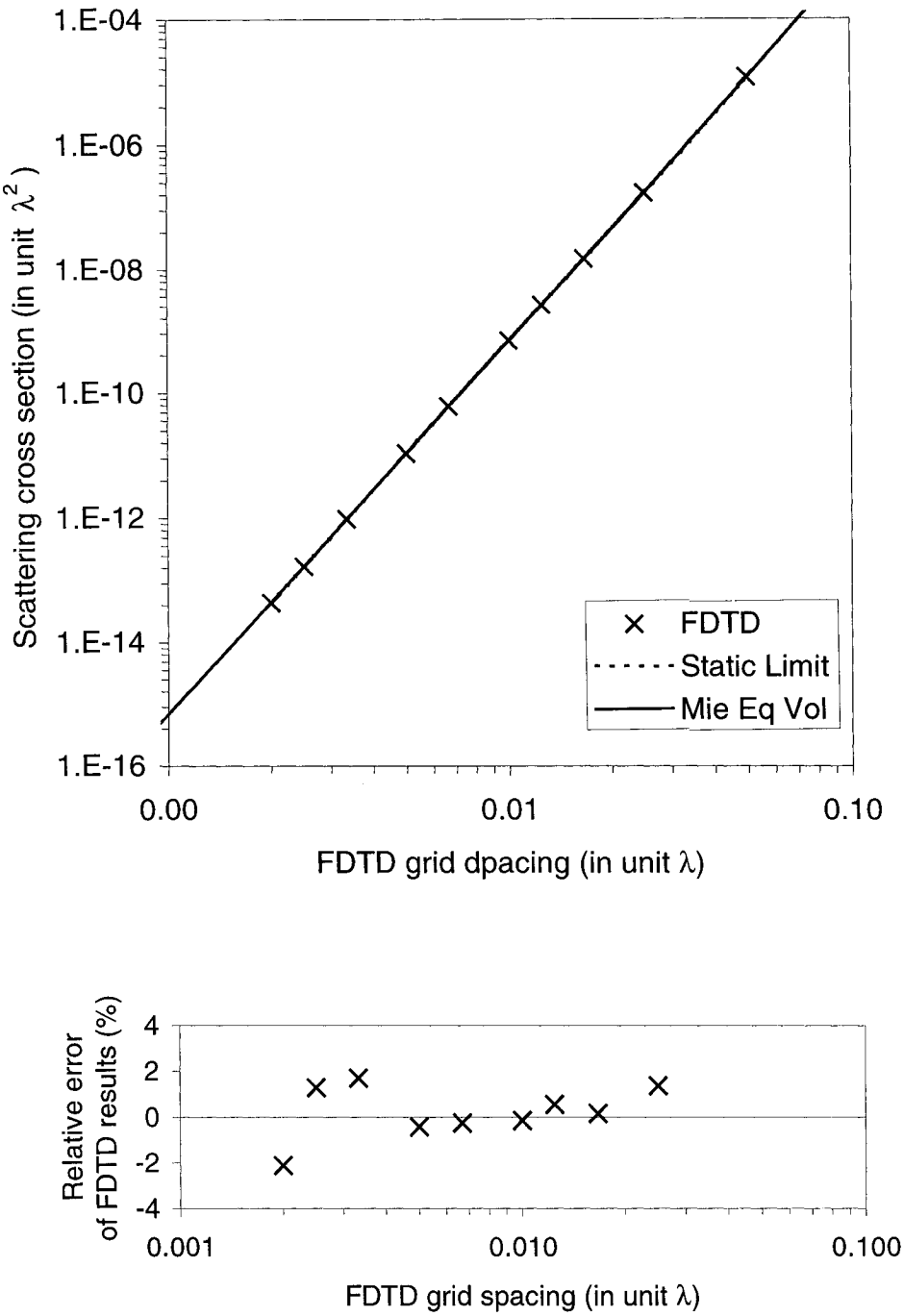

Figure 2.6: Scattering cross section and relative error of a cube. The Mie results are computed using an equal-volume sphere radius. The static limit results are calculated by using Eq. 2.58.

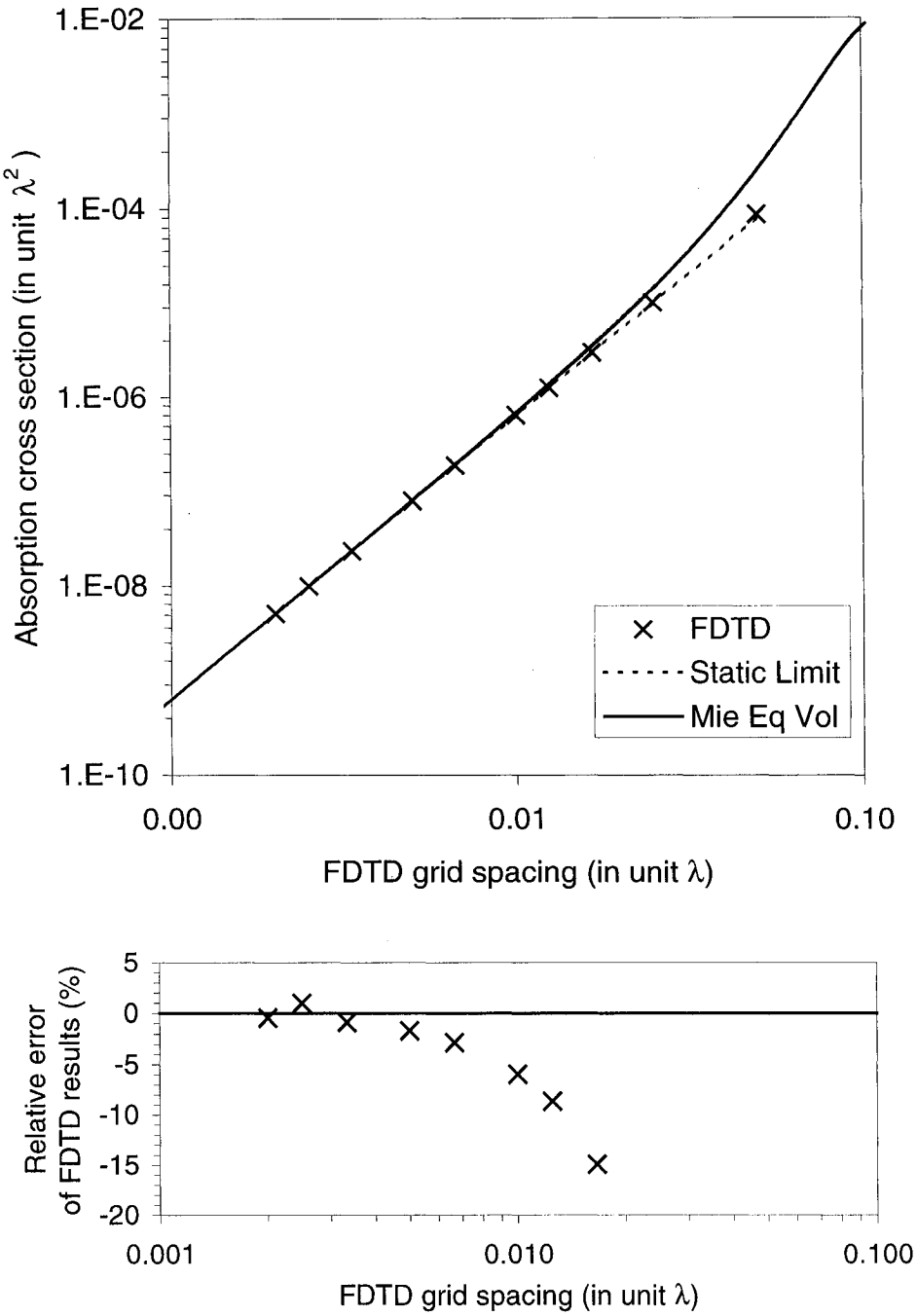

Figure 2.7: Absorption cross section and relative error of a cube. The Mie results are computed using an equal-volume sphere radius. The static limit results are calculated by using Eq. 2.57.

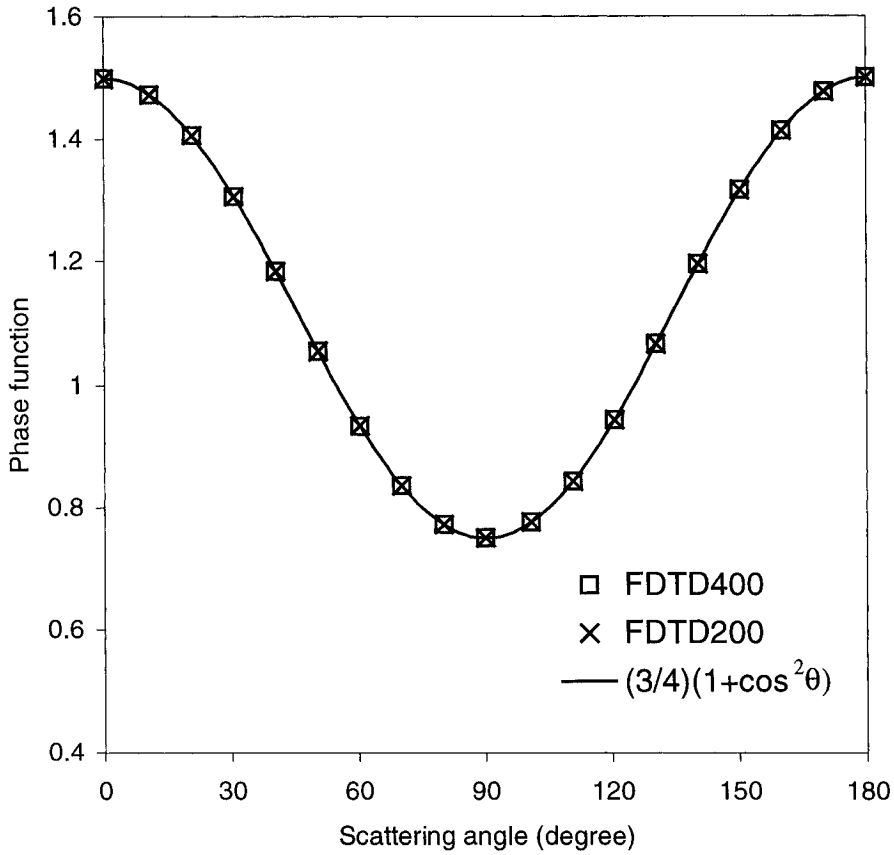

Figure 2.8: Phase function of a cubic FDTD cell (refractive index $7.14 + 2.89i$, FDTD grid spacing $\Delta s = \lambda / 200$ for FDTD200, and $\Delta s = \lambda / 400$ for FDTD400) computed using the FDTD method and analytical formula (Eq. (2.59)).

Table 2.5: Extinction and scattering cross sections computed using the Mie theory and the FDTD method for four refractive indices of a cubic FDTD cell (grid spacing $\Delta s = \lambda / 400$)

	Mie		FDTD		Relative Error (%)	
m	σ_{ext} (unit λ^2)	σ_{sca} (unit λ^2)	σ_{ext} (unit λ^2)	σ_{sca} (unit λ^2)	σ_{ext}	σ_{sca}
2.0 + 0i	4.542×10^{-14}	4.542×10^{-14}	4.507×10^{-14}	4.507×10^{-14}	-0.8	-0.8
1.33 + 0.01i	1.655×10^{-9}	7.569×10^{-15}	1.657×10^{-9}	7.768×10^{-15}	0.1	2.6
1.78 + 0.0024i	2.827×10^{-10}	3.198×10^{-14}	2.834×10^{-10}	3.192×10^{-14}	0.3	-0.2
7.14 + 2.89i	9.909×10^{-9}	1.690×10^{-13}	9.872×10^{-9}	1.665×10^{-13}	-0.4	-1.5

2.9 Summary

The finite-difference time-domain (FDTD) method provides a flexible method for calculations of scattering properties of irregular and inhomogeneous particles. The FDTD method is a direct discretization of the Maxwell curl equations. The FDTD algorithm involves a simple time marching iteration where electric fields and magnetic fields are updated alternately.

An incident source is injected in the computational domain by employing surface currents surrounding the particle or using the total/scattered field formulation where the computational space is divided into two zones: total field zone and scattered field zone. A connecting condition is performed at the boundary of the two zones.

A particle is modeled by assigning appropriate dielectric properties at grid points. Here local values of dielectric properties at the grid points are used.

The frequency domain fields are obtained by discrete Fourier transformation of the time domain fields. The frequency domain fields are then used to obtain scattering properties of the particle by volume integration or surface integration.

It is shown that the FDTD method gives accurate results for extinction, scattering, absorption, asymmetry factor and phase function.

The FDTD computer program developed here has been validated with the Mie theory (see chapter 4). Because very small spheres are of interest for testing the effective medium approximation (see chapter 6), a new approximation for very small spheres is given in this chapter.

Chapter 3

Multiple Absorbing Surfaces-Absorbing Boundary Condition

As mentioned in chapter 2 in order to apply the FDTD method, an absorbing boundary condition (ABC) is required for an open space problem or for a scattering problem. Although the perfectly matched layer method has been currently accepted as a standard method to truncate the FDTD method. Development of a new and improved ABC is still an active field. During the process of developing the FDTD method, a new method was developed, and it is called multiple absorbing surfaces (MAS) ABC. The MAS method is discussed in this chapter (sections 3.2-3.7).

3.1. One- and Two-Dimensional Maxwell Equations

For a two-dimensional problem where the electric and magnetic fields are independent of z coordinate, for transverse electric (TE) fields i.e. $\mathbf{E} = E_x\hat{\mathbf{x}} + E_y\hat{\mathbf{y}}$ and $\mathbf{H} = H_z\hat{\mathbf{z}}$, and for non-conductive medium, the time dependent Maxwell equations Eqs. (2.10) and (2.11) reduce to

$$\frac{\partial H_z}{\partial t} = \frac{1}{\mu}\left(\frac{\partial E_x}{\partial y} - \frac{\partial E_y}{\partial x}\right) \tag{3.1}$$

$$\frac{\partial E_x}{\partial t} = \frac{1}{\varepsilon}\frac{\partial H_z}{\partial y} \tag{3.2}$$

$$\frac{\partial E_y}{\partial t} = -\frac{1}{\varepsilon}\frac{\partial H_z}{\partial x} \tag{3.3}$$

Using Yee's method of differencing (see chapter 2) the above Eqs. (3.1)-(3.3) are discretized to

$$H_z^{n+\frac{1}{2}}(I+\tfrac{1}{2}, J+\tfrac{1}{2}) = H_z^{n-\frac{1}{2}}(I+\tfrac{1}{2}, J+\tfrac{1}{2}) + \frac{\Delta t}{\mu}\left\{\frac{1}{\Delta y}[E_x^n(I+\tfrac{1}{2}, J+1) - E_x^n(I+\tfrac{1}{2}, J)] - \frac{1}{\Delta x}[E_y^n(I+1, J+\tfrac{1}{2}) - E_y^n(I, J+\tfrac{1}{2})]\right\} \tag{3.4}$$

$$E_x^{n+1}(I+\tfrac{1}{2}, J) = E_x^n(I+\tfrac{1}{2}, J) + \frac{\Delta t}{\varepsilon \Delta y}[H_z^{n+\frac{1}{2}}(I+\tfrac{1}{2}, J+\tfrac{1}{2}) - H_z^{n+\frac{1}{2}}(I+\tfrac{1}{2}, J-\tfrac{1}{2})] \tag{3.5}$$

$$E_y^{n+1}(I, J+\tfrac{1}{2}) = E_y^n(I, J+\tfrac{1}{2}) + \frac{\Delta t}{\varepsilon \Delta x}[H_z^{n+\frac{1}{2}}(I-\tfrac{1}{2}, J+\tfrac{1}{2}) - H_z^{n+\frac{1}{2}}(I+\tfrac{1}{2}, J+\tfrac{1}{2})] \tag{3.6}$$

For simplicity, we first consider a one-dimensional wave propagation. For a one-dimensional problem with only non-zero E_y and H_z components, Eqs. (3.4)-(3.6) reduce to

$$H_z^{n+\frac{1}{2}}(I+\tfrac{1}{2}) = H_z^{n-\frac{1}{2}}(I+\tfrac{1}{2}) + \frac{\Delta t}{\mu \Delta x}[E_y^n(I, J+\tfrac{1}{2}) - E_y^n(I+1)]\} \tag{3.7}$$

$$E_y^{n+1}(I) = E_y^n(I) + \frac{\Delta t}{\varepsilon \Delta x}[H_z^{n+\frac{1}{2}}(I-\tfrac{1}{2}) - H_z^{n+\frac{1}{2}}(I+\tfrac{1}{2})] \tag{3.8}$$

3.2. Total-Field/Scattered-Field Formulation

One concept needed in developing the MAS method is the total-field/scattered-field formulation. In this formulation a virtual connecting surface is used to separate two regions: total-fields region and scattered-fields region. Consider two regions in a one-

dimensional FDTD simulation as shown in Fig. 3.1. In the left-hand region only the total fields are calculated and stored in computer memory and in the right-hand region only the scattered fields are calculated and stored. The total fields are defined as the sum of scattered and incident fields.

$$\mathbf{E}_{tot} = \mathbf{E}_{sca} + \mathbf{E}_{inc}, \quad \mathbf{H}_{tot} = \mathbf{H}_{sca} + \mathbf{H}_{inc} \tag{3.9}$$

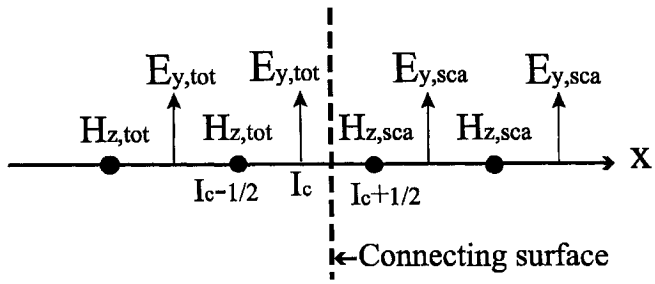

Figure 3.1: A one-dimensional FDTD mesh showing two regions (total-fields and scattered-fields regions) separated by a connecting surface.

By knowing exactly the incident fields, the scattered fields can be simulated in the scattered-fields region. Since the two regions have different fields, we have to impose a connecting condition at the connecting surface such that consistency between the two fields is ensured.

Equations (3.7) and (3.8) are used to calculate total fields and scattered fields in the two regions except at the connecting surface. The condition for consistency at the connecting surface can be determined by realizing that the fields are located in different regions. Let us consider the electric field located at I_c. It is updated by

$$E_{y,tot}^{n+1}(I_c) = E_{y,tot}^{n}(I_c) + \frac{\Delta t}{\varepsilon \Delta x}[H_{z,tot}^{n+\frac{1}{2}}(I_c - \tfrac{1}{2}) - H_{z,tot}^{n+\frac{1}{2}}(I_c + \tfrac{1}{2})] \tag{3.10}$$

Since $H_{z,tot}(I_c + \frac{1}{2})$ is located in scattered-field region, Eq. (3.9) is used.

$$H_{z,tot}(I_c + \tfrac{1}{2}) = H_{z,sca}(I_c + \tfrac{1}{2}) + H_{z,inc}(I_c + \tfrac{1}{2}) \tag{3.11}$$

After substitution, we have

$$\begin{aligned} E_{y,tot}^{n+1}(I_c) = E_{y,tot}^{n}(I_c) + \frac{\Delta t}{\varepsilon \Delta x}[H_{z,tot}^{n+\frac{1}{2}}(I_c - \tfrac{1}{2}) - H_{z,sca}^{n+\frac{1}{2}}(I_c + \tfrac{1}{2})] \\ - \frac{\Delta t}{\varepsilon \Delta x} H_{z,inc}^{n+\frac{1}{2}}(I_c + \tfrac{1}{2}) \end{aligned} \tag{3.12}$$

or

$$E_{y,tot}^{n+1}(I_c) = \{E_{y,tot}^{n+1}(I_c)\}_{\text{using (3.8)}} - \frac{\Delta t}{\varepsilon \Delta x} H_{z,inc}^{n+\frac{1}{2}}(I_c + \tfrac{1}{2}) \tag{3.13}$$

where $\{\}$ denotes Eqs. (3.7) or (3.8) are used. Similarly for the scattered field at $I_c + \frac{1}{2}$, the connecting condition is

$$H_{z,sca}^{n+\frac{1}{2}}(I_c + \tfrac{1}{2}) = \{H_{z,sca}^{n+\frac{1}{2}}(I_c + \tfrac{1}{2})\}_{\text{using (3.7)}} - \frac{\Delta t}{\mu \Delta x} E_{y,inc}^{n}(I_c) \tag{3.14}$$

Therefore, we apply Eqs. (3.7) and (3.8) to update the fields in both total-field and scattered-field regions and the connecting condition is imposed by re-updating the field using Eqs. (3.13) and (3.14).

Because we have imposed the connecting condition at the connecting surface, the incident fields that propagate in the positive x direction are absorbed by the surface leaving only scattered fields to be transmitted across the surface. In other words, the connecting surface acts as a filter that allows only scattered fields to propagate through the surface.

This concept of a connecting surface is very useful for constructing an ABC because we can think of the surface as an absorbing surface, which absorbs only the incident fields propagating through it. We can modify the above concept such that the connecting surface absorbs the total fields. This is done by replacing the incident fields by an approximation of the total fields ($E_{y,app}(I_c)$ and $H_{z,app}(I_c + \frac{1}{2})$). Then we have new connecting conditions given by:

$$E_{y,tot}^{n+1}(I_c) = \{E_{y,tot}^{n+1}(I_c)\}_{\text{using (3.8)}} - \frac{\Delta t}{\varepsilon \Delta x} H_{z,app}^{n+\frac{1}{2}}(I_c + \tfrac{1}{2}) \tag{3.15}$$

$$H_{z,sca}^{n+\frac{1}{2}}(I_c + \tfrac{1}{2}) = \{H_{z,sca}^{n+\frac{1}{2}}(I_c + \tfrac{1}{2})\}_{\text{using (3.7)}} - \frac{\Delta t}{\mu \Delta x} E_{y,app}^{n}(I_c) \tag{3.16}$$

With these conditions the connecting surface now acts as an absorbing surface where it only transmits the difference of the total field and the approximating field or the error of approximation. We can expect that the field in the scattered region will be very small when we have a good approximation for the total fields. The next step in constructing ABC is to define a suitable approximating function such that the connecting surfaces transmit small errors and without reflection.

3.3. Approximating Functions

Since the total fields propagate in the positive x direction the approximating field must be determined from fields in the total-fields region. In order to avoid an instability the approximating fields should be a function of linear combinations of the total fields, since a nonlinear function will produce a nonlinear response. For first order approximation three neighboring points $U^n(I)$, $U^n(I-1)$ and $U^{n+1}(I-1)$ (where U is the electric or magnetic fields, $I = I_c$ for electric field and $I = I_c + \frac{1}{2}$ for magnetic field) are used. Therefore first order approximation is of the form

$$U_{app}^{n+1}(I) = pU^n(I) + qU^{n+1}(I-1) + rU^n(I-1) \tag{3.17}$$

where p, q, and r are constant coefficients. Using this approximating function the fields are approximated by

$$E_{y,app}^{n+1}(I_c) = pE_{y,tot}^{n}(I_c) + qE_{y,tot}^{n+1}(I_c - 1) + rE_{y,tot}^{n}(I_c - 1) \tag{3.18}$$

and

$$\begin{aligned} H_{z,app}^{n+\frac{1}{2}}(I_c + \tfrac{1}{2}) = p[&H_{z,app}^{n-\frac{1}{2}}(I_c + \tfrac{1}{2}) + H_{z,sca}^{n-\frac{1}{2}}(I_c + \tfrac{1}{2})] \\ &+ qH_{z,tot}^{n+\frac{1}{2}}(I_c - \tfrac{1}{2}) + rH_{z,tot}^{n-\frac{1}{2}}(I_c - \tfrac{1}{2}) \end{aligned} \tag{3.19}$$

There are a number of schemes that can be used for determining the above coefficients. We can use an averaging method i.e. $p = q = r = 1/3$, a space-time extrapolation (e.g. $p = q = 0, r = 1$) and the first order Higdon annihilation operator (Higdon, 1986 and 1987). In this thesis the Higdon operator is used. The Higdon operator is found to have a higher accuracy than the other methods. It also simplifies the formulation since it can be easily implemented and it also provides enough parameters for wide variety of applications making the MAS method very flexible.

The first Higdon operator used to absorb an incident wave at angle α is given by (Higdon, 1986 and 1987)

$$[\cos(\alpha)\frac{\partial}{\partial t} + c\frac{\partial}{\partial z} + \beta]U = 0 \tag{3.20}$$

where c is the speed of wave in the medium and β is nonnegative number introduced to ensure stability (Higdon, 1987). The parameter β can also be used to absorb evanescent

waves (Fang, 1994).

Discretization of the Higdon operator by the central difference scheme produces coefficients given by

$$p = \frac{\cos(\alpha)\Delta z - c\Delta t - \beta\Delta t\Delta z/2}{\cos(\alpha)\Delta z + c\Delta t + \beta\Delta t\Delta z/2} \tag{3.21a}$$

$$q = -\frac{\cos(\alpha)\Delta z - c\Delta t + \beta\Delta t\Delta z/2}{\cos(\alpha)\Delta z + c\Delta t + \beta\Delta t\Delta z/2} \tag{3.21b}$$

$$\mathrm{r} = \frac{\cos(\alpha)\Delta z + c\Delta t - \beta\Delta t\Delta z/2}{\cos(\alpha)\Delta z + c\Delta t + \beta\Delta t\Delta z/2} \tag{3.21c}$$

3.4. Transmission Functions

In order to know how effective the approximating function is, we need to investigate the transmission of the connecting surface. An incident wave travelling in positive x direction is given by

$$U_{tot}^{n}(I) = A\exp(ikI\Delta x - i\omega n\Delta t) \tag{3.22}$$

where A is the amplitude of wave and k and ω are the wave number and angular frequency of wave. The transmitted wave is given as the difference between the incident wave and the approximating wave.

$$U_{\mathrm{sca}}^{\mathrm{n+1}}(I) = U_{tot}^{n+1}(I) - U_{app}^{n+1}(I) \tag{3.23}$$

Substituting Eq. (3.17) into Eq. (3.23), we have

$$U_{tot}^{n+1}(I) - pU_{tot}^{n}(I) - qU_{tot}^{n+1}(I-1) - rU_{tot}^{n}(I-1) = U_{sca}^{n+1}(I) \tag{3.24}$$

The transmitted wave is in the form of

$$U_{sca}^{n}(I) = TA\exp(ikI\Delta x - i\omega n\Delta t) \tag{3.25}$$

After substitution of Eqs. (3.25) and (3.22) into Eq. (3.24) and after a manipulation the transmission is equal to

$$T(+) = 1 - p\exp(i\omega\Delta t) - q\exp(-ik\Delta x) - r\exp(-ik\Delta x + i\omega\Delta t) \tag{3.26}$$

Here we use $(+)$ to indicate the transmission in positive x direction.

For the case of a wave travelling in negative x direction, the transmission is determined by using the fact that a wave travelling in a negative x direction is exactly the

same as the wave travelling in a positive x direction provided that the time runs backward. Using the same previous analysis, for backward time direction the incident wave is now given by $U_{sca}^{n}(I)$ and the transmitted wave is $U_{tot}^{n}(I)$.

the waves travelling in negative x direction are in the form of

$$U_{sca}^{n}(I) = A\exp(-ikI\Delta x - i\omega n\Delta t) \tag{3.27}$$

and

$$U_{tot}^{n}(I) = TA\exp(-ikI\Delta z - i\omega n\Delta t) \tag{3.28}$$

After substitutions of Eqs. (3.27) and (3.28) into Eq. (3.24), the transmission is now given by

$$T(-) = 1/[1 - p\exp(i\omega\Delta t) - q\exp(ik\Delta x) - r\exp(ik\Delta x + i\omega\Delta t)] \tag{3.29}$$

Similarly $(-)$ denotes for the transmission of a wave travelling in the negative x direction.

3.5. Preliminary Numerical Simulations

A one-dimensional FDTD simulation is performed to test the concept of a connecting surface for the absorbing boundary. In this simulation, the spatial spacing and temporal increment is taken to be $\Delta x = 1.5$ cm (it is $\lambda/20$ at 1 GHz frequency) and $\Delta t = \Delta x/2c = 25$ ps, where λ and c are the wavelength and speed of light in the medium. In this numerical experiment we take a vacuum as the medium. The connecting surface uses approximating function Eqs. (3.17) and (3.21) with parameters $\alpha = 0$ and $\beta = 0$. Fig. 3.2a shows a Gaussian pulse generated at the left-hand boundary which then propagates in the positive x direction. The pulse then propagates through the connecting surface in which the pulse is absorbed leaving small-transmitted fields as shown in Fig. 3.2b. However, for a pulse propagating in a negative direction (see Fig. 3.3a) is amplified when it passes the connecting surface (see Fig. 3.3b).

Using the same parameters, another numerical experiment is done to investigate the transmission of the connection surface. In this simulation a Gaussian pulse source and the discrete Fourier transform (DFT) scheme are used here to calculate the frequency component for the incident field and the transmitted field. The spatial length in this

simulation is taken large enough such that the transmitted field is not reflected by the boundary during the simulation.

A comparison of results from the FDTD simulation and from the theoretical transmissions (Eqs. (3.25) and (3.29)) is shown in Fig. 3.4. The numerical FDTD results show good agreements with the theoretical transmissions. We note in Fig. 3.4b that the transmission for negative x direction $T(-)$ increases as the frequency decreases. It approaches infinity when the frequency approaches zero. This can be noted from Eq. (3.29) where the denominator approaches zero as frequency decreases. Therefore large amplification is present for low frequency waves in negative x direction. This amplification is reduced when we use a positive nonzero parameter β.

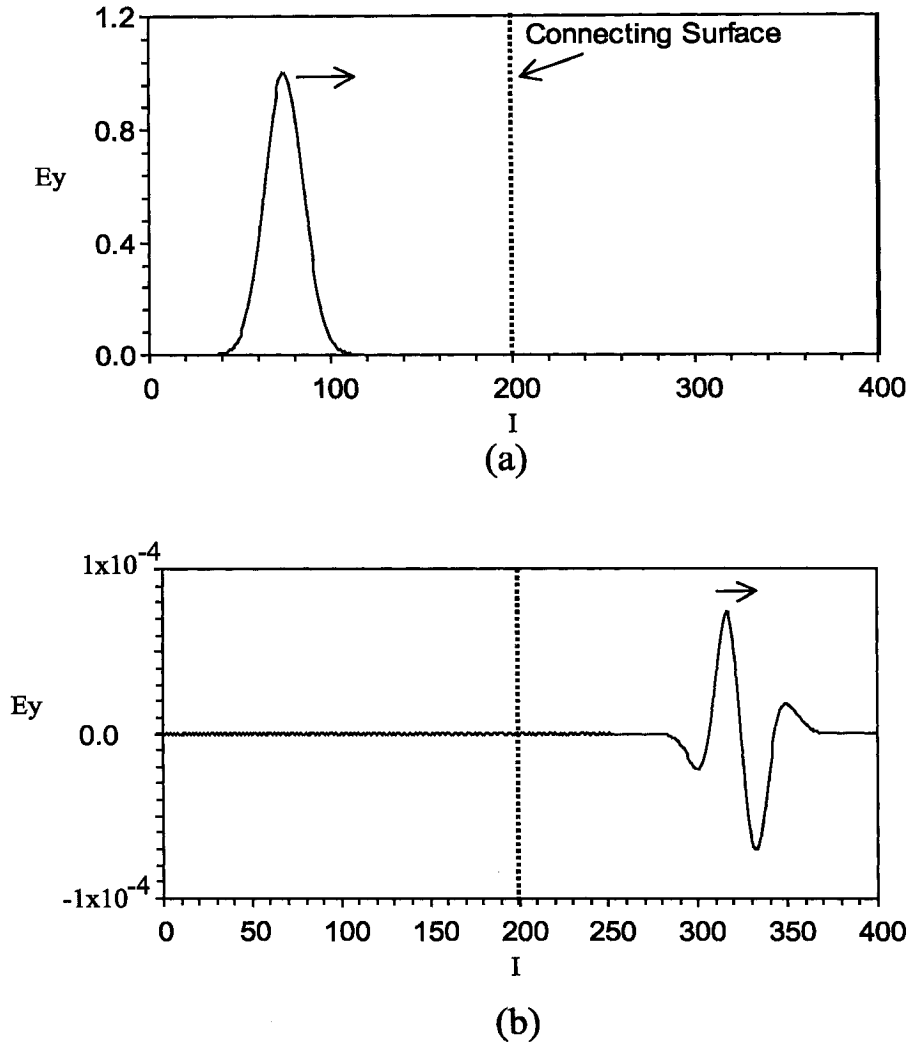

Figure 3.2: One-dimensional FDTD simulations of a Gaussian pulse propagating through a connecting surface: (a) an incidence pulse in the positive x direction, (b) a transmitted pulse. The connecting surface uses approximating function Eqs. (3.17) and (3.21) with parameters $\alpha = 0$ and $\beta = 0$.

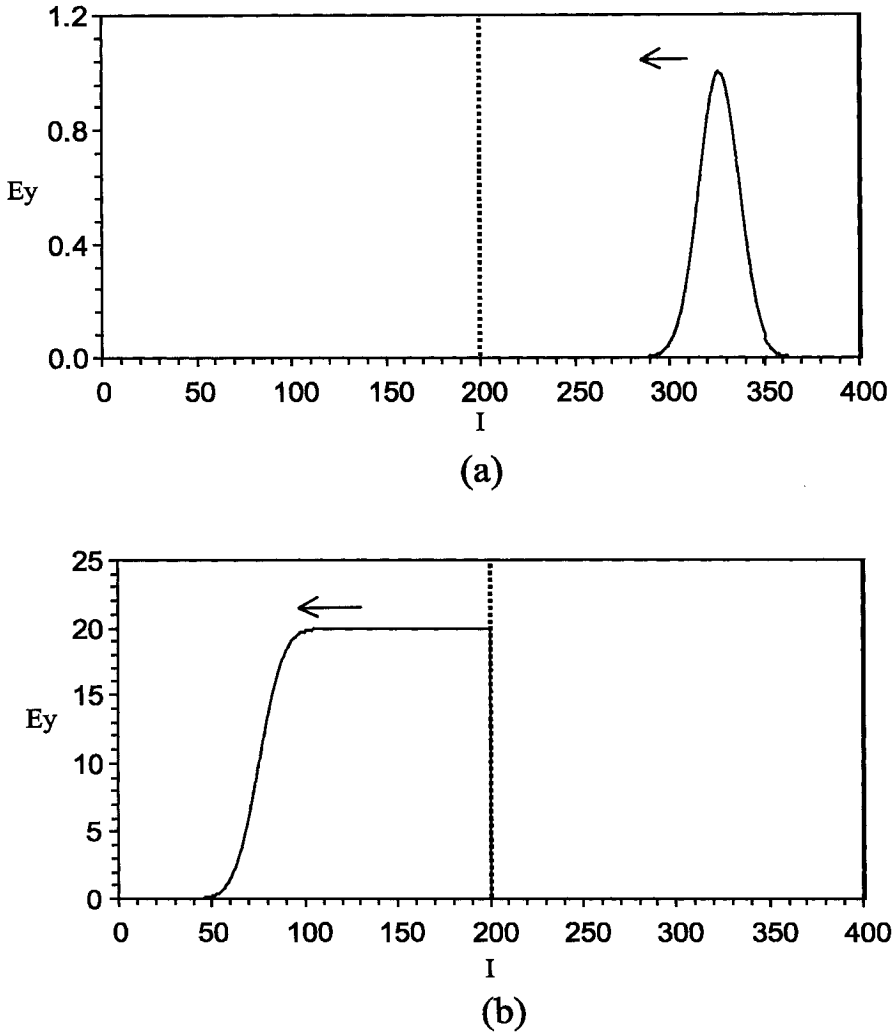

Figure 3.3: One-dimensional FDTD simulations of a Gaussian pulse propagating through a connecting surface: (a) an incidence pulse in the negative x direction, (b) a transmitted pulse, The connecting surface uses approximating function Eqs. (3.17) and (3.21) with parameters $\alpha = 0$ and $\beta = 0$.

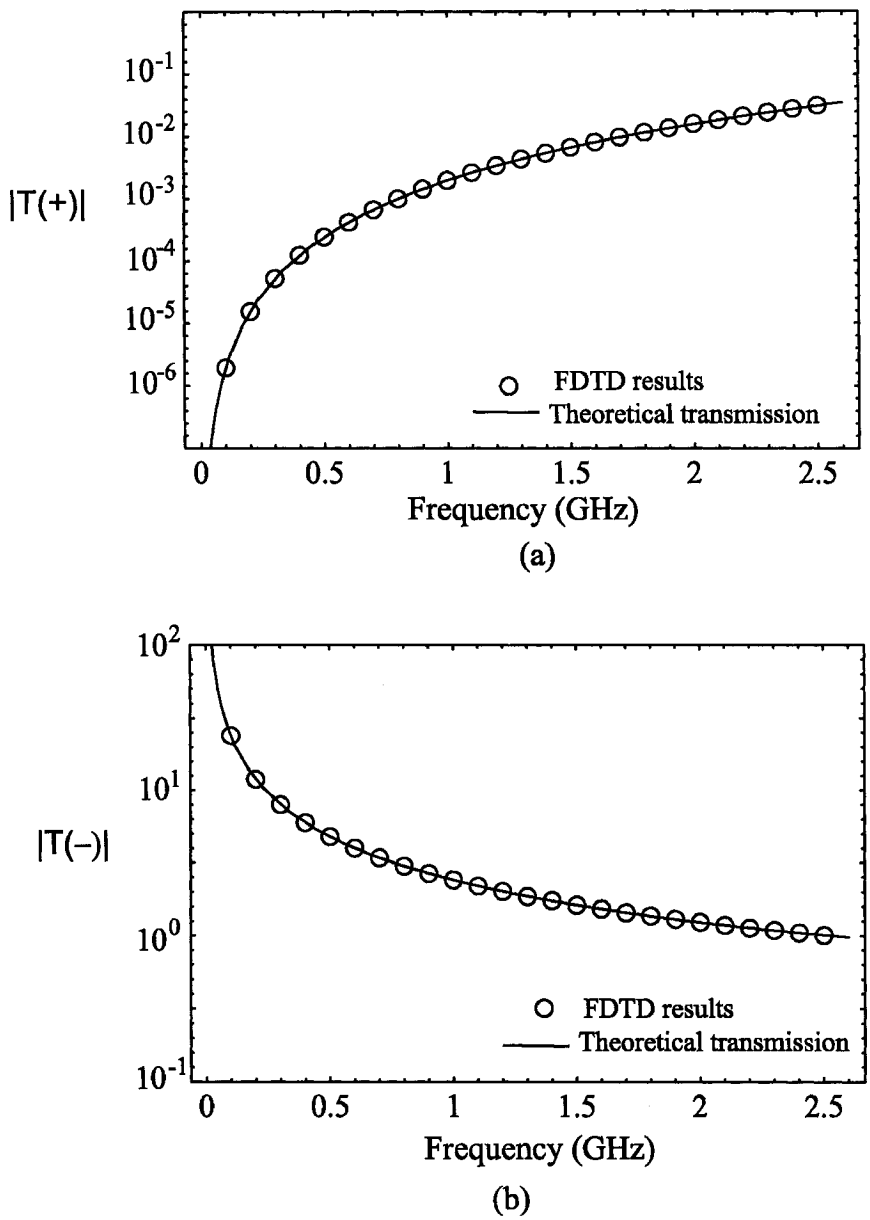

Figure 3.4: FDTD results and theoretical transmissions of connecting surface as a function of angular frequency for wave travelling in (a) the positive x direction and (b) the negative x direction. T(+) and T(−) is the transmission for the positive and the negative x directions.

As shown in Fig. 3.4b for a wave travelling in the negative x direction, the transmission is large. To reduce the amplification for wave travelling in the negative direction we construct another surface on the left side of the connecting surface as shown in Fig. 3.5. With this additional surface, the region between the two connecting surfaces is the total fields region. We can note that the second surface (S2) is an exact mirror to the first surface (S1). Therefore, the properties of the second surface (S2) are the opposite of the first surface (S1). There are some advantages when using this pair of surfaces. The first advantage is that the resultant transmission is small regardless of the direction of incident waves. This is important for maintaining the stability of the method. Beside that, for this pair of surfaces we need only to store two additional variables for two connecting surfaces, therefore the number of FDTD cells needed for the MAS boundary is kept to a minimum.

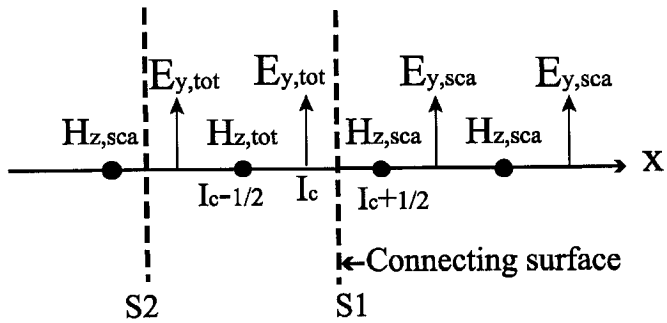

Figure 3.5: A one-dimensional FDTD mesh showing two connecting surfaces which separate three regions (total-fields (middle) and two scattered-fields regions).

The connecting conditions for the second surface are

$$E_{y,tot}^{n+1}(I_c-1)=\{E_{y,tot}^{n+1}(I_c-1)\}_{\text{using (3.8)}}+\frac{\Delta t}{\varepsilon\Delta z}H_{z,app}^{n+\frac{1}{2}}(I_c-\tfrac{3}{2}) \tag{3.30}$$

$$H_{z,sca}^{n+\frac{1}{2}}(I_c-\tfrac{3}{2})=\{H_{z,sca}^{n+\frac{1}{2}}(I_c-\tfrac{3}{2})\}_{\text{using (3.7)}}+\frac{\Delta t}{\mu\Delta z}E_{y,app}^{n}(I_c-1) \tag{3.31}$$

and the approximation functions are given by

$$E_{y,app}^{n+1}(I_c-1)=pE_{y,tot}^{n}(I_c-1)+qE_{y,tot}^{n+1}(I_c)+rE_{y,tot}^{n}(I_c) \tag{3.32}$$

and

$$\begin{aligned}H_{z,app}^{n+\frac{1}{2}}(I_c-\tfrac{3}{2})=p[&H_{z,app}^{n-\frac{1}{2}}(I_c-\tfrac{3}{2})+H_{z,sca}^{n-\frac{1}{2}}(I_c-\tfrac{3}{2})]\\&+qH_{z,tot}^{n+\frac{1}{2}}(I_c-\tfrac{1}{2})+rH_{z,tot}^{n-\frac{1}{2}}(I_c-\tfrac{1}{2})\end{aligned} \tag{3.33}$$

The resulted transmission for the pair of surfaces is

$$T = \frac{1 - p\exp(i\omega\Delta t) - q\exp(-ik\Delta x) - r\exp(-ik\Delta x + i\omega\Delta t)}{1 - p\exp(i\omega\Delta t) - q\exp(ik\Delta x) - r\exp(ik\Delta x + i\omega\Delta t)} \tag{3.34}$$

An illustration of a pair of surfaces in two dimensions is shown in Fig. 3.6. The connecting conditions Eqs. (3.15), (3.16), (3.30), and (3.31) and approximating functions Eqs. (3.18), (3.19), (3.32) and (3.33) can be used directly for the two-dimensional case by replacing the index (I) with $(I, J+\frac{1}{2})$ in the expressions. Other connecting conditions for y plane can be derived in similar way as previous discussion.

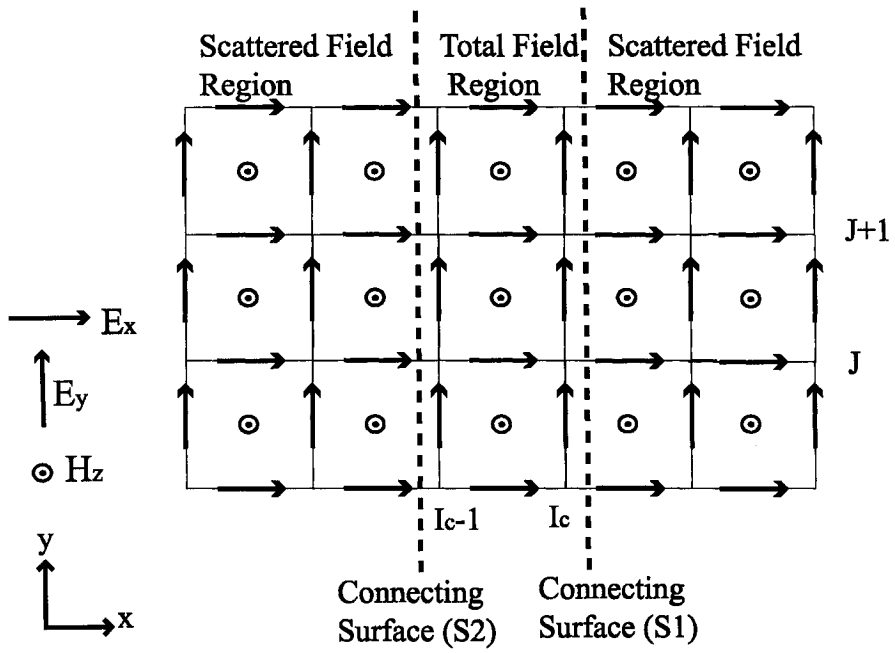

Figure 3.6: A two-dimensional FDTD mesh consists of three regions separated by connecting surfaces.

Generalization of the transmission function Eq. (3.34) in the two and three dimensions is done by replacing the wave number k in Eq. (3.34) with the component of wave number in the x direction $k_x = k\cos(\theta)$ where θ is the incident angle from the x axis. The transmission for two- or three-dimensional case is

$$T(\theta) = \frac{1 - p\exp(i\omega\Delta t) - q\exp(-ik\cos(\theta)\Delta x) - r\exp(-ik\cos(\theta)\Delta x + i\omega\Delta t)}{1 - p\exp(i\omega\Delta t) - q\exp(ik\cos(\theta)\Delta x) - r\exp(ik\cos(\theta)\Delta x + i\omega\Delta t)} \tag{3.35}$$

Before constructing the MAS boundary we first observe the properties of a pair of MAS surfaces. An FDTD simulation is performed to investigate the transmission

characteristic of the pair of MAS surfaces. In this experiment 200x200 FDTD grid cells is constructed. The spatial and temporal increments used here are $\Delta x = \Delta y = 1.5$ mm and $\Delta t = \Delta x / 2c = 2.5$ ps. There is no lost of generality if we take a medium to be a vacuum. A Gaussian pulse is generated at the center of the computational space. The Gaussian pulse is $H_z(100,100) = \exp(-((n-150)/30)^2)$. The pair of absorbing surfaces is located 10 cells away from the Gaussian source. The MAS parameters for the pair surfaces are $\alpha = \beta = 0$. The magnitude of the magnetic field distribution after n=300 time steps is shown in Fig. 3.7. We can note here that the circular contours at the left-hand side region are not affected by the presence of MAS surfaces. Observation of the magnetic fields show that the reflection caused by the MAS surfaces is exactly zero.

We note that the transmission of MAS depends on the direction of incident wave. Fig. 3.7 shows very small transmission for the forward direction and there is significant transmission at large incident angle. This corresponds to the choice of Higdon's parameters used in this simulation where the operator annihilates waves in forward direction ($\alpha = 0$).

In order to know the angle dependence of transmission numerically we performed another experiment. The configuration of this experiment is shown in Fig. 3.8. We used a plane source generated near the MAS surfaces using the virtual connecting surface or Huygens surface method. We observed the evolution of the field at position P which is located near the MAS surfaces. The length of virtual surface and the position P are adjusted in such a way that there are no undesired fields from B1 and B2 disturbing the desired fields. Discrete Fourier Transform (DFT) is used here to obtain the frequency component of transmission. We also selected carefully the duration of time for the DFT such that the undesired fields (from B1 and B2) are excluded. The FDTD and MAS parameters are the same as in the previous simulation. The incident plane wave uses a band pass Gaussian pulse with a Fourier spectrum symmetrical about frequency f_o = 10 GHz given by $H_i = \exp[-((n-150)/30)^2]\sin(2\pi f_o(n-150)\Delta t)$.

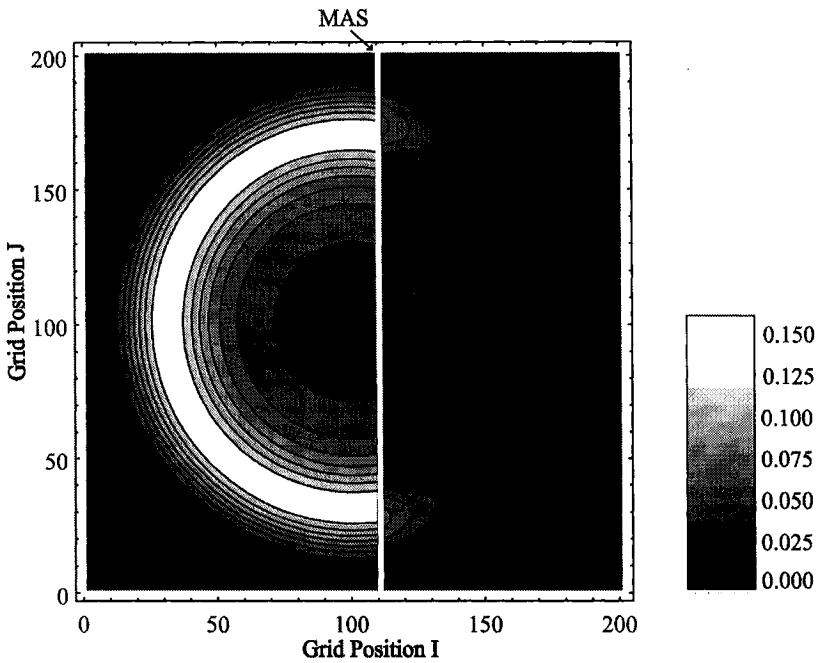

Figure 3.7: The magnitude of magnetic fields $|H_z|$ distribution after n=300 time steps with a Gaussian pulse generated at a grid position (100,100). A pair of MAS surfaces is located 10 cells away from the source.

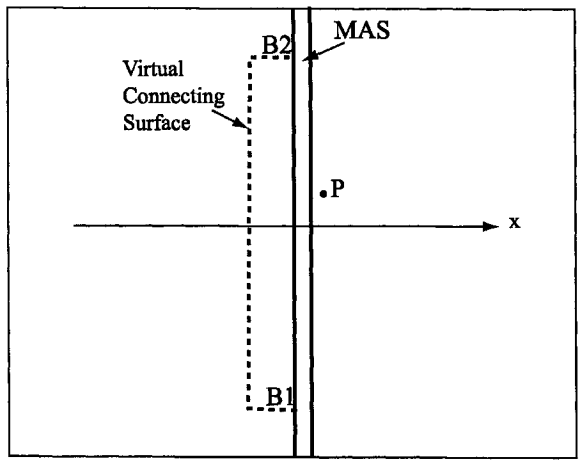

Figure 3.8: A configuration of FDTD simulation of a plane wave incident on a pair of MAS surfaces.

The numerical results as shown in Fig. 3.9 agree with the theoretical transmission Eq. (3.35). The theoretical and numerical transmissions for $\alpha = 0^\circ$ show the zero transmission is shifted to a larger angle instead of angle $= 0^\circ$. The shift is caused by the discretization of the Higdon operator. The MAS parameters can be adjusted such that the

desired absorption is achieved for any specified mesh discretization. A discussion of the adjustment procedure can be found in (Prescott & Shuley, 1997).

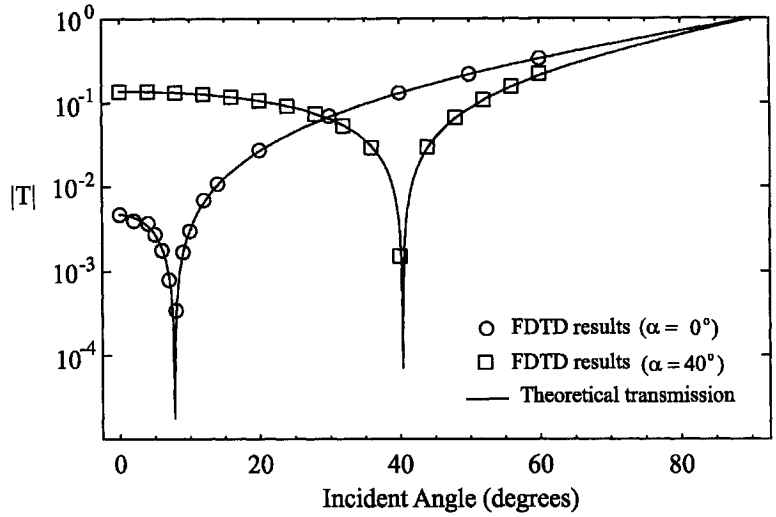

Figure 3.9: Numerical and theoretical transmission of a pair of MAS surfaces as a function of incident angle. The MAS parameters are $\alpha = 0°, \beta = 0$ and $\alpha = 40°, \beta = 0$.

We can note here that the MAS surfaces can be tuned to absorb at desired incident angle by selecting the appropriate angle α. We can construct a number of MAS surfaces with different parameter α such that the MAS surfaces absorb for wide range incident angles.

The previous analysis is mainly concentrated on propagating waves. It is found that the transmission function Eq. (3.35) can also be used for an analysis in the case of evanescent wave. This is done by changing the real wave number k_x to complex wave number $k_x = k_{x,re} + ik_{x,im}$, where $k_{x,re}$ and $k_{x,im}$ are real and imaginary parts. Choosing the value of $\cos(\alpha) = 0$ and nonzero positive values of β, it is shown that the Higdon's operator can absorb evanescent wave (Fang, 1994). The optimum value of β depends on the imaginary part of the wave number.

By selecting appropriately the MAS parameters α and β, we can construct MAS surfaces that absorb both propagating waves and evanescent waves. The choice of MAS parameters makes the MAS method very flexible. It is also possible to vary the speed of light c in the Higdon's operator. This variation and with appropriate connecting conditions modify the MAS method which also absorbs propagating waves in a

dispersive medium. Moreover by choosing an appropriate value of β, the MAS can also absorb propagating waves in an absorbing medium.

Because the MAS method is based on the application of the connecting surfaces or Huygens surfaces. The MAS method can be applied to other coordinate systems such as cylindrical and spherical coordinates.

3.6. Constructing ABC

The analysis of the pair of MAS has been discussed and the numerical results also agree with the theory. The MAS is now ready to be applied as an ABC. We put the pair of MAS surfaces at the outer computational boundaries. The outer most boundaries are truncated by a perfectly electric conductor (PEC) as shown in Fig 3.10. Other ABCs such as the PML may also be used instead of the PEC boundary. We note that there is an overlap between the MAS surfaces at the corner region. The overlap region does not cause inconsistencies in the connecting conditions. Therefore it does not produce any errors in the simulation. FDTD simulations show that there is no reflection caused by the overlap region. The analysis of MAS surfaces can be done separately without considering the overlap region.

Because the outgoing waves pass through a pair of MAS twice before the waves re-enter the computational domain, the reflection of the pair of MAS and the PEC structure is given by

$$R = -\left[\frac{1 - p\exp(i\omega\Delta t) - q\exp(-ik\cos(\theta)\Delta x) - r\exp(-ik\cos(\theta)\Delta x + i\omega\Delta t)}{1 - p\exp(i\omega\Delta t) - q\exp(ik\cos(\theta)\Delta x) - r\exp(ik\cos(\theta)\Delta x + i\omega\Delta t)}\right]^2 \qquad (3.36)$$

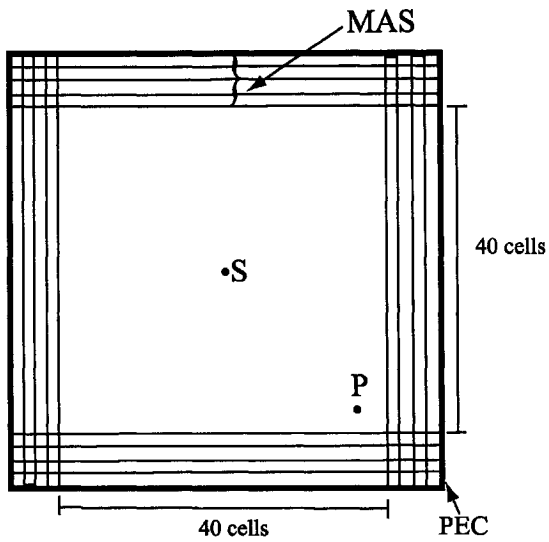

Figure 3.10: A square 40x40 cells computational domain with the MAS and PEC boundary. A band pass Gaussian source generated at S. The field is observed at point P.

The reflection coefficient (Eq. 3.36) is exactly the reflection of the second order Higdon ABC (Prescott & Shuley, 1997). This is expected since the Higdon operator is used for the approximating function. The negative sign is added because of the reflection from the PEC boundary. Adding an additional pair of surfaces lessen the reflection of ABC. This is similar to higher order Higdon ABC. Therefore we can add many absorbing surfaces until the desired reflection is achieved. Moreover, we can also use a combination of different approximating functions for the surfaces such that the resulted ABC provides good accuracy and stability for wide applications. Because we can construct multiple of surfaces, this ABC is called Multiple Absorbing Surface (MAS) ABC. For 2N surfaces or N-pair of surfaces, the reflection factor is

$$R = -\prod_{j=1}^{N}\left[\frac{1 - p_j \exp(i\omega\Delta t) - q_j \exp(-ik\cos(\theta)\Delta x) - r_j \exp(-ik\cos(\theta)\Delta x + i\omega\Delta t)}{1 - p_j \exp(i\omega\Delta t) - q_j \exp(ik\cos(\theta)\Delta x) - r_j \exp(ik\cos(\theta)\Delta x + i\omega\Delta t)}\right]^2$$

(3.37)

The MAS method may be thought as a different way for implementing the higher order one-way wave operators in the FDTD program. The MAS method may also be thought to be the same as the higher order Higdon operators. However there are some differences. First, the MAS-ABC consists of pair of surfaces. Each pair of surfaces can be analyzed separately without consideration of the other pairs. Each pair of surfaces

corresponds to a second order Higdon operator. Therefore, we may think that the MAS method consists of multiple second order Higdon operators. Second, it was shown that the second order Higdon operator is stable (Higdon, 1986 and 1987). As a consequence, the MAS method or the multiple second order operators is also stable. This is in contrast to the higher order Higdon operators, which employs a parameter β to stabilize the method (Higdon, 1987). It is shown later from numerical results that the MAS method is stable even though the parameter $\beta = 0$ is used.

Instead of MAS surfaces constructed in pairs, we can also construct an ABC without the pairing configuration. It is shown later (Fig. 3.12) that without the pairing configuration the MAS is unstable. This is mainly due to a large amplification that has been shown in Fig. 3.3.

3.7. Numerical Results

To investigate the performance of the MAS boundary, we consider here a square computational domain (40x40 cells). We construct the MAS and the PEC boundary as illustrated in Fig. 3.10. A band pass Gaussian source is used and placed at the center of computational domain. We observed the temporal variation of magnetic field at position P located at the corner 2 cells away from the MAS boundary. The MAS and FDTD parameters are the same as in the previous simulation where $\Delta x = \Delta y = 1.5\,\text{mm}$, $\Delta t = 2.5\,\text{ps}$ and $\alpha_j = \beta_j = 0$ (where $j = 1, 2, 3, \cdots$, is index of a pair of MAS). The magnetic fields obtained at P are compared with the reference fields obtained from the simulation with large computational domain in which the reflection caused by the outer boundary is not present in the calculation. For comparison we define the relative error as

$$\text{Relative Error} = \frac{\left|H^n_{z,ref}(I,J) - H^n_z(I,J)\right|}{\max\{\left|H^n_{z,ref}(I,J)\right|\}} \tag{3.38}$$

where $H_z(I,J)$ is the field obtained at P with the MAS boundary and $H_{z,ref}(I,J)$ is the reference field at P and max{ } represents a maximum value.

We performed simulations for different numbers of the MAS surfaces. The results

for two, six and ten surfaces are shown in Fig. 3.11. We note that the relative error decreases as the number of MAS surfaces increases. For six and ten surfaces the relative error is reasonably small. It is therefore suitable for application in an FDTD simulation. We also observe that after long duration of simulation time (see Fig. 3.11) the paired MAS is found to be stable even though we used $\beta_j = 0$ for the Higdon parameter. In contrast to the unpaired MAS, it is found to be unstable (see Fig. 3.12).

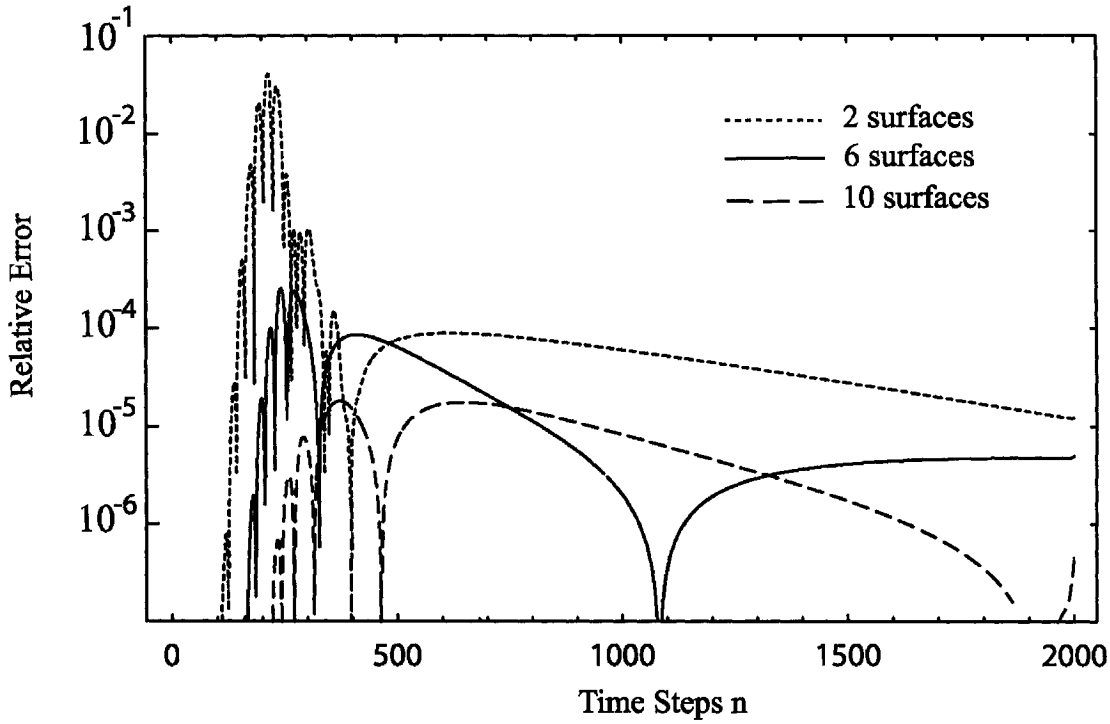

Figure 3.11: The relative errors for different number of surfaces at point P. The MAS parameters are $\alpha_j = \beta_j = 0$ (where $j = 1, 2, 3, \cdots$, is index of a pair of MAS).

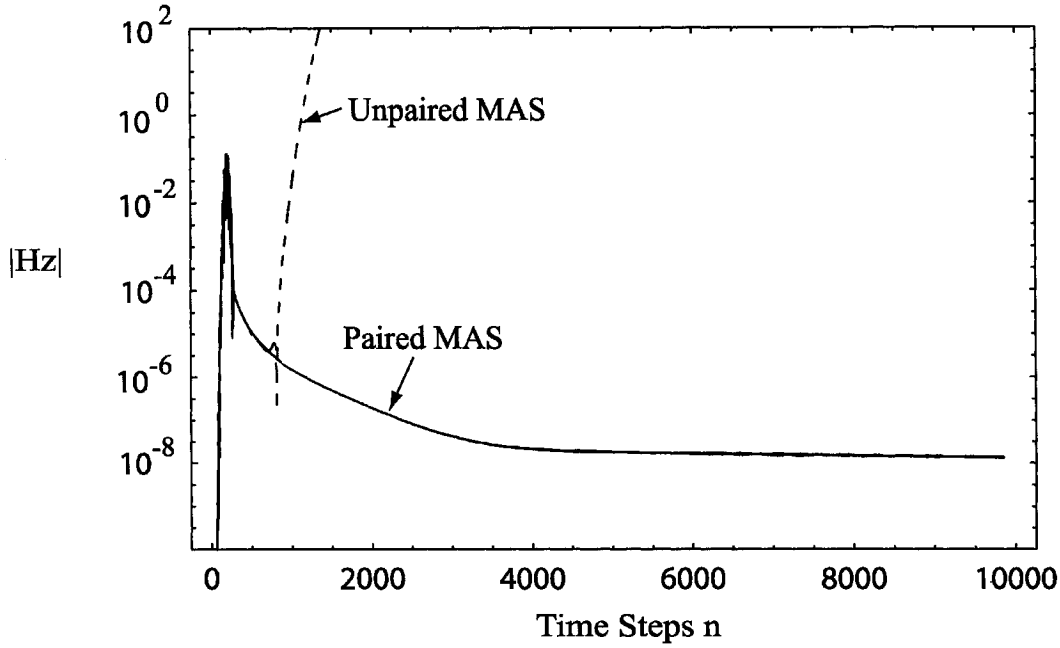

Figure 3.12: The value of magnetic field at point P for ten MAS surfaces (with paired and unpaired configuration). The MAS parameters are $\alpha_i = \beta_i = 0$.

Using the same geometry, we performed an FDTD numerical experiment with the PML-ABC. We use here 6-cell and 10-cell PML. The PML layers use a cubic conductivity profile with the maximum conductivity chosen such that the theoretical normal reflection is $R(0) \approx 10^{-4}$ for the 6-cell PML and $R(0) \approx 10^{-7}$ for the 10-cell PML. The number of cells needed for the MAS boundary is the same as the number of MAS surfaces. Therefore we compared the 6-cell PML with 6-surface MAS, and similarly for the 10-cell PML. We use two sets of MAS parameters $\alpha_j = \beta_j = 0$ and $\alpha_j = 0, \beta_j = 0.2(j-1)$ (where $j = 1,2,3...,$ is the integer index of a pair of MAS). The relative errors of the numerical results at point P are shown in Fig. 3.13. It is noted that the 6-surface MAS has lower maximum relative errors compared to the 6-cell PML. However the 10-surface MAS with $\alpha_j = \beta_j = 0$ has higher the relative errors compared to the 10-cell PML. We can improve the MAS boundary by selecting different parameters α and β. An improvement is shown by the lowest maximum of the relative errors when we use $\alpha_j = 0$ and $\beta_j = 0.2(j-1)$. Further numerical experiments are needed to optimize the properties of the MAS boundary. In general the MAS method has shown

considerable high accuracy for a small number of surfaces and it also has been shown to have accuracy comparable to or better than the PML method.

It has been shown in Fig. 3.13 that 6-surface MAS has a good accuracy for practical applications. To show that the MAS method is applicable to scattering problems, we preformed a three-dimensional FDTD simulation with MAS ABC. The connecting conditions and the approximating functions for three-dimensional case can be determined in similar way as previous discussion. The extension in three dimension of the MAS method is done easily. For a comparison, we consider scattering by a spherical particle. The FDTD method is truncated by two methods: the PML and the MAS method. Here, the PML method is used as a reference. The free space between the spherical particle and the PML or the MAS ABC is four cells. The MAS surfaces can be put close to the object without affecting its accuracy. Many comparisons show that MAS method has comparable accuracy to the PML. An example of the comparisons between the MAS and the PML is shown in Fig. 3.14. In this figure shows a phase matrix S11 of a spherical particle with size parameter $x = 2\pi a / \lambda = 1$ (where a is a radius of a sphere) using the PML and the MAS method. It is noted that the MAS (with six surfaces) show very close results to the PML. Therefore we can conclude that the MAS has shown a considerable accuracy such that it is suitable for an FDTD method.

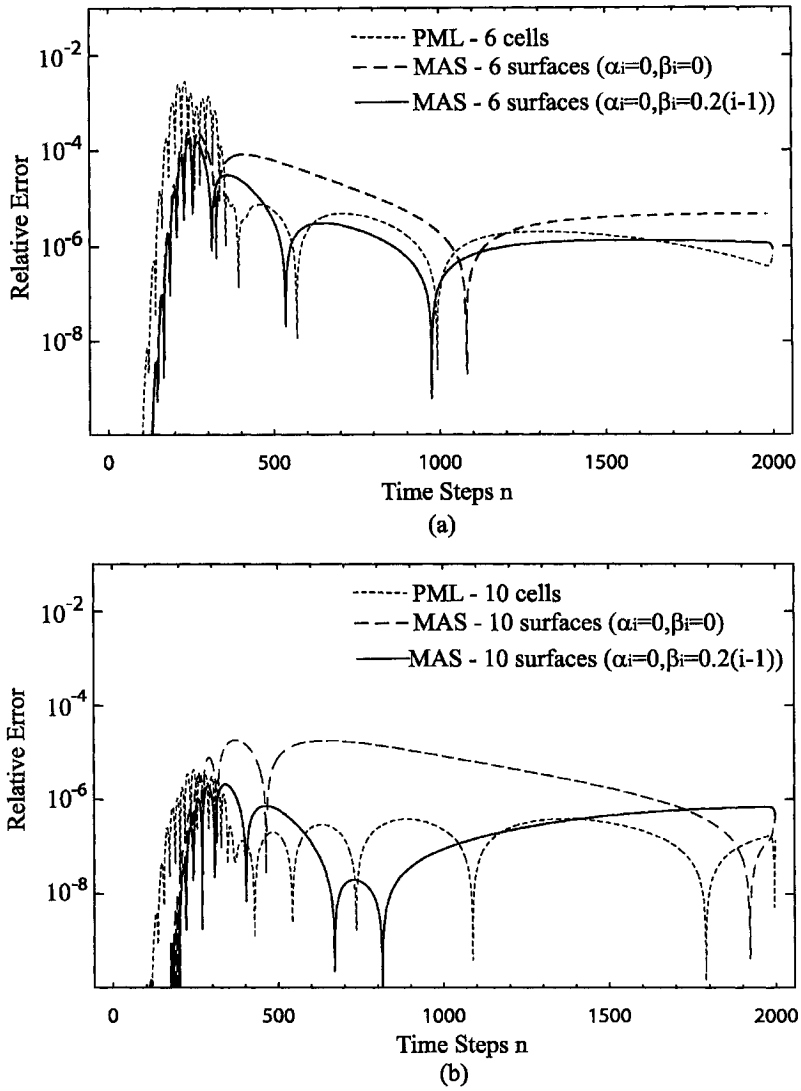

Figure 3.13: The relative errors of fields at point P for the MAS and the PML method.

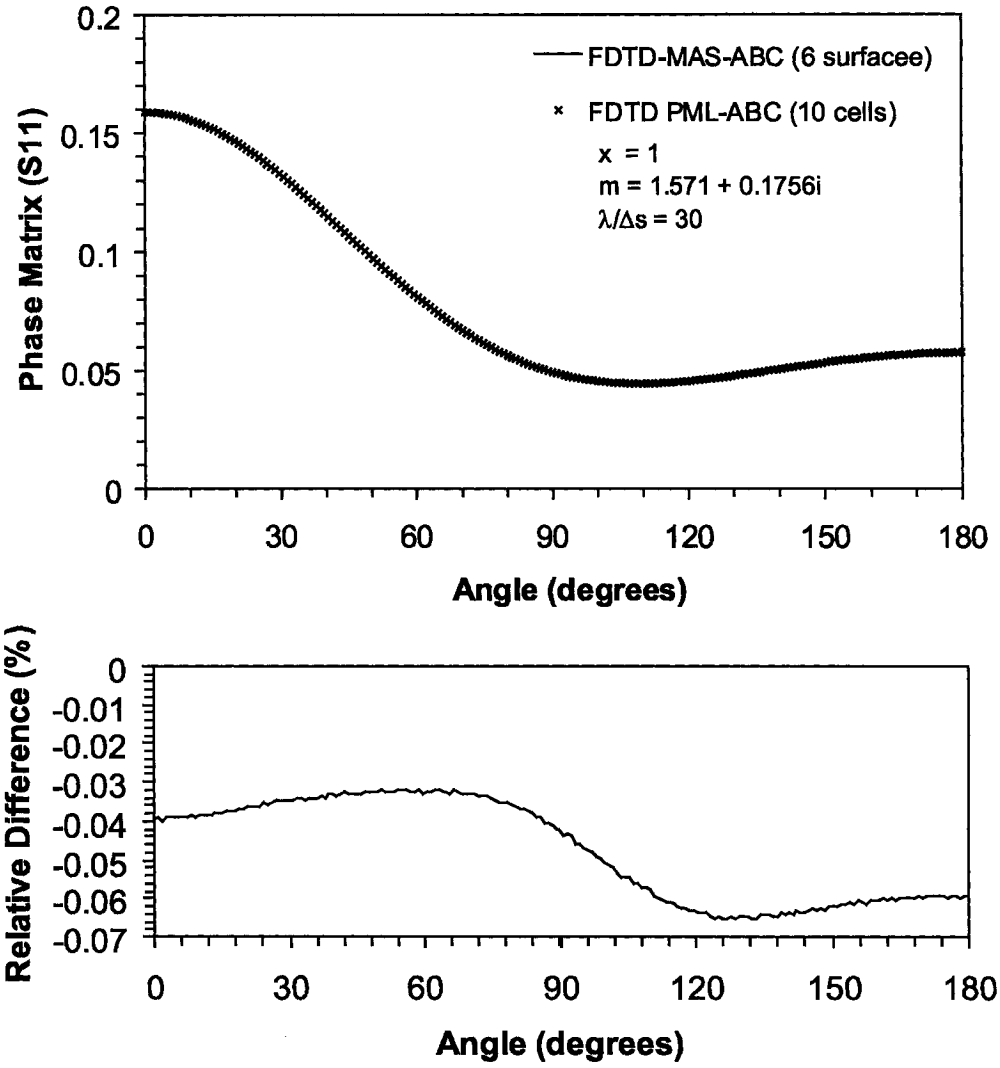

Figure 3.14: A comparison of phase functions (S11) resulted from FDTD calculations using the MAS ABC and the PML ABC.

3.8 Summary

A new absorbing boundary condition (ABC) which is called multiple absorbing surfaces (MAS) has been developed. The MAS-ABC uses the total-field/scattered-field FDTD formulation or the Huygens surface method. The MAS also uses a linear approximating function to obtain fields at the Huygens surface. The MAS can be easily added in the FDTD code. Numerical simulations have shown that the MAS-ABC has a comparable accuracy to the perfectly matched layer (PML) method.

There are some advantages in using the MAS method over the PML method. The advantages include the application of the MAS method for propagating and evanescent waves in various media such as lossy and dispersive medium. The MAS method can also be used to improve other ABCs, since the MAS method can be combined easily with other ABCs. Because the Huygens surface can be inserted in many different coordinate systems, the MAS method also can also be applied to other coordinate systems.

Chapter 4

Mie Scattering Formalism in Absorbing Medium

Light scattering by a spherical particle embedded in a homogenous non-absorbing medium is described by Mie scattering formalism (Bohren & Huffman, 1983; van de Hulst, 1957; Kerker, 1969). Several authors attempted to generalize the Mie theory for a case of spherical particle embedded in an absorbing medium (Chýlek, 1977; Mundy et al., 1974; Lebedev et al., 1999; Quinten & Rostalski, 1996; Sudiarta and Chýlek, 2001a; Fu and Sun, 2001; Bohren and Gilra, 1979). Mundy et al. (1974) and Chýlek (1977) extended the Mie theory to take into account the effect of absorbing medium by using a far field approximation of the Mie solution. They also integrated the radiative fluxes over a large sphere that included both the particle and the absorbing medium. Their approach was further modified by Quinten and Rostalski (1996) who did not use the far field approximation. Bohren and Gilra (1979) also attempted to extend the Mie theory by considering a detector in the far field region that measures the change in the forward-scattered energy (or the extinction energy) due to the presence of a spherical particle. In all these versions of the Mie scattering generalization, the extinction is not a well-defined quantity due to the integration over a large sphere concentric to the particle used in

calculation of extinction. As a result the extinction is a function of the radius of an integrating sphere considered.

In this chapter we calculate the extinction and other scattering quantities of interest by integration over the surface of the spherical particle itself. This approach, similar to that proposed by Lebedev et al. (1999), Sudiarta and Chýlek (2001a) and Fu and Sun (2001), removes the ambiguity in the definition of the extinction and provides methods useful for practical applications.

4.1 Mie Formalism

Let us consider that a plane wave propagating in an absorbing host medium is incident on a spherical particle (radius a) in a direction of a positive z axis with electric and magnetic field vectors $\mathbf{E}_i$ and $\mathbf{H}_i$. The fields inside a sphere is denoted by $\mathbf{E}_1$ and $\mathbf{H}_1$. The scattered fields are $\mathbf{E}_{sca}$ and $\mathbf{H}_{sca}$. The fields outside the sphere are the sum of the scattered and the incident fields:

$$\mathbf{E}_2 = \mathbf{E}_i + \mathbf{E}_{sca}, \mathbf{H}_2 = \mathbf{H}_i + \mathbf{H}_{sca} \tag{4.1}$$

The incident and the scattered fields are expanded in vector spherical harmonics in the forms

$$\mathbf{E}_i = \sum_{n=1}^{\infty} E_n (\mathbf{M}_{o1n}^{(1)} - i\mathbf{N}_{e1n}^{(1)}), \qquad \mathbf{H}_i = \frac{-k_0}{\omega\mu} \sum_{n=1}^{\infty} E_n (\mathbf{M}_{e1n}^{(1)} + i\mathbf{N}_{o1n}^{(1)}), \tag{4.2}$$

$$\mathbf{E}_{sca} = \sum_{n=1}^{\infty} E_n (ia_n \mathbf{N}_{e1n}^{(3)} - b_n \mathbf{M}_{o1n}^{(3)}), \mathbf{H}_{sca} = \frac{k_0}{\omega\mu} \sum_{n=1}^{\infty} E_n (ib_n \mathbf{N}_{o1n}^{(3)} + a_n \mathbf{M}_{e1n}^{(3)}), \tag{4.3}$$

and the inner fields are

$$\mathbf{E}_1 = \sum_{n=1}^{\infty} E_n (c_n \mathbf{M}_{o1n}^{(1)} - id_n \mathbf{N}_{e1n}^{(1)}), \quad \mathbf{H}_1 = \frac{-k_1}{\omega\mu} \sum_{n=1}^{\infty} E_n (d_n \mathbf{M}_{e1n}^{(1)} + ic_n \mathbf{N}_{o1n}^{(1)}), \tag{4.4}$$

where $E_n = i^n (2n+1) E_0 / n(n+1)$, a_n, b_n, c_n and d_n are the scattering coefficients, ω is the angular frequency, $k_0 = 2\pi m_{med}/\lambda$ and $k_1 = 2\pi m_{sph}/\lambda$, m_{med} and m_{sph} are the refractive indices of the host medium and the sphere, λ is the wavelength in vacuum, $\mathbf{M}$ and $\mathbf{N}$ are the vector spherical harmonic functions, which are given by

$$\mathbf{M}_{o1n} = \cos\phi\pi_n(\cos\theta)z_n(\rho)\hat{\mathbf{e}}_\theta - \sin\phi\tau_n(\cos\theta)z_n(\rho)\hat{\mathbf{e}}_\phi,$$

$$\mathbf{M}_{e1n} = -\sin\phi\pi_n(\cos\theta)z_n(\rho)\hat{\mathbf{e}}_\theta - \cos\phi\tau_n(\cos\theta)z_n(\rho)\hat{\mathbf{e}}_\phi,$$

$$\mathbf{N}_{o1n} = n(n+1)\sin\phi\sin\theta\,\pi_n(\cos\theta)\frac{z_n(\rho)}{\rho}\hat{\mathbf{e}}_r + \sin\phi\tau_n(\cos\theta)\frac{1}{\rho}\frac{\partial[\rho z_n(\rho)]}{\partial\rho}\hat{\mathbf{e}}_\theta$$
$$+\cos\phi\pi_n(\cos\theta)\frac{1}{\rho}\frac{\partial[\rho z_n(\rho)]}{\partial\rho}\hat{\mathbf{e}}_\phi,$$

$$\mathbf{N}_{e1n} = n(n+1)\cos\phi\sin\theta\,\pi_n(\cos\theta)\frac{z_n(\rho)}{\rho}\hat{\mathbf{e}}_r + \cos\phi\tau_n(\cos\theta)\frac{1}{\rho}\frac{\partial[\rho z_n(\rho)]}{\partial\rho}\hat{\mathbf{e}}_\theta$$
$$-\sin\phi\pi_n(\cos\theta)\frac{1}{\rho}\frac{\partial[\rho z_n(\rho)]}{\partial\rho}\hat{\mathbf{e}}_\phi, \tag{4.5}$$

where $\rho = kr$, $z_n(\rho) = j_n(\rho)$ for superscript (1) of $\mathbf{M}$ and $\mathbf{N}$, and $z_n(\rho) = h_n(\rho)$ for superscript (3), $\pi_n(\cos(\theta)) = P_n^1(\cos(\theta))/\sin(\theta)$, $\tau_n(\cos(\theta)) = \mathrm{d}P_n^1(\cos(\theta))/\mathrm{d}\theta$, P_n^1 is the associated Legendre function of first kind of degree n and order 1.

The expansion coefficients a_n, b_n, c_n and d_n are obtained by matching the boundary conditions on the surface of a spherical particle. The scattering coefficients for nonmagnetic sphere and medium are found to be (Bohren & Huffman, 1983; Kerker, 1969, van de Hulst, 1957)

$$a_n = \frac{m_r\psi_n(m_r x)\psi_n'(x) - \psi_n(x)\psi_n'(m_r x)}{m_r\psi_n(m_r x)\xi_n'(x) - \xi_n(x)\psi_n'(m_r x)} \tag{4.6}$$

$$b_n = \frac{\psi_n(m_r x)\psi_n'(x) - m_r\psi_n(x)\psi_n'(m_r x)}{\psi_n(m_r x)\xi_n'(x) - m_r\xi_n(x)\psi_n'(m_r x)} \tag{4.7}$$

$$c_n = \frac{im_r}{\psi_n(m_r x)\xi_n'(x) - m_r\xi_n(x)\psi_n'(m_r x)} \tag{4.8}$$

$$d_n = \frac{im_r}{m_r\psi_n(m_r x)\xi_n'(x) - \xi_n(x)\psi_n'(m_r x)} \tag{4.9}$$

where $\psi_n(\rho)$, $\psi_n'(\rho)$, $\xi_n(\rho)$ and $\xi_n'(\rho)$ are the appropriate Riccati-Bessel functions and their derivatives with respect to the argument ρ, m_r is the complex relative refractive index of spherical particle ($m_r = m_{sph}/m_{med}$) and size parameter $x = k_0 a$. The Riccati-Bessel functions used are defined as $\psi_n(\rho) = \rho j_n(\rho)$ and

$\xi_n(\rho) = \rho(j_n(\rho) + iy(\rho))$, where $j_n(\rho)$ and $y_n(\rho)$ are spherical Bessel functions of first and second kind of order n. We note here that we need to evaluate the Riccati-Bessel functions and their derivatives for a complex argument x and $m_r x$.

The above derivation is the original Mie formalism. Formally, the generalized Mie solution is obtained by replacing the real refractive index of medium with a complex refractive index or by replacing the real size parameter x with a complex number. The scattering coefficients remain unchanged. The only modification is that all spherical Bessel functions and size parameters are now complex quantities. In order to determine the scattering properties, the rate energy scattered, absorbed and extinct by sphere are needed. Due to the absorption effect of host medium, the amount of energy incident on sphere is required for cross section calculation. These are discussed in the next section.

4.2. Energy Scattered, Absorbed, Extinct by a Sphere

4.2.1. Scattered Energy

The net rate of the scattered energy is determined by integral of radial component of Poynting vector over surface of a sphere:

$$W_{sca} = \frac{1}{2} Re \iint_S (\mathbf{E}_{\mathbf{sca}} \times \mathbf{H}^*_{sca}) \cdot \hat{\mathbf{r}} dA, \tag{4.10}$$

where $\hat{\mathbf{r}}$ is the unit vector pointing in the direction of outward normal to the surface of sphere, Re means the real part and the asterisk denotes the complex conjugate. After substituting for $\mathbf{E}_{\mathbf{sca}}$ and $\mathbf{H}_{\mathbf{sca}}$, and using the appropriate expansions in vector spherical harmonics, we obtain:

$$W_{sca} = \frac{\pi |E_o|^2}{\mu\omega |k_0|^2} \mathrm{Re}\left\{ k_0^* \sum_{n=1}^{\infty} (2n+1)(-i|a_n|^2 \xi'_n(x)\xi^*{}_n(x) + i|b_n|^2 \xi_n(x)\xi'^*{}_n(x)) \right\} \tag{4.11}$$

where E_0 is an amplitude of an electric field at z = 0.

4.2.2. Absorbed Energy

The energy absorbed by the sphere is evaluated in a similar way:

$$W_{abs} = -\frac{1}{2} Re \iint_S (\mathbf{E} \times \mathbf{H}^*) \cdot \hat{\mathbf{r}} dA \tag{4.12}$$

where $\mathbf{E} = \mathbf{E}_i + \mathbf{E}_{sca}$, $\mathbf{H} = \mathbf{H}_i + \mathbf{H}_{sca}$ and the integral is evaluated over the surface of a sphere. We obtain

$$W_{abs} = \frac{\pi|E_o|^2}{\mu\omega|k_0|^2}\mathrm{Re}\{k_0^*\sum_{n=1}^{\infty}(2n+1)(i\psi_n^*(x)\psi_n'(x) - i\psi_n(x)\psi_n'^*(x) + ib_n\psi_n'^*(x)\xi_n(x) + ib_n^*\psi_n(x)\xi_n'^*(x) + i|a_n|^2\xi_n'(x)\xi^*{}_n(x) - i|b_n|^2\xi_n(x)\xi'^*{}_n(x) - ia_n\psi_n^*(x)\xi_n'(x) - ia_n^*\psi_n'(x)\xi_n^*(x))\} \tag{4.13}$$

Instead of using scattering coefficients a_n and b_n, the absorbed energy can also be expressed in terms of scattering coefficients c_n and d_n. By similar derivation, it can be shown that W_{abs} is of the form

$$W_{abs} = \frac{\pi|E_o|^2}{\mu\omega|k_1|^2}\mathrm{Re}\left\{k_1^*\sum_{n=1}^{\infty}(2n+1)(i|d_n|^2\psi_n^*(m_r x)\psi_n'(m_r x) - i|c_n|^2\psi_n(m_r x)\psi_n'^*(m_r x))\right\} \tag{4.14}$$

Another form of expression of W_{abs} is found by a volume integration. Using the divergence theorem, the surface integration in Eq. (4.12) can be converted to a volume integration in a form

$$W_{abs} = -\frac{1}{2}Re\iiint_V \nabla\cdot(\mathbf{E}_1\times\mathbf{H}_1^*)dV \tag{4.15}$$

where the volume integration is over the volume of particle. Maxwell's equations in frequency domain (by substituting time dependence $\exp(-i\omega t)$) are given by $\nabla\times\mathbf{E} = i\omega\mu\mathbf{H}$, and $\nabla\times\mathbf{H} = -i\omega\varepsilon\mathbf{E}$. Using a vector identity and with substitutions of the Maxwell's equations, it can be shown that $\nabla\cdot(\mathbf{E}\times\mathbf{H}^*) = -i\omega\varepsilon^*|\mathbf{E}|^2 + i\omega\mu|\mathbf{H}|^2$. After substituting $\varepsilon = \varepsilon_0\varepsilon_r = \varepsilon_0(\varepsilon_R + i\varepsilon_I)$, we have

$$W_{abs} = \frac{1}{2}\varepsilon_0\varepsilon_I\omega\iiint_V|\mathbf{E}_1|^2 dV \tag{4.16}$$

After substituting the expansions of internal fields Eq. (4.4) and after considerable manipulations, it can be shown that

$$W_{abs} = \pi\varepsilon_0\omega|E_o|^2\varepsilon_I\sum_{n=1}^{\infty}(2n+1)|c_n|^2\int_0^a|j_n(k_1r)|^2r^2dr + |d_n|^2\int_0^a[(n+1)|j_{n-1}(k_1r)|^2 + n|j_{n+1}(k_1r)|^2]r^2dr \quad (4.17)$$

4.2.3. Extinction

Extinction is defined as energy removed by particle due to absorption and scattering i.e. the sum of the scattered and absorbed energy $W_{sca}+W_{abs}$ (Chýlek, 1977; Bohren and Huffman, 1983). In this definition, the energy absorbed by the host medium is not included. We have used the integrating sphere given by the surface of the particle to eliminate the energy absorbed by the host medium. This is convenient when we are interested in the extinction caused by the particle itself; not by the medium. The host medium causes the field to decay as it travels through the medium. Consequently the host medium affects the amount of energy incident upon the particle. This effect is accounted for in the calculation of an average intensity incident upon the particle.

Adding Eq. (4.11) and Eq. (4.13) we obtain

$$W_{ext} = \frac{\pi|E_o|^2}{\mu\omega|k_0|^2}Re\{k_0^*\sum_{n=1}^{\infty}(2n+1)(i\psi_n^*(x)\psi_n'(x) - i\psi_n(x)\psi_n'^*(x) + ib_n\psi_n'^*(x)\xi_n(x) + ib_n^*\psi_n(x)\xi_n'^*(x) - ia_n\psi_n^*(x)\xi_n'(x) - ia_n^*\psi_n'(x)\xi_n^*(x))\} \quad (4.18)$$

These results are equivalent to the expressions given by Lebedev et al. (1999) and by Quinten and Rostalski (1996) when the size of integrating sphere is equal to the size of particle. For non-absorbing medium, the scattering, absorption and extinction reduce to the standard Mie theory form (Bohren & Huffman, 1983; Kerker, 1969; van de Hulst, 1957).

Using a similar derivation as for W_{abs}, but now we use $W_{ext}=W_{sca}+W_{abs}$ and Eqs. (4.1), (4.10) and (4.12), after some manipulations it can be shown that

$$W_{ext} = \frac{1}{2}\varepsilon_0\omega[\mathrm{Im}\{\iiint_V(\varepsilon_r-\varepsilon_h^*)\mathbf{E}_1\cdot\mathbf{E}_i^*dV\} - \iiint_V\varepsilon_{hI}|\mathbf{E}_i|^2dV], \quad (4.19)$$

where $\mathbf{E}_i$ is the incident field, $\varepsilon_h=\varepsilon_{hR}+\varepsilon_{hI}i$ is the complex dielectric constant of host medium. After substituting the expansions of vector spherical harmonics and some manipulations, it can be shown that

$$W_{ext} = \pi\varepsilon_0\omega|E_o|^2[\mathrm{Im}\{(\varepsilon_r - \varepsilon_h^*)\sum_{n=1}^{\infty}(2n+1)c_n\int_0^a|j_n(k_1r)|^2 r^2dr + d_n\int_0^a[(n+1)|j_{n-1}(k_1r)|^2 + n|j_{n+1}(k_1r)|^2]r^2dr\} - \tfrac{2}{3}\pi a^3\varepsilon_{hI}] \quad (4.20)$$

4.3. Incident Intensity

As a consequence of an absorbing medium the field incident on the sphere is different at different locations on the sphere. Therefore, we need to calculate the total energy flux incident upon the particle. This can be done by calculating the net energy crossing the illuminated part of the sphere. We define an average incident intensity as an average energy flux crossing the cross-sectional area of a sphere, $I = W/\pi a^2$. Thus average incident intensity is given by

$$I = \frac{1}{2\pi a^2} Re\int_{half\ sphere}(\mathbf{E}_i \times \mathbf{H}_i^*)\cdot\hat{\mathbf{r}}dA \quad (4.21)$$

The integration is over an illuminated part of a sphere. We obtain

$$I = \frac{|E_o|^2}{\mu\omega}\mathrm{Re}\{k_0\}\left(\frac{\exp(2ak_{0,I})}{2ak_{0,I}} + \frac{1-\exp(2ak_{0,I})}{(2ak_{0,I})^2}\right) \quad (4.22)$$

where $k_{0,I}$ is the imaginary part of wave number k_0 in host medium. This modification of an average intensity incident upon a particle (Eq. (4.22)) was first derived by Mundy et al. (1974).

The cross sections are now obtained as $\sigma = W/I$ and efficiencies are given by $Q = W/I\pi a^2$. Taking the limit of Eq. (4.22) for a non-absorbing medium ($k_{0,I} = 0$), the Eq. (4.22) reduces to the usual expression of intensity,

$$I = \frac{1}{2}\varepsilon c|E_o|^2 \quad (4.23)$$

4.4. Numerical Results

A computer program for computing the Mie cross sections, for example as found in Bohren and Huffman (1983), can be modified following the previous derivation. A Mathematica notebook written for this purpose is provided in Sudiarta (2003a).

The effect of an absorbing medium on the extinction efficiency is shown in Fig. 4.1 (the particle itself is not absorbing). The interference and the ripple structures (Chýlek & Zhan, 1989; Chýlek, 1976) are significantly reduced with an increasing absorption of a medium. As the radius of a sphere increase, the extinction efficiency approaches an asymptotic limit of 1. This is in contrast to the non-absorbing medium case where the extinction approaches a value of 2 (extinction paradox) (Bohren and Huffman, 1983; can de Hulst, 1957). For a large spherical particle embedded in an absorbing medium, the incident radiation is absorbed by a medium before it can reach the edges of a sphere. Thus, in an asymptotic limit of a radius approaching infinity, there is no diffraction contribution to the extinction efficiency.

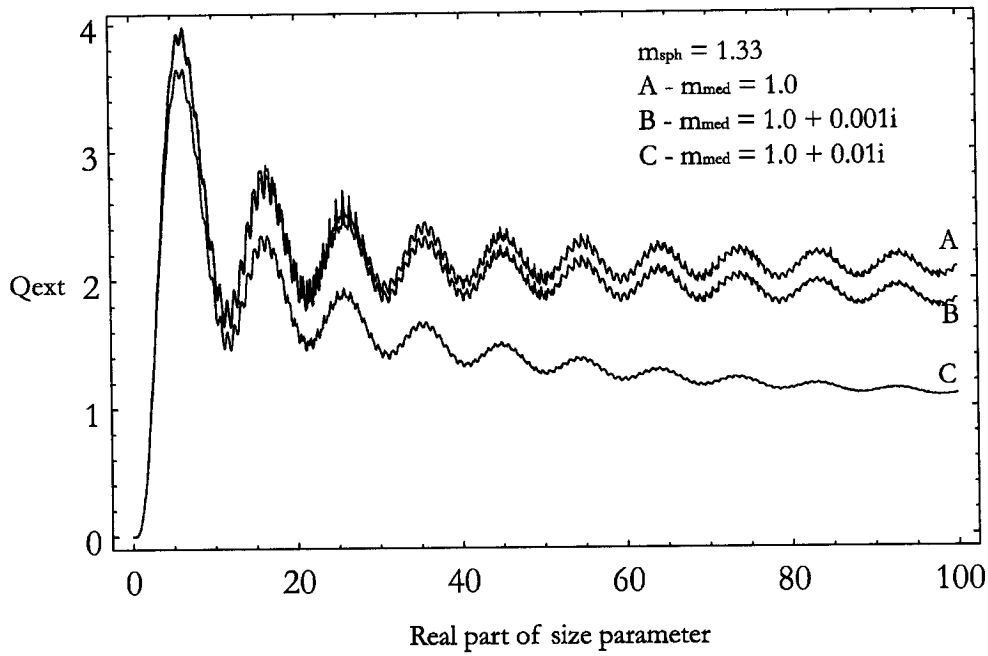

Figure 4.1: The extinction efficiency (Q_{ext}) of a non-absorbing sphere, with a refractive index m_{sphere} = 1.33, placed in a medium of a given refractive index (1; 1+0.01i; 1 +0.001i) as a function of real part of size parameters x. The size parameter $x = 2\pi a m_{med} / \lambda$, where a is the radius of the sphere and λ is the wavelength of considered radiation in vacuum.

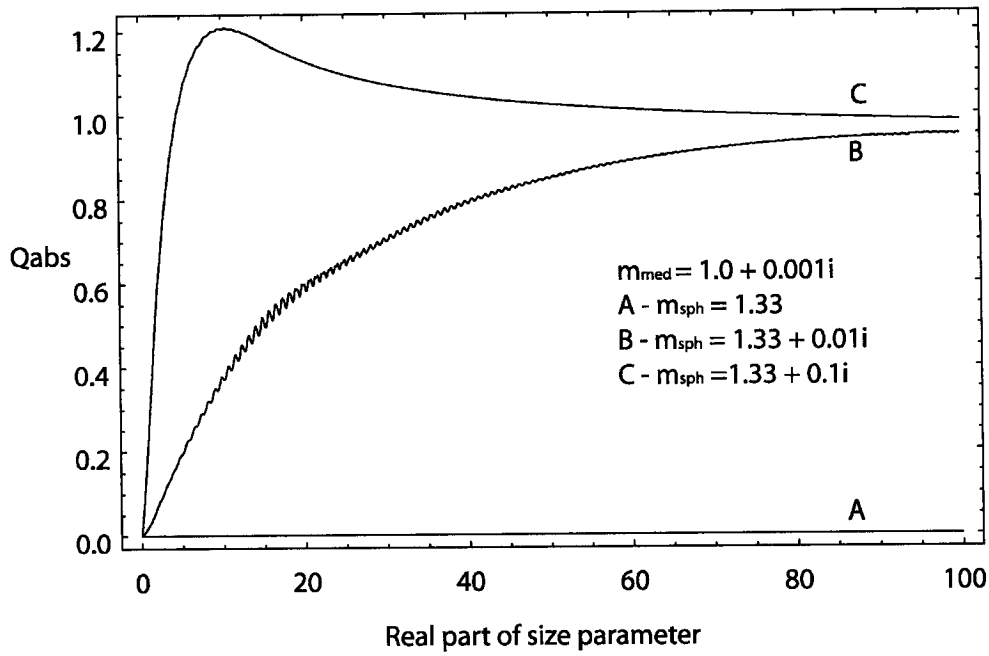

Figure 4.2: The absorption efficiency (Q_{abs}) for a sphere, with a refractive index ($m_{sph} = 1.33\ ,\ 1.33 + 0.01i\ ,\ 1.33 + 0.1i$), placed in a medium of a refractive index ($m_{med} = 1.0 + 0.001i$) as a function of real part of size parameters x.

For the case of a non-absorbing sphere placed in an absorbing medium, the relative refractive index of sphere is complex. Therefore, one can argue that a particle embedded in an absorbing medium should absorb the radiation even if a particle by itself is non-absorbing. This turns out, however, to be incorrect. The numerical calculations show (Fig. 4.2) that the absorption is zero when the refractive index of a particle is real. It is noted in Fig. 4.2 that for a large absorbing sphere the absorption efficiency approaches a certain numerical value.

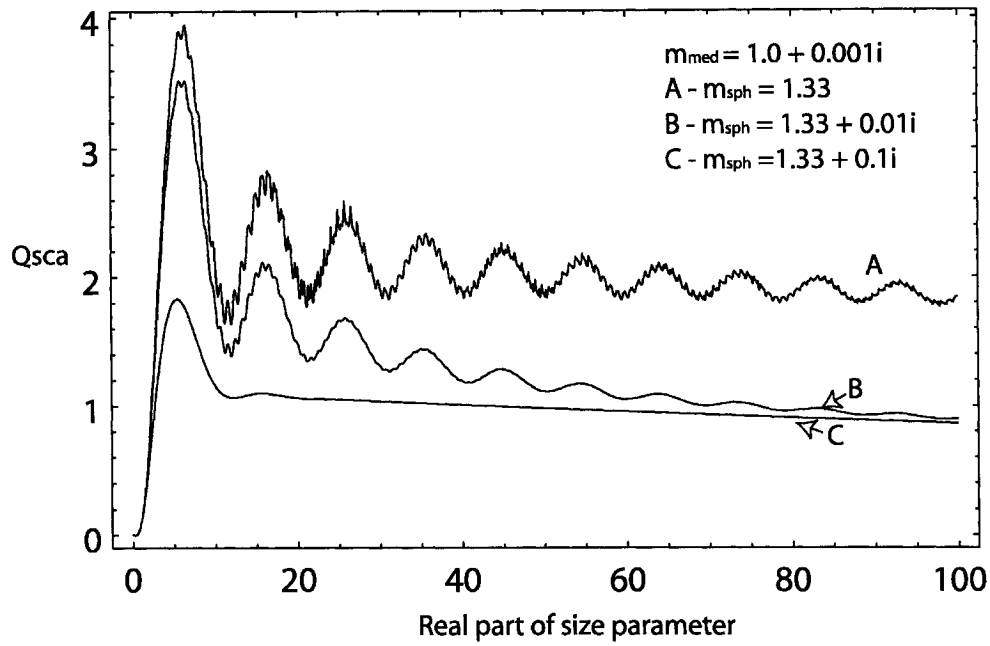

Figure 4.3: The same as Fig. 4.2, except it is for the scattering efficiency (Q_{sca}).

The scattering efficiency for a sphere in absorbing medium is shown in Fig. 4.3. Similar to absorption efficiency, the scattering efficiency also approaches a definite value as the size parameter increases.

From Fig. 4.1 it is shown that the effect of absorbing host medium is significant for a large particle or for very absorbing medium. For atmospheric applications, because of small size particle and small absorption of the atmosphere, the effect is small and it can be neglected.

4.5. Asymptotic Limit of Mie Scattering Efficiency

For non-absorbing host medium, the Mie scattering efficiency (Q_{sca}) is given by

$$Q_{sca}(x,m) = \frac{2}{x^2}\sum_{n=1}^{\infty}(2n+1)(|a_n|^2 + |b_n|^2). \tag{4.24}$$

For the case of a spherical particle embedded in a non-absorbing medium, Herman (1962) suggested the asymptotic limit of the scattering efficiency to be

$$\lim_{x\to\infty} Q_{sca} = 1 + R(0^o) \tag{4.25}$$

where $R(0^o) = \left|(m_r - 1)/(m_r + 1)\right|^2$ is a reflectance of a plane surface at normal incidence.

This limit seems to be intuitively plausible if we consider that the sphere becomes a planar surface at an infinitely large radius. Thus the Q_{sca} is expected to be equal to one (the diffraction part) plus the reflection of a planar surface. The same limiting value was deduced by Chylek (1973, 1975) by considering an asymptotic limit of the Eq. (4.24). Acquista et al. (1980) argued that Chylek's derivation may not be correct, since some terms were neglected without a proper justification.

van de Hulst (1957) and later Deirmendjian (1969) suggested an alternative expression for an asymptotic form of a scattering efficiency of a large absorbing sphere in the form

$$\lim_{x \to \infty} Q_{sca} = 1 + \int_0^{\pi/2} (| r_1 |^2 + | r_2 |^2) \cos(\theta) \sin(\theta) \, d\theta \tag{4.26}$$

where r_1 and r_2 are the Fresnel reflection coefficients (Jackson, 1999; Griffiths, 1981) for radiation incident at the angle θ. The first term in Eq. (4.26) represents the diffraction and the second term the radiation reflected at the front surface of a sphere. Bohren and Herman (1979) provided numerical calculations for a sphere of the size parameter up to the order of 10^4 to show that the numerical results, using the Mie scattering efficiency Eq. (4.24), seem to approach the limit given by Eq. (4.26). Calculation of the Q_{sca} for size parameter up to the order of 10^5 supports this conclusion (Fig. 4.4). To verify this numerical result, the absorption efficiency is calculated using Eq. (4.13) and the numerical results are shown in Fig. 4.5. From the large size limit of absorption efficiency, it can be shown that the scattering efficiency can be obtained from the relation

$$\lim_{x \to \infty} Q_{sca} = 2 - \lim_{x \to \infty} Q_{abs} \tag{4.27}$$

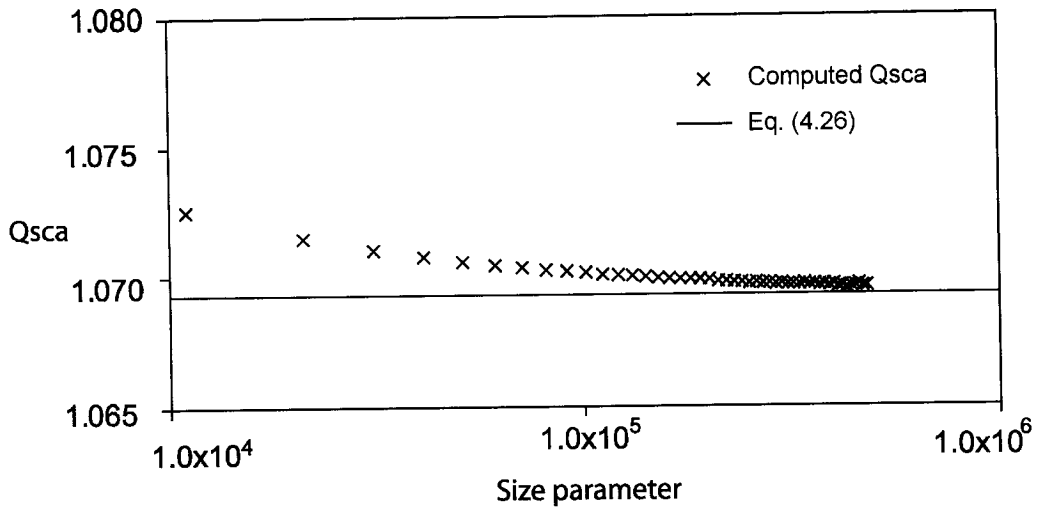

Figure 4.4: Scattering efficiency of a sphere with index of refraction 1.33 +0.1i embedded in a non-absorbing host medium (m_{med} =1). The crosses show computed Q_{sca}. The limiting value, given by Eq. (4.26), is 1.069299.

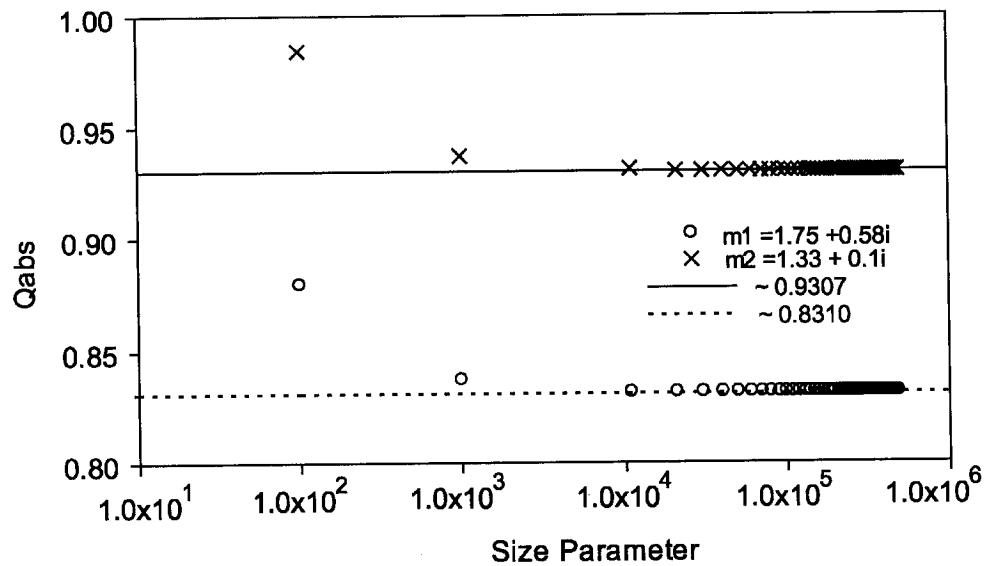

Figure 4.5: Absorption efficiency of a spherical particle with the refractive index m_1 = 1.33 +0.1i and m_2 = 1.75 + 0.58i embedded in a non-absorbing host medium (m_{med} =1.0). The crosses and circles show computed Q_{abs} for refractive indices m_1 and m2 respectively.

Table 4.1: Calculated large radius limit of Q_{abs} and the right hand side of Eq. (4.26).

m_r	Q_{abs}	$Q_{sca} = 2 - Q_{abs}$	Q_{sca} from Eq. (4.26).
$1.33 + 0.1i$	0.9307	1.0693	1.069299
$1.75 + 0.58i$	0.8310	1.1690	1.169033
$1.55 + 0.155i$	0.8964	1.1036	1.103645
$1.29 + 0.0472i$	0.9396	1.0604	1.060395

Comparison of results obtained from Eqs. (4.25) and (4.26) is provided in Table 4.1. Using previous results, the scattering efficiency of a spherical particle embedded in an absorbing medium for the real part of the size parameter up to the order of 10^4 is shown in Fig. 4.6. It is apparent that the scattering efficiency approaches the value given by the reflection at a flat surface at perpendicular incidence, suggesting that we have

$$\lim_{x \to \infty} Q_{sca} = R(0^o) \tag{4.28}$$

Comparing this expression with those for a particle in a non-absorbing medium, we see that: (a) the diffraction term (equal to one in the case of non-absorbing medium) is not present, and (b) the term representing the reflection by a sphere in Eq. (4.26) is replaced by a reflection by a flat surface at perpendicular incidence.

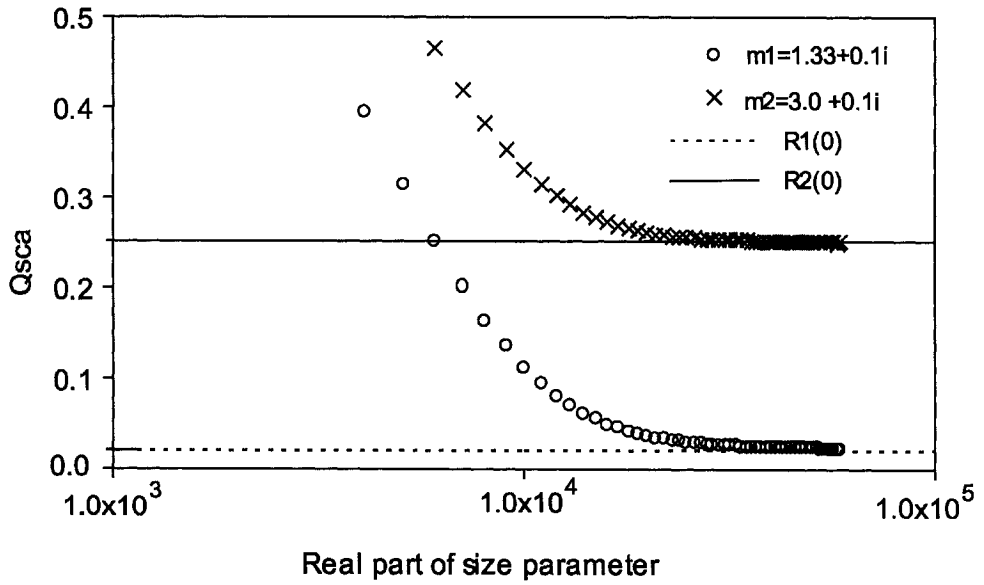

Figure 4.6: Q_{sca} for a sphere with refractive index m_1=1.33 + 0.1i and m_2 = 3.0 +0.1i, embedded in an absorbing medium with refractive index $m_{med} = 1+10^{-4}i$. $R_1(0)$ = 0.021861 and $R_2(0)$ = 0.250468 is the reflectance of a planar interface at normal incidence, for refractive indices m_1 and m_2 , respectively.

4.6 A Coated Sphere in an Absorbing Medium

I give here a brief explanation on how the solution for scattering by a coated sphere is reformulated. The solution for a light scattering by a coated sphere in a non-absorbing medium was first obtained by Aden and Kerker (1951). Following previous treatment for generalizing the Mie theory for absorbing host medium, we can reformulate straightforwardly the solution for a coated sphere. It was mentioned previously that one crucial modification of the Mie theory is the replacement of the host medium with complex quantities. The cross sections for a coated sphere can follow the previous derivation.

Following the derivation given in Bohren and Huffman (1983), the electric and magnetic fields are expanded in vector spherical harmonics, and the coefficients of expansions are obtained by satisfying the boundary conditions at the interface of core and coating, and interface of host medium and coating. The scattering coefficients are given by

$$a_n = \frac{\psi_n(x_2)[\psi_n'(m_2x_2) - A_n\xi_n'(m_2x_2)] - m_2\psi_n'(x_2)[\psi_n(m_2x_2) - A_n\xi_n(m_2x_2)]}{\xi_n(x_2)[\psi_n'(m_2x_2) - A_n\xi_n'(m_2x_2)] - m_2\xi_n'(x_2)[\psi_n(m_2x_2) - A_n\xi_n(m_2x_2)]},$$

$$b_n = \frac{m_2\psi_n(x_2)[\psi_n'(m_2x_2) - B_n\xi_n'(m_2x_2)] - \psi_n'(x_2)[\psi_n(m_2x_2) - B_n\xi_n(m_2x_2)]}{m_2\xi_n(x_2)[\psi_n'(m_2x_2) - B_n\xi_n'(m_2x_2)] - \xi_n'(x_2)[\psi_n(m_2x_2) - B_n\xi_n(m_2x_2)]}, \quad (4.29)$$

where

$$A_n = \frac{m_2\psi_n'(m_1x_1)\psi_n(m_2x_1) - m_1\psi_n(m_1x_1)\psi_n'(m_2x_1)}{m_2\psi_n'(m_1x_1)\xi_n(m_2x_1) - m_1\psi_n(m_1x_1)\xi_n'(m_2x_1)},$$

$$B_n = \frac{m_2\psi_n(m_1x_1)\psi_n'(m_2x_1) - m_1\psi_n'(m_1x_1)\psi_n(m_2x_1)}{m_2\psi_n(m_1x_1)\xi_n'(m_2x_1) - m_1\psi_n'(m_1x_1)\xi_n(m_2x_1)}, \quad (4.30)$$

where m_1 and m_2 are the refractive indices of core and coating relative to the host medium, $x_1 = k_0a_1$ and $x_2 = k_0a_2$; a_1 and a_2 are the radius of core and coating, $k_0 = 2\pi m_{med}/\lambda$, where λ is the wavelength in vacuum.

The expressions for cross sections of a coated sphere turn out to be the same as the expression for a homogenous sphere except size parameter x is replaced by the coating size parameter x_2. The net rate scattered, absorbed and extinct energy are rewritten here as

$$W_{sca} = \frac{\pi|E_o|^2}{\mu\omega|k_0|^2}\mathrm{Re}\left\{k_0^*\sum_{n=1}^{\infty}(2n+1)[-i|a_n|^2\xi_n'(x_2)\xi_n^*(x_2)+i|b_n|^2\xi_n(x_2)\xi_n'^*(x_2)]\right\} \quad (4.31)$$

$$\begin{aligned}W_{abs} = \frac{\pi|E_o|^2}{\mu\omega|k_0|^2}\mathrm{Re}\{k_0^*\sum_{n=1}^{\infty}\ & (2n+1)[i\psi_n^*(x_2)\psi_n'(x_2)-i\psi_n(x_2)\psi_n'^*(x_2)\\ & +ib_n\psi_n'^*(x_2)\xi_n(x_2)+ib_n^*\psi_n(x_2)\xi_n'^*(x_2)+i|a_n|^2\xi_n'(x_2)\xi_n^*(x_2)\\ & -i|b_n|^2\xi_n(x_2)\xi'^*_n(x_2)-ia_n\psi_n^*(x_2)\xi_n'(x_2)-ia_n^*\psi_n'(x_2)\xi_n^*(x_2)]\}\end{aligned} \quad (4.32)$$

$$\begin{aligned}W_{ext} = \frac{\pi|E_o|^2}{\mu\omega|k_0|^2}Re\{k_0^*\sum_{n=1}^{\infty}\ & (2n+1)[i\psi_n^*(x_2)\psi_n'(x_2)-i\psi_n(x_2)\psi_n'^*(x_2)\\ & +ib_n\psi_n'^*(x_2)\xi_n(x_2)+ib_n^*\psi_n(x_2)\xi_n'^*(x_2)\\ & -ia_n\psi_n^*(x_2)\xi_n'(x_2)-ia_n^*\psi_n'(x_2)\xi_n^*(x_2)]\}\end{aligned}$$

4.7 Summary

A new formulation of Mie scattering in an absorbing medium and numerical results are presented in this chapter. Numerical results have shown that for an absorbing host medium the extinction efficiency approaches one as the size parameter of sphere is large. This is in contrast to the extinction efficiency for non-absorbing host medium where the extinction efficiency approaches two. The reason for this difference is due to attenuation of the incident field as it propagates in the absorbing host medium. This attenuation leads to a decrease in incident field reaching the edge of sphere and consequently a decrease in diffraction effect. The scattering efficiency of sphere in absorbing medium approaches the reflection of a plane surface as the size parameter increases. On the other hand, for non-absorbing case, the scattering efficiency approaches a geometrical reflection by a sphere.

Chapter 5

Effective Medium Approximations

Single scattering properties of heterogeneous particles are needed for radiative transfer calculations in atmospheric science, oceanography and remote sensing. The problem of scattering by a heterogeneous particle is a very complicated problem. Therefore it is desirable to have an approximate method that approximate the scattering properties of heterogeneous particles. Various approximate methods, known as effective medium approximations (EMAs), for composite linear media are discussed in this chapter.

5.1 Introduction

To simplify discussion, let us consider a composite material comprised of inclusion particles with dielectric constant ε_i and a host medium with dielectric constant ε_h. Because inclusion particles are randomly positioned and oriented, it is therefore possible to represent this composite media with a homogenous effective medium with dielectric constant ε_{eff}, provided that the sizes of inclusions are less than the wavelength in the host medium. Here, we use the subscripts *eff*, i and h for indicating the effective, the inclusion, and the host dielectric constants. Let f be the fraction of volume occupied by

the inclusions.

The effective medium in a quasi-static field is determined from a requirement that the average of electric displacement of the heterogeneous medium is the same as that of the homogenous effective medium. The electric displacement $\mathbf{D}$ and the electric field $\mathbf{E}$ for linear media is related by Eq. (2.5), rewritten here,

$$\mathbf{D}(\mathbf{r}) = \varepsilon(\mathbf{r})\varepsilon_0\mathbf{E}(\mathbf{r}) \tag{5.1}$$

where $\varepsilon(\mathbf{r})$ is the dielectric constant (the subscript r of the dielectric constant $\varepsilon(\mathbf{r})$ is dropped here to simplify the notation.), which generally depends on position $\mathbf{r}$. Therefore, an effective dielectric constant ε_{eff} of a composite medium in a quasi-static approximation is defined by

$$< \mathbf{D}(\mathbf{r}) >=< \varepsilon(\mathbf{r})\varepsilon_0\mathbf{E}(\mathbf{r}) >= \varepsilon_{eff}\varepsilon_0 < \mathbf{E}(\mathbf{r}) > \tag{5.2}$$

where the bracket <> represents a spatial averaging.

For a composite of two media, the effective dielectric constant can be defined as

$$\varepsilon_{eff} = \frac{\int_V \mathbf{D}dV}{\varepsilon_0 \int_V \mathbf{E}dV} = \frac{f\varepsilon_i < \mathbf{E}_i > + (1-f)\varepsilon_h < \mathbf{E}_h >}{f < \mathbf{E}_i > + (1-f) < \mathbf{E}_h >} \tag{5.3}$$

where $\mathbf{E}_i$ and $\mathbf{E}_h$ are the electric fields inside the inclusion and host medium, respectively.

Depending on how $< \mathbf{E}_i >$ and $< \mathbf{E}_h >$ are approximated, and depending on the assumptions of the sizes of inclusions, the shapes of the inclusions, and the topology of a mixture, an approximate expression (also known as a mixing rule) for effective dielectric constant can be obtained (Chylek et al., 2000). There are many mixing rules that have been used in the past. The well-known mixing rules, often used in atmospheric applications, are the followings:

(a) The Maxwell-Garnett (MG) mixing rule,

$$\frac{\varepsilon_{eff} - \varepsilon_h}{\varepsilon_{eff} + 2\varepsilon_h} = f\frac{\varepsilon_i - \varepsilon_h}{\varepsilon_i + 2\varepsilon_h}; \tag{5.4}$$

(b) By interchanging the role of host and inclusion, $\varepsilon_i \leftrightarrow \varepsilon_h$ and $f \leftrightarrow (1-f)$ in the Maxwell-Garnet mixing rule, we obtain the inverted Maxwell-Garnet (IMG) mixing rule,

$$\frac{\varepsilon_{eff}-\varepsilon_i}{\varepsilon_{eff}+2\varepsilon_i}=(1-f)\frac{\varepsilon_h-\varepsilon_i}{\varepsilon_h+2\varepsilon_i}; \tag{5.5}$$

(c) The Bruggeman (BR) mixing rule is

$$f\frac{\varepsilon_i-\varepsilon_{eff}}{\varepsilon_i+2\varepsilon_{eff}}+(1-f)\frac{\varepsilon_h-\varepsilon_{eff}}{\varepsilon_h+2\varepsilon_{eff}}=0\text{; and} \tag{5.6}$$

(d) Some other simple mixing rules can be put in the form of

$$\varepsilon_{eff}=\left[f\varepsilon_i^{\alpha}+(1-f)\varepsilon_h^{\alpha}\right]^{1/\alpha}, \tag{5.7}$$

where α is a constant ($-1\le\alpha\le 1$). We have volume average with $\alpha=1$, average of refractive index $\alpha=1/2$ and cube root average $\alpha=1/3$ (Landau and Lifshitz, 1960).

The Maxwell-Garnett and Bruggeman methods are derived on the assumption of spherical inclusions with the size parameters much smaller than the wavelength in the host medium.

5.2 Dynamic Effective Medium Approximations

The previous definition of an effective medium (Eq. (5.2)) is applicable only for a quasi-static fields. For a scattering problem the electromagnetic fields are time-dependent fields. We, therefore, need to redefine the effective medium. In this study three methods are considered for defining an effective medium based on: (a) the total (or extinction) cross section, (b) the energy content, and (c) a multiple scattering approach. In the first method, an effective medium is chosen in such a way that the requirement of the difference in the total cross section between the composite medium and the effective medium vanishes on average (Kirchner et. al, 1998; Busch & Soukoulis, 1995). In the second method, we consider an electromagnetic plane wave propagating in a composite material, and an effective medium is obtained by demanding the same energy content in the composite material as in an homogenous effective medium (Busch & Soukoulis, 1995 and 1996). In the last method, the wave propagation in a random medium is first solved, and the effective medium is then derived from an effective wave number in the medium.

5.2.1 Equivalence of Extinction Cross Section (Aggregate Structure or Bruggeman Type)

A composite material can be classified into two types: an aggregate structure (or Bruggeman type) and a separated-grain structure (or Maxwell-Garnett type) (Chylek, 1988). We first discuss the aggregate structure. Let us consider a composite medium of two materials with dielectric constants ε_1 and ε_2, and volumes V_1 and V_2 as shown in Fig. 5.1a. We define a volume fraction of the materials as $f_1 = V_1/(V_1+V_2)$ and $f_2 = V_2/(V_1+V_2)$. To reformulate EMA, we assume that an aggregate material (e.g. Fig. 5.1a) can be modeled by an aggregate of spheres with radii R_1 and R_2 (e.g. Fig. 5.1b). We assume that the aggregate of material can be replaced by an effective material ε_{eff}. Let us consider a plane wave propagating in the aggregate material. To determine the effective material, we use the requirement that the attenuation (or extinction) due to the aggregate material is the same as the attenuation in the effective material. Let us consider only one of the spheres in the aggregate of spheres (see Fig. 5.1b). This sphere feels the homogeneous effective material as the surrounding medium since we assumed that the effective material can replace the aggregate material. Therefore this sphere can be considered to be embedded in the effective material. This is illustrated in Fig. 5.1c. The attenuation of this sphere can be obtained from the solution of the Mie theory as discussed in chapter 4. In order that the effective material represents the attenuation of the aggregate material properly, the volume-averaged attenuation of all the spheres in the aggregate of spheres model must be the same as the attenuation of the effective material. In other words, the effective material is chosen in such a way that the difference between the extinction cross sections of a sphere embedded in the effective material and a spherical volume of the effective material vanishes on average (Kirchner et. al, 1998; Busch & Soukoulis, 1996).

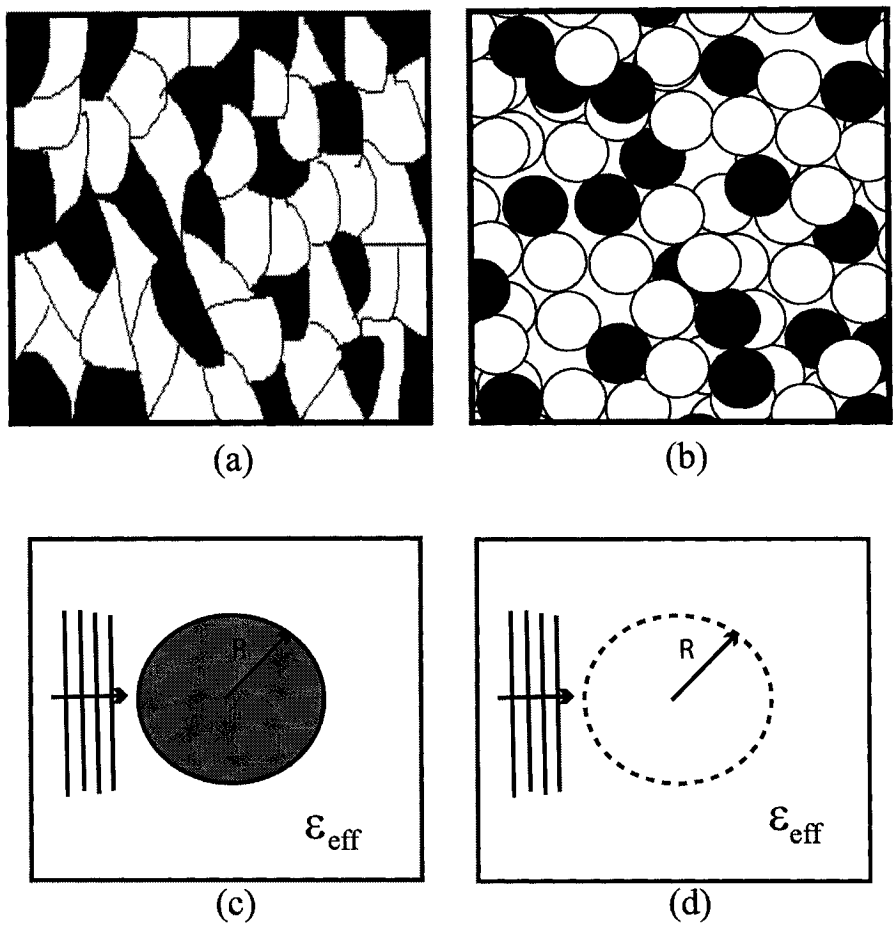

Figure 5.1: (a) An aggregate material, (b) an aggregate of spheres, (c) a plane wave incident on a spherical particle in an effective medium, and (d) a plane wave propagating in an effective medium. A spherical volume of the effective medium is also shown in (d). The requirement for determining the effective medium is that the difference in attenuation between the spherical particle in (c) and the spherical volume of the effective medium in (d) vanishes on average.

Stroud and Pan (1978) stated that the requirement of vanishing total (or extinction) cross section is equivalent to a requirement of vanishing total forward scattering amplitude $S(0)$. This is true for a non-absorbing host medium since from the optical theorem it is known that the total cross-section is proportional to S(0) (Bohren and Huffman,1983). For an absorbing host medium, the total cross-section is no longer proportional to S(0). This is because of the attenuation of the field in the host medium. The effect of the absorbing medium on the scattering by a sphere is discussed in chapter 4. It was shown that the effect of an absorbing host medium becomes important when we have a highly absorbing medium or a large spherical particle. Therefore S(0) cannot be used for formulating the effective medium approximation in such cases.

Alternatively, we can use an equivalent requirement based on the difference in the net rate of energy extinction of a particle volume, instead of the difference in total cross section. This can be done since, by definition, a cross section is directly related to the net rate of energy flow (see chapter 4). In other words, for an effective medium to represent a composite medium, the net rate extinct energy of a particle volume should be the same as the net rate of energy flow into the effective medium with the same volume as the particle. Therefore, the equivalent requirement for an effective medium is of the form

$$< \Delta W >=< W_{\text{ext}} - W_{\text{eff}} >= 0 \tag{5.8}$$

where W_{ext} and W_{eff} are the net rate of energy extinction due to a spherical particle and the net rate of energy extinction due to the same spherical volume of an effective medium.

For an absorbing aggregate material, the corresponding effective medium is also an absorbing one. Therefore we need also to include the absorption of the effective medium in the formulation of EMA. For an absorbing medium the net rate extinct energy is given by Eq. (4.18) and it is rewritten here,

$$\begin{aligned} W_{ext} = \frac{\pi|E_o|^2}{\mu\omega|k|^2} Re\{k^* \sum_{n=1}^{\infty} \; & (2n+1)(i\psi_n^*(x)\psi_n'(x) - i\psi_n(x)\psi_n'^*(x) \\ & + ib_n\psi_n'^*(x)\xi_n(x) + ib_n^*\psi_n(x)\xi_n'^*(x) \\ & - ia_n\psi_n^*(x)\xi_n'(x) - ia_n^*\psi_n'(x)\xi_n^*(x))\} \end{aligned} \tag{5.9}$$

The net rate of energy extinction due to a spherical volume of an effective medium is obtained by substituting $a_n = b_n = 0$ into Eq. (5.9) since we know the fact that there is no particle present.

$$W_{eff} = \frac{\pi |E_o|^2}{\mu\omega |k|^2} \mathrm{Re}\{k^* \sum_{n=1}^{\infty} (2n+1)(i\psi_n^*(x)\psi_n'(x) - i\psi_n(x)\psi_n'^*(x)\} \tag{5.10}$$

The difference in the net rate of energy extinction for a spherical particle, after a manipulation using the identity $\mathrm{Re}\{g^*\} = \mathrm{Re}\{g\}$, is given by

$$\begin{aligned} W_{ext} - W_{eff} = \frac{\pi |E_o|^2}{\mu\omega |k|^2} Re\{\sum_{n=1}^{\infty} (2n+1)[ia_n(k\ \psi_n'^*(x)\xi_n(x) - k^*\psi_n^*(x)\xi_n'(x)) \\ + ib_n(k^*\psi_n'^*(x)\xi_n(x) - k\psi_n(x)^*\xi_n'(x))]\} \end{aligned} \tag{5.11}$$

For an aggregate of spheres, the requirement of EMA (Eq. (5.8)) can be expressed by

$$\sum_j n_j (W_{ext,j} - W_{eff,j}) = 0 \tag{5.12}$$

where $n_j = f_j / (\frac{4}{3}\pi R_j^3)$ is the number concentration of the jth sphere. After substitution of Eq. (5.11) into Eq. (5.12) and simplification, we have

$$\begin{aligned} \mathrm{Im}\{\sum_j n_j \sum_{n=1}^{\infty} (2n+1)[a_{n,j}(k\ \psi_n'^*(x)\xi_n(x) - k^*\psi_n^*(x)\xi_n'(x)) \\ + b_{n,j}(k^*\psi_n'^*(x)\xi_n(x) - k\psi_n(x)^*\xi_n'(x))]\} = 0 \end{aligned} \tag{5.13}$$

We assume here that the quantity inside $\mathrm{Im}\{\}$ is also zero, then we have

$$\begin{aligned} \sum_j n_j \sum_{n=1}^{\infty} (2n+1)[a_{n,j}(k\ \psi_n'^*(x)\xi_n(x) - k^*\psi_n^*(x)\xi_n'(x)) \\ + b_{n,j}(k^*\psi_n'^*(x)\xi_n(x) - k\psi_n(x)^*\xi_n'(x))] = 0 \end{aligned} \tag{5.14}$$

For a non-absorbing medium, it can be shown using Wronskian relations that Eq. (5.14) reduces to the original self-consistent requirement as stated by Stroud and Pan (1978), that is

$$\sum_j n_j \sum_{n=1}^{\infty} (2n+1)[a_{n,j} + b_{n,j}] = 0 \tag{5.15}$$

The mixing rule resulted from Eq. (5.14) with a homogenous sphere model will be called Extended Bruggemann (EBR) mixing rule, whereas the mixing rule Eq. (5.15) will

be called Uncorrected-EBR (UEBR).

For small particle grains ($x << 1$), we need to keep only the first term of the expansions

$$\sum_j f_j[a_{1,j}(k\ \psi_1'^*(x)\xi_1(x) - k^*\psi_1^*(x)\xi_1'(x)) + b_{1,j}(k^*\psi_1'^*(x)\xi_1(x) - k\psi_1(x)^*\xi_1'(x))] = 0 \tag{5.16}$$

The Riccati-Bessel functions and scattering coefficients are approximated by

$$\psi_1(x) \approx \frac{x^2}{3} - \frac{x^4}{30} + O(x^6),\ \psi_1'(x) \approx \frac{2x}{3} - \frac{2x^3}{15} + O(x^4),$$

$$\xi_1(x) \approx -\frac{i}{x} - \frac{ix}{2} + \frac{x^2}{3} + O(x^3),\ \xi_1'(x) \approx \frac{i}{x^2} - \frac{i}{2} + \frac{2x}{3} + O(x^2),$$

$$a_{1,j} \approx -\frac{2ix^3}{3}\frac{\varepsilon_j - \varepsilon_{eff}}{\varepsilon_j + 2\varepsilon_{eff}} + O(x^5), \text{ and } b_{1,j} \approx -\frac{ix^5}{45}\left(\frac{\varepsilon_j}{\varepsilon_{eff}} - 1\right) + O(x^7). \tag{5.17}$$

Keeping the first term only,

$$\sum_j f_j[\frac{2}{3}\frac{\varepsilon_j - \varepsilon_{eff}}{\varepsilon_j + 2\varepsilon_{eff}}(k\frac{2}{3}x_j x_j^* + k^*\frac{1}{3}x_j^{2*}) + \frac{x_j^2}{45}(\frac{\varepsilon_j}{\varepsilon_{eff}} - 1)(k^*\frac{2}{3}^* x_j x_j^* + k\frac{1}{3}x_j^{2*})] = 0 \tag{5.18}$$

Substituting $x = kR$, $k = 2\pi m_{eff}/\lambda$, and $\varepsilon = m^2$, we have

$$\sum_j f_j[\frac{m_j^2 - m_{eff}^2}{m_j^2 + 2m_{eff}^2}(2m_{eff}^2 + m_{eff}^{2*}) + \frac{1}{30}\left(\frac{2\pi R_j}{\lambda}\right)^2 (m_j^2 - m_{eff}^2)(3m_{eff}m_{eff}^*)] = 0 \tag{5.19}$$

If the radii of inclusions are much smaller than the wavelength, then the Bruggeman mixing rule is obtained.

5.2.2. A Separated-Grain Structure (Maxwell-Garnett Type)

For a separated grain structure, we consider an inclusion particle of dielectric constant ε_i embedded in a host medium of dielectric constant ε_h. The inclusions can have arbitrary shapes in general, but in this study we consider only spherical inclusions (see Figure 5.2a). This type of composite medium can be modeled by an aggregate of coated spheres where the core is the inclusion ε_i with radius R_i and the coating is the

host medium ε_h with outer radius $R_h = R_i / f_i^{1/3}$ (see Figure 5.2b), where f_i is the volume fraction of the inclusions.

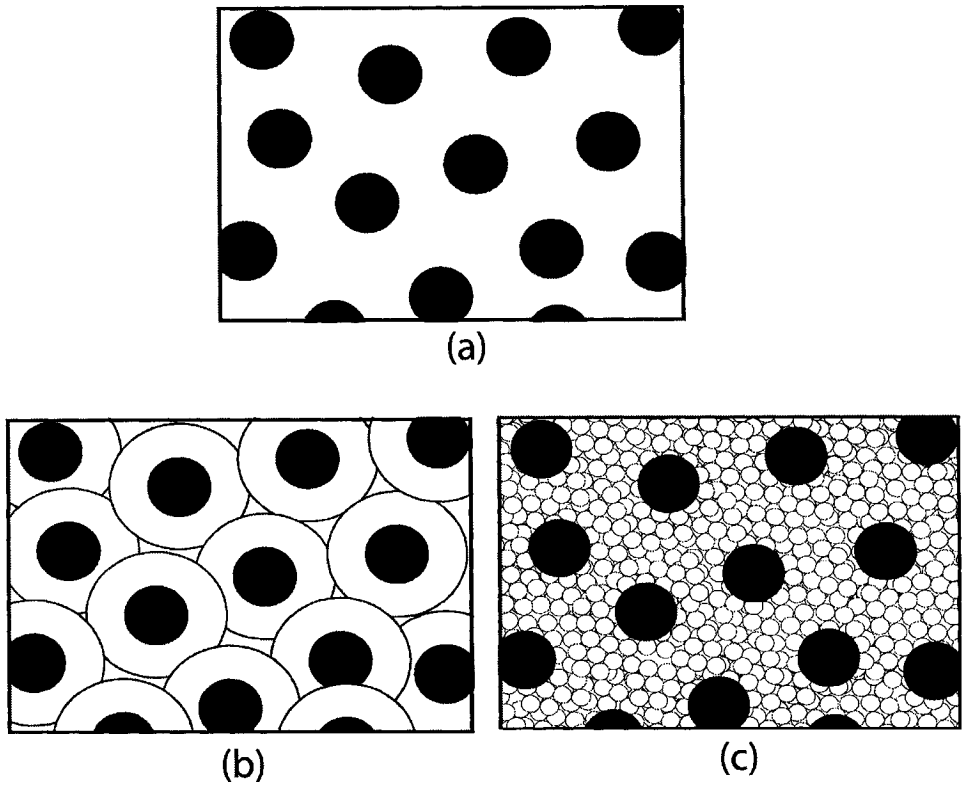

Figure 5.2: (a) a separated-grain structure, (b) an aggregate of coated spheres, and (c) an aggregate of spheres with inclusion radius R_i and host radius R_h.

The formulation for an aggregate of coated-spheres model is the same as the previous derivation for the aggregate structure. The expression for net rate of energy extinction is also the same as Eq. (5.9) and (5.10). The only difference is the expression for a_n and b_n (see chapter 4). Therefore the requirement for EMA is given by Eq. (5.14). The mixing rule Eq. (5.14) with a coated sphere model will be called Extended Maxwell-Garnett (EMG) mixing rule. The mixing rule Eq. (5.15) with coated sphere model is called Uncorrected-EMG (UEMG).

For small inclusions $x << 1$, We need to keep only the first term of expansions

$$a_{1c,j} \approx \frac{2ix^3}{3} \frac{(\varepsilon_h - \varepsilon_{eff})(\varepsilon_i + 2\varepsilon_2) + (R_i / R_h)^3 (2\varepsilon_h + \varepsilon_{eff})(\varepsilon_i - \varepsilon_h)}{(\varepsilon_h + 2\varepsilon_{eff})(\varepsilon_i + 2\varepsilon_2) + 2(R_i / R_h)^3 (2\varepsilon_h - \varepsilon_{eff})(\varepsilon_i - \varepsilon_h)} + O(x^5),$$

$$b_{1c,j} \approx \frac{ix^5}{45}[(\varepsilon_h - \varepsilon_{eff}) + (\varepsilon_i - \varepsilon_h)(R_i / R_h)^5] + O(x^7) \tag{5.20}$$

where size parameter $x = 2\pi R_h m_{med} / \lambda$. Using Eq. (5.20) and Eq. (5.14), after some manipulations, and keeping only for $a_{1c,j}$, it can be shown that the Maxwell-Garnett rule is reproduced.

The separated-grain structure can also be modeled by an aggregate of spheres with inclusion radius R_i and host radius R_h much smaller than the wavelength (or host size parameter $x << 1$, see Fig. 5.2c). For the purpose of specific calculation the host size parameter $x = 0.0001$ is used in this report.

To see differences in effective refractive indices produced by extended EMAs and uncorrected extended-EMAs, an effective refractive index for a composite material comprised of ice as the host medium and spherical waters as the inclusions with volume fraction $f = 0.125$ is calculated. The wavelength of light is taken to be 3.21 cm. In this wavelength the difference in refractive index between ice and water is large. The refractive index of ice is $m_{ice} = 1.78 + 0.0024i$, and refractive index of water is $m_w = 7.14 + 2.89i$. These refractive indices are chosen in order to see clearly the effect of the absorbing host medium. The results of effective refractive index as function of size parameter of inclusions for EBR and UEBR are shown in Fig. 5.3 and for EMG and UEMG are shown in Fig. 5.4. It is shown that the difference between the corrected and uncorrected extended EMA becomes significant for size parameter x larger than about 0.4. It is also noted from Fig. 5.3 and 5.4 that the extended EMAs depart from the Maxwell-Garnett or Bruggeman mixing rules for size parameter larger than about 0.05. It can be concluded that it is generally important to consider the corrected extended EMA.

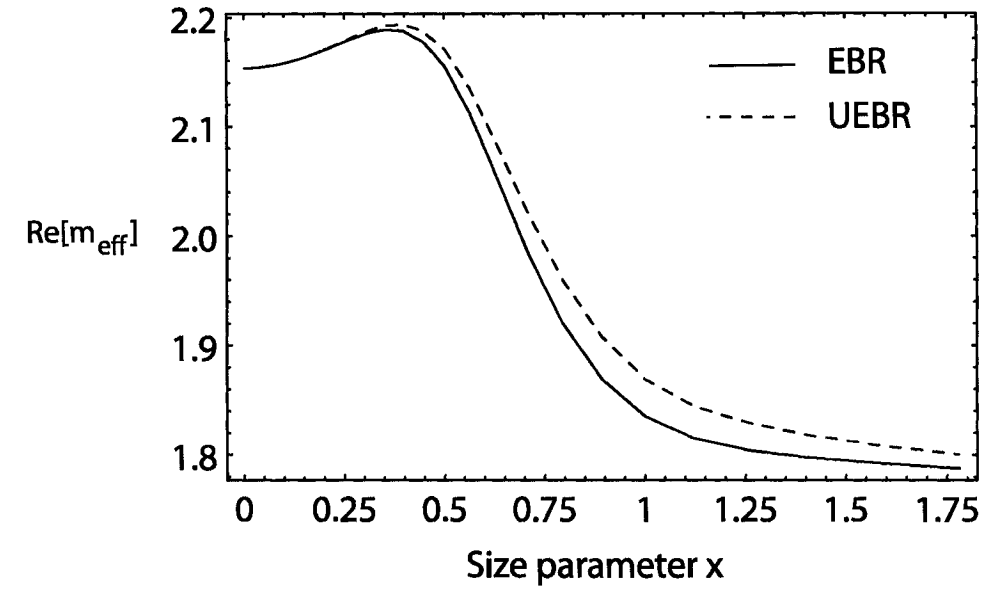

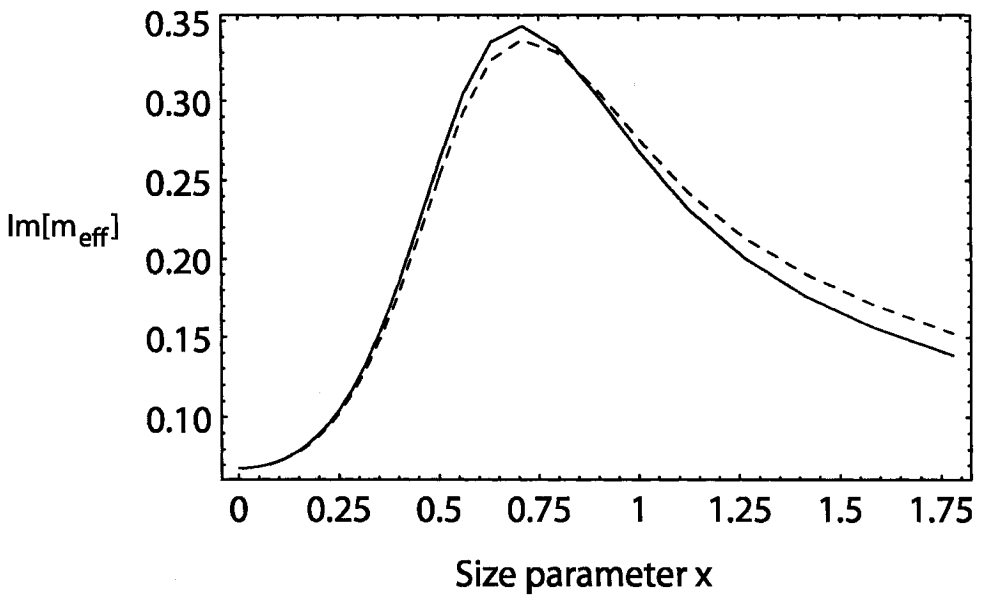

Figure 5.3: Real and imaginary part of an effective refractive index of ice (host) and spherical water (inclusions) for extended Bruggeman (EBR) and uncorrected EBR (UEBR) as a function of size parameter x ($x = 2\pi a \mathrm{Re}[m_{ice}]/\lambda$, where a is radius of spherical inclusions and λ is the wave length in a vacuum). We use volume fraction of water $f = 0.125$. The refractive indices are $m_{ice} = 1.78 + 0.0024i$, and $m_w = 7.14 + 2.89i$.

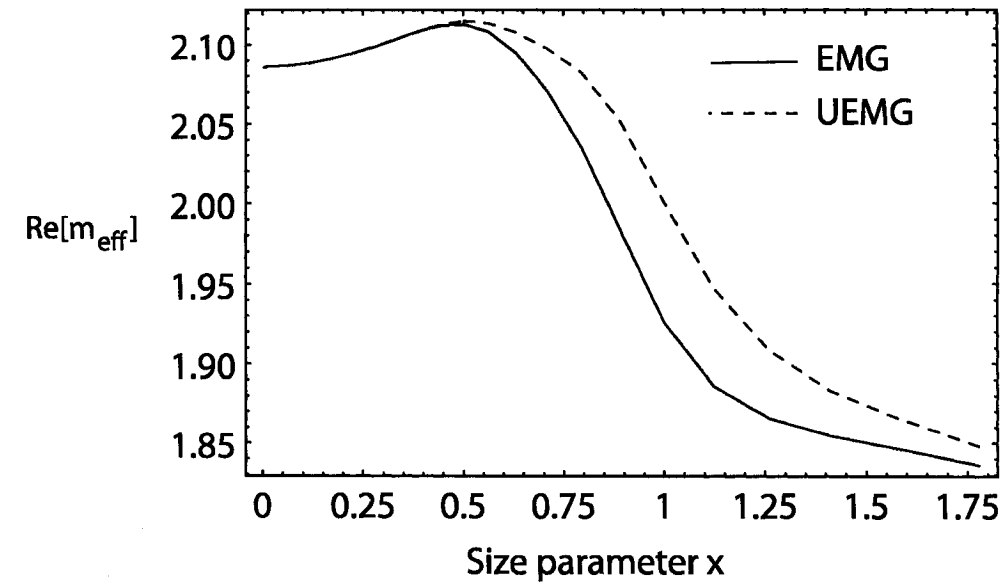

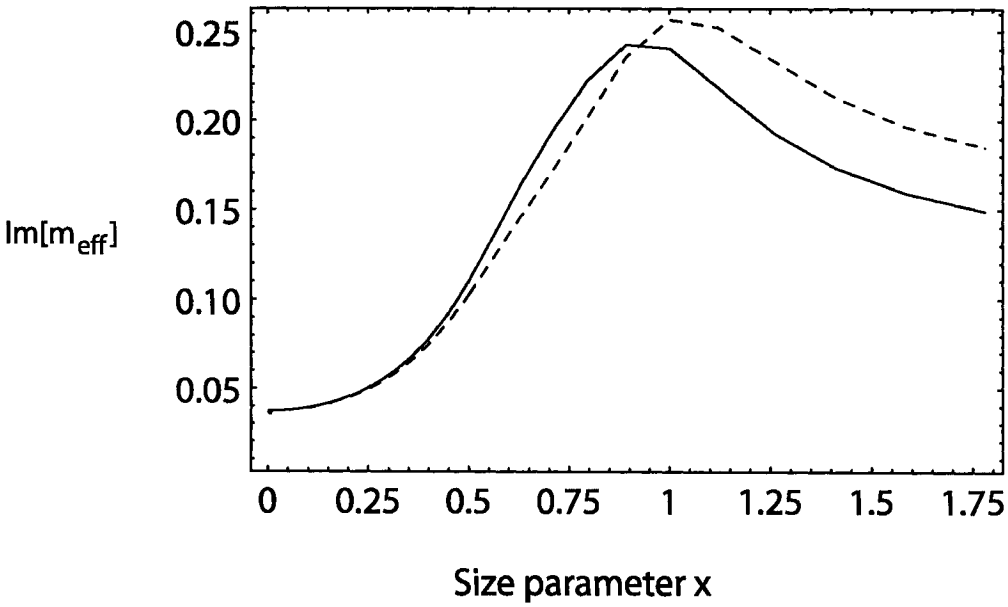

Figure 5.4: The same as Figure 5.3 except that these are for the real and the imaginary part of effective refractive index for extended Maxwell-Garnett (EMG) and uncorrected EMG (UEMG) as a function of size parameter x ($x = 2\pi a \,\mathrm{Re}[m_{ice}]/\lambda$, where a is radius of spherical inclusions).

5.3.3. Equivalence of Absorbed Energy Model

In the previous discussion, we have used the equivalence of extinction for defining an effective medium. Similarly, we can employ an equivalence of energy absorbed by a medium. The requirement for EMA using the absorbed energy is

$$\sum_j n_j \left(\iiint_{V_j} U_j(\mathbf{r}) \mathrm{d}^3 r - \iiint_{V_j} U_{eff}(\mathbf{r}) \mathrm{d}^3 r \right) = 0 \tag{5.21}$$

where $n_j = f_j / (\frac{4}{3}\pi R_j^3)$ is the number concentration of the jth sphere, $U_j(\mathbf{r})$ and $U_{eff}(\mathbf{r})$ are the absorbed electric energy of the jth sphere and for a spherical volume of effective medium respectively, and the integration is over the volume of the jth sphere.

For a harmonic field in a linear medium, the previous analysis (see chapter 4) has shown that the absorbed electric energy density is proportional to

$$U(\mathbf{r}) = \mathrm{Im}[\varepsilon(\mathbf{r})] |\mathbf{E}(\mathbf{r})|^2 \tag{5.22}$$

where ε is the permittivity of a medium. Because we have used the imaginary part of permittivity, the equivalence of absorbed energy can only be applied for a mixture of absorbing materials.

The solution of a scattering of electromagnetic plane wave by a homogenous spherical particle is given in chapter 4. From an analysis in chapter 4 (Eq. (4.17)), the energy content inside the ith sphere is

$$\begin{aligned} \iiint_{V_j} U_j(\mathbf{r}) \mathrm{d}^3 r = 2\pi \, \mathrm{Im}[\varepsilon_j] \sum_{n=1}^{\infty} & (2n+1) |c_{n,j}|^2 \int_0^{R_j} |j_n(k_j r)|^2 r^2 dr + \\ & |d_{n,j}|^2 \int_0^{R_j} \{(n+1) |j_{n-1}(k_j r)|^2 + n |j_{n+1}(k_j r)|^2 \} r^2 dr \end{aligned} \tag{5.23}$$

where for simplicity in derivation we use $\varepsilon_0 |E_0|^2 = 1$, since it is only a proportionality constant. The energy content in a spherical volume of the effective medium can be shown to be

$$\iiint_{V_j} U_{eff}(\mathbf{r}) \mathrm{d}^3 r = \frac{4}{3} \pi R_j^3 \, \mathrm{Im}[\varepsilon_{eff}] \tag{5.24}$$

where similarly we have used $\varepsilon_0 |E_0|^2 = 1$.

In the limit of small spheres ($R_j << \lambda$) or long wavelength limit, we need to consider only the first term of scattering coefficients ($n = 1$).

$$\iiint_{V_j} U_j(\mathbf{r})\mathrm{d}^3 r = \frac{4\pi R_j^3}{3}\mathrm{Im}[\varepsilon_j]\left|\frac{3\varepsilon_{eff}}{\varepsilon_j + 2\varepsilon_{eff}}\right|^2 \tag{5.25}$$

After substitution, we have

$$\mathrm{Im}\left\{ f_1\left[\varepsilon_1\left|\frac{3\varepsilon_{eff}}{\varepsilon_1 + 2\varepsilon_{eff}}\right|^2 - \varepsilon_{eff}\right] + f_2\left[\varepsilon_2\left|\frac{3\varepsilon_{eff}}{\varepsilon_2 + 2\varepsilon_{eff}}\right|^2 - \varepsilon_{eff}\right]\right\} = 0 \tag{5.26}$$

Alternatively, we can use the net rate of energy absorption by a spherical particle given by Eqs. (4.13) and (4.14). The EMA requirement is now

$$\sum_j n_j (W_{abs,j} - W_{abs,eff,j}) = 0,$$

$$\mathrm{Im}\{k_0^* \sum_j n_j \sum_{n=1}^{\infty} (2n+1)(b_n \psi_n'^*(x)\xi_n(x) + b_n^* \psi_n(x)\xi_n'^*(x) + |a_n|^2 \xi_n'(x)\xi^*{}_n(x)$$
$$- |b_n|^2 \xi_n(x)\xi'^*{}_n(x) - a_n \psi_n^*(x)\xi_n'(x) - a_n^* \psi_n'(x)\xi_n^*(x)) \} = 0 \tag{5.27}$$

The expression for a separated-grain structure is determined in similar way as previous discussion.

5.2.4 Multiple Scattering Approaches

The extended Bruggeman and the Maxwell-Garnett approaches are based on extinction and absorbed energy of a single (homogeneous or coated) spherical particle embedded in a homogeneous effective medium. For high frequency wave the effect of multiple scattering is significant, especially when the volume fraction of inclusion is comparable to the host medium. We can develop an effective medium approximation by solving Maxwell's equations for randomly positioned particles. For spherical inclusions it has been done by Tsang and Kong (1980), for nonspherical particles by Twersky (1977, 1978) and Varadan et al. (1987a, 1987b) and recently also by Ao and Kong (2002).

For spherical shapes the well-known approximations are Foldy's approximation (also called the effective field approximation (EFA)), the quasi-crystalline approximation (QCA) and the QCA with coherent potential (QCA-CP). QCA-CP has been found to be

the most accurate method of these three. In the limit of small inclusion (compared to the wavelength and for non-overlapping spherical inclusions, which corresponds to the Percus-Yevick (PY) pair distribution function (Percus and Yevick, 1958), the effective medium approximations using these methods are given by

$$\text{EFA}: \varepsilon_{eff} = \varepsilon_h\left[1+\frac{3\varepsilon_d f}{\varepsilon_d+3}+i\frac{2x^3\varepsilon_d^2 f}{(\varepsilon_d+3)^2}\right],$$

$$\text{QCA-PY}: \varepsilon_{eff} = \varepsilon_h\left[1+\frac{3\varepsilon_d f}{\varepsilon_d(1-f)+3}+i\frac{2x^3\varepsilon_d^2 f}{[\varepsilon_d(1-f)+3]^2}\frac{(1-f)^2}{(1+2f)^2}\right],$$

QCA-CP-PY:

$$\varepsilon_{eff} = \varepsilon_h\left[1+\frac{3\varepsilon_d f(\varepsilon_{eff}/\varepsilon_h)}{\varepsilon_d(1-f)+3(\varepsilon_{eff}/\varepsilon_h)}+i\frac{2x^3\varepsilon_d^2(\varepsilon_{eff}/\varepsilon_h)^{5/2} f}{[\varepsilon_d(1-f)+3(\varepsilon_{eff}/\varepsilon_h)]^2}\frac{(1-f)^2}{(1+2f)^2}\right],$$

where $\varepsilon_d = (\varepsilon_i - \varepsilon_h)/\varepsilon_h$, f and x are the volume fraction and size parameter of inclusions respectively.

A Mathematica notebook written to compute the effective refractive indices from analytical EMAs presented in this chapter is provided in Sudiarta (2003a).

5.3 Operational EMA for a Scattering Problem

Instead of previous analytical expressions for the definition of effective medium, we can also directly define various requirements for EMAs if we know the distribution of fields inside a composite material. Using the FDTD method, a scattering by a particle with inclusions is solved and the internal fields can be obtained. Following Chylek et al. (1999), effective dielectric constants can be defined following two homogenization requirements. As in previous discussion, the two requirements for an effective dielectric are the total cross section model and the energy density model.

Effective dielectric constants or refractive indices are computed using the following methods. The first method is

Method 1 (M1):
$$\varepsilon_{eff} = \frac{\sum \iiint_V \varepsilon(\mathbf{r})|\mathbf{E}|^2 \mathrm{d}^3 r}{\sum \iiint_V |\mathbf{E}|^2 \mathrm{d}^3 r} \tag{5.27}$$

where $\mathbf{E}$ is the electric field inside a particle, the sum $\sum$ is over a number N of FDTD simulations with different randomly positioned inclusions, and the volume integration is over a volume of the host particle. We note here that the dielectric constant is weighted by $|\mathbf{E}|^2$. The weighting factor $|\mathbf{E}|^2$ is related to the energy density inside a spherical particle. The energy absorbed by a particle is proportional to $\mathrm{Im}\{\iiint_V \varepsilon(\mathbf{r})|\mathbf{E}|^2 \mathrm{d}^3 r\}$.

Therefore, the method 1 corresponds to the equivalence of absorption between a heterogeneous particle and homogenous particle with an effective dielectric constant.

Instead of using a dielectric constant, a refractive index can also be used for an averaging scheme.

Method 2 (M2):
$$m_{eff} = \frac{\sum \iiint_V m(\mathbf{r})|\mathbf{E}|^2 \mathrm{d}^3 r}{\sum \iiint_V |\mathbf{E}|^2 \mathrm{d}^3 r} \tag{5.28}$$

Another scheme is to use a weighting factor $\mathbf{E} \cdot \mathbf{E}_i^*$ (where $\mathbf{E}_i$ is the incident field) since it is known that the extinction energy is proportional to $\mathrm{Im}\{\iiint_V (\varepsilon(\mathbf{r}) - 1)\mathbf{E} \cdot \mathbf{E}_i^* \mathrm{d}^3 r\}$.

Hence, another effective medium scheme is defined as

Method 3 (M3):
$$\varepsilon_{eff} = \frac{\sum \iiint_V \varepsilon(\mathbf{r})\mathbf{E} \cdot \mathbf{E}_i^* \mathrm{d}^3 r}{\sum \iiint_V \mathbf{E} \cdot \mathbf{E}_i^* \mathrm{d}^3 r} \tag{5.29}$$

Instead of using method 1 and 3, a combination of the two methods can be used. We first determine the imaginary part of effective dielectric constant using method 1 and the real part of dielectric constant is computed by requiring that the equivalence of extinction energy.

Method 1 & 3 (M1&3):
$$\varepsilon_{eff,I} = \frac{\mathrm{Im}\{\sum \iiint_V \varepsilon\ (\mathbf{r})|\mathbf{E}|^2 \mathrm{d}^3 r\}}{\sum \iiint_V |\mathbf{E}|^2 \mathrm{d}^3 r} \tag{5.30}$$

$$\varepsilon_{eff,R} = \frac{\mathrm{Im}\{\sum \iiint_V \varepsilon(\mathbf{r})\mathbf{E}\cdot\mathbf{E}_i^* \mathrm{d}^3 r\} - \varepsilon_{eff,i}\,\mathrm{Re}\{\sum \iiint_V \mathbf{E}\cdot\mathbf{E}_i^* \mathrm{d}^3 r\}}{\mathrm{Im}\{\sum \iiint_V \mathbf{E}\cdot\mathbf{E}_i^* \mathrm{d}^3 r\}} \tag{5.31}$$

The numerical schemes given in this section 5.3 have not been used previously and their validity for applications is not known. In the next chapter, FDTD simulations are performed and the numerical schemes are examined.

5.4 Summary

Various effective medium approximations (EMAs) are discussed in this chapter. Three analytical EMA approaches are (a) extinction based EMA, (b) absorption based EMA, and (c) EMA based on multiple scattering approach. The classical EMAs, such as the Maxwell-Garnett and the Bruggeman, are extended to include the effect of inclusion size. The new formulation of extinction and absorption for light scattering by a spherical particle in an absorbing medium, as discussed in chapter 4, is used here to reformulate the extended EMAs. Some differences in the resulting effective refractive indices are noted when the extended EMAs with an absorbing medium correction is used. Four numerical approaches for calculating an effective medium are also presented. These EMAs are tested using the FDTD method in the next chapter.

Chapter 6

Numerical Results and Discussion

In this chapter various effective medium approximations (EMAs), as discussed in chapter 5, are tested using the FDTD method. The FDTD method is used to obtain the scattering properties and the distribution of internal fields of a heterogeneous particle. Then, the effective refractive indices of various EMAs are calculated and compared. The effective refractive indices from analytical EMAs are computed using the Mathematica program. A Mathematica notebook for this purpose is given in Sudiarta (2003a). The purpose of this test is to determine the appropriate EMA for a given specified geometrical structure of a heterogeneous particle.

For a practical application of EMAs, we consider a scattering by a particle with multiple inclusions. This type of particle is of considerable importance for atmospheric applications. An example is a hail particle which is comprised of a mixture of ice, water and air bubbles. Other examples are black carbon–sulfate mixture and black carbon–water mixture. Because we consider many realizations of positions of the inclusions, we need to average the single scattering properties. We define optical properties of the heterogeneous particle by averaging over N realizations of the positions of inclusions. For example,

$$< \sigma_{sca} >= \frac{1}{N} \sum_{j=1}^{N} \sigma_{sca,j} \tag{6.1}$$

and

$$< S_{11} >= \frac{1}{N}\sum_{j=1}^{N} S_{11,j} \tag{6.2}$$

We define also a normalized, azimuthally averaged phase function and asymmetry factor by

$$P(\theta) = \frac{\int_0^{2\pi} < S_{11} > d\phi}{\int_0^{\pi}\int_0^{2\pi} < S_{11} > \sin(\theta) d\phi d\theta}$$

$$g = \int_0^{\pi} P(\theta)\cos(\theta)\sin(\theta) d\theta \,. \tag{6.3}$$

In this thesis we only consider a mixture of water and ice at 3.21 cm wavelength. The values of refractive indices used here are given in Table 6.1. The reason for choosing these values is that the differences in refractive index between water and ice are large. We expect that the effective refractive indices obtained using various EMAs would be significantly different from each other. This makes it easier to differentiate between various EMAs and to determine which is more accurate for a prescribed structure.

Table 6.1: The values of refractive indices of water and ice at 3.21 cm wavelength.

Medium	Refractive index
Ice	$1.78 + 0.0024\,i$
Water	$7.14 + 2.89\,i$

To test various EMAs, we use a spherical ice particle with multiple spherical water inclusions. The random positioned spherical inclusions are placed sequentially inside the sphere with a requirement that the inclusions cannot overlap.

There are four cases are investigated here. They are (a) very small spherical inclusions, (b) finite size inclusions, (c) only one inclusion and (d) clusters of inclusions.

6.1 Case A: Very Small Inclusions

We first consider an ice sphere with very small spherical water inclusions (size parameter

$x << 1$). This is important for testing the validity of the Maxwell-Garnett and the Bruggeman mixing rules. As mentioned in chapter 5 that the Maxwell-Garnett and the Bruggeman are derived in the limit of a very small spherical particle or in the limit of a static field.

To model a very small spherical particle in the FDTD mesh accurately, an approach given in chapter 2 is used. In this approach, a very small spherical particle is represented by an FDTD cubic cell. It was shown that because of the nature of FDTD mesh, a cube of material located at a position of a component of the electric fields has polarizability in the direction of the field component. It is, therefore, anisotropic. Because we consider an isotropic composite material, we need to assign the same number of cubes for each component of the electric fields. The cubes are then randomly placed inside the host sphere. To satisfy the requirement of smallness of the inclusions and to ensure the validity of the cubic approximation, we used an FDTD parameter $\lambda / \Delta s = 400$. The size parameter of an equal-volume sphere is $x_w \approx 0.00974$. For calculations we used a personal computer with Intel pentium4 2.66 GHz processor and 785 Mbytes memory. Using these computational resources, our first calculation is limited to a host size parameter 0.5. The number of inclusions is taken to be 5,000, 10,000 and 20,000. These correspond to volume fractions of 0.037, 0.074 and 0.148. For each volume fraction, we consider several FDTD simulations with different realizations of the positions of the inclusions, and in each FDTD simulation the scattering properties for two linear polarizations of incident waves are computed.

Values of effective refractive indices, efficiencies, and asymmetry factor obtained from the FDTD method, and Mie calculations with effective refractive indices obtained using various EMAs are shown in Table 6.2-6.4.

It is noted that the numerical method 3 (M3) (based on the numerical averaging by extinction) is the most accurate method for all volume fractions, and its relative errors are generally less than 1%. The numerical method 1 (M1), which is based on the numerical averaging of internal energy (or absorbed energy), gives accurate results only for the absorption efficiency. The M1 gives relative errors less than about 2% for absorption efficiencies and gives large relative errors (larger than 10%) for scattering and extinction efficiencies. The numerical method 2 (M2) produces inaccurate results for all

efficiencies. The relative errors of the M2 can be as large as 70%. The combination of numerical method M1 and M3 (M1 & 3) was constructed in such a way to minimize both extinction and absorption but it does not perform as expected. This might be due to numerical errors in the implementation of the FDTD method, since it was shown in chapter 2 that the cubic approximation of sphere gives about 1-2% relative error. We note also in Table 6.2 – 6.4 that the relative errors in efficiencies of the M3 are about 1-2%. The M1 gives also about 1-2% relative error in absorption efficiency. Therefore combining the M1 and the M2 may cause an increase in relative errors.

EMAs that are based on volume averages of dielectric constants, refractive indices, and cube root of dielectric constants generally give relative errors much larger than 10%. These methods generally overestimate the amount of absorption because the imaginary part of the effective refractive indices are too large. Of these methods, we note that the average of dielectric constants give the largest relative errors and the average of cube root of dielectric constant give the least errors.

It is noted that the refractive indices of the extended-EMAs are close to the refractive indices of the Maxwell-Garnett and Bruggeman rules. This is expected since in the limit of a small particle ($x << 1$), the extended EMAs should give the same results as the Maxwell-Garnett and the Bruggeman results. From the results, it is clearly shown that the Bruggeman results are more accurate than the Maxwell-Garnett results. This indicates that the Bruggeman model is more appropriate than the Maxwell-Garnett model for a composite medium with inclusion sizes much smaller than the wavelength.

The inverted Maxwell-Garnett is found to produce the largest relative errors. It is understood since the errors are mainly from an incorrect assumption of the topology of the ice-water mixture. Here we have water inclusions embedded in an ice matrix. However, the inverted Maxwell-Garnett assumes ice inclusions embedded in a water matrix (an inverted topology). Therefore it is important to consider the topology of a composite before applying the Maxwell-Garnett formulae.

For multiple scattering approaches, the EFA and the QCA-PY show large relative errors for all efficiencies. On the other hand, the QCA-CP-PY gives reasonable results (relative errors less than 5%) for small volume fraction less than 0.1. For a larger volume fraction the QCA-CP-PY overestimates the efficiencies. This is in contrast to the

Bruggeman and Maxwell-Garnett, which generally underestimate the efficiencies. Of the multiple scattering approaches the QCA-CP-PY method is concluded to be the best method.

Table 6.2: Effective refractive indices of various effective medium approximations, and calculated efficiencies and asymmetry factors of a spherical ice ($m_{ice} = 1.78 + 0.0024i$, $x_{ice} = 0.5$) with spherical water inclusions ($m_w = 7.14 + 2.89\,i$, size parameter $x_w \approx 0.00974$, with water volume fraction $f_w = 0.037$) obtained from an FDTD method and Mie theory with effective refractive indices of numerical method 1-3 (M1-3), method 1&3, volume average of dielectric constants $< \varepsilon >$, volume average of refractive indices $< m >$, volume average of cube root of dielectric constant $< \varepsilon^{1/3} >$, Bruggeman (BR), Maxwell-Garnett (MG), inverted MG (IMG), extended BR (EBR,using extended EMA-aggregate model with absorbing medium correction), uncorrected EBR (UEBR, using extended EMA-aggregate model without absorbing medium correction), extended MG (EMG, using Extended EMA-separated grain model with absorbing medium correction), uncorrected EMG (UEMG, without absorbing medium correction), effective field approximation (EFA), quasi crystalline approximation with Percus Yevick pair distribution (QCA-PY), and QCA with coherent potential (CP) with PY distribution (QCA-CP-PY). The FDTD parameter $\lambda / \Delta s$ is 400.

	Effective Refractive Indices		Scattering Properties				Relative Error (%)			
	mr	mi	Qext	Qsca	Qabs	g	δQ_{ext}	δQ_{sca}	δQ_{abs}	δg
Mean of FDTD results			0.0511	0.0375	0.0136	0.0580	0.2	0.0	0.7	0.1
Std deviation of FDTD results			0.0001	0.0000	0.0001	0.0001				
M1	1.79100	0.01400	0.0453	0.0318	0.0135	0.0562	-11	-15	-0.3	-3
M2	1.78521	0.00531	0.0366	0.0314	0.0052	0.0560	-28	-16	-62	-3
M3	1.87459	0.01463	0.0507	0.0373	0.0135	0.0587	-1	-1	-1	1
M1&3	1.91751	0.01308	0.0519	0.0401	0.0118	0.0600	2	7	-13	3
$< \varepsilon >$	2.18011	0.35219	0.3274	0.0618	0.2656	0.0686	541	65	1857	18
$< m >$	1.97838	0.10927	0.1387	0.0445	0.0942	0.0621	171	19	594	7
$< \varepsilon^{1/3} >$	1.93682	0.07083	0.1042	0.0415	0.0627	0.0607	104	11	362	5
BR	1.87352	0.01400	0.0501	0.0372	0.0129	0.0586	-2	-1	-5	1
MG	1.86834	0.01212	0.0481	0.0369	0.0112	0.0585	-6	-2	-17	1
IMG	2.06274	0.25230	0.2570	0.0520	0.2050	0.0648	403	39	1411	12
EBR	1.87356	0.01402	0.0501	0.0372	0.0129	0.0586	-2	-1	-5	1
UEBR	1.87356	0.01402	0.0501	0.0372	0.0129	0.0586	-2	-1	-5	1
EMG	1.86836	0.01213	0.0481	0.0369	0.0112	0.0585	-6	-2	-17	1
UEMG	1.86834	0.01212	0.0481	0.0369	0.0112	0.0585	-6	-2	-17	1
EnBR	1.79788	0.01203	0.0438	0.0323	0.0116	0.0564	-14	-14	-15	-3
EnMG	1.79773	0.01195	0.0438	0.0322	0.0115	0.0564	-14	-14	-15	-3
EFA	1.86554	0.01151	0.0473	0.0367	0.0107	0.0584	-7	-2	-21	1
QCA	1.86834	0.01212	0.0481	0.0369	0.0112	0.0585	-6	-2	-17	1
QCACPPY	1.87628	0.01511	0.0513	0.0374	0.0139	0.0587	0.4	-0.3	2	1

Table 6.3: The same as Table 6.2, except the volume fraction of water f_w is 0.074.

	Effective Refractive Indices		Scattering Properties				Relative Error (%)			
	mr	mi	Qext	Qsca	Qabs	g	δQ_{ext}	δQ_{sca}	δQ_{abs}	δg
Mean of FDTD results			0.0753	0.0450	0.0302	0.0613	0.3	0.1	0.7	0.2
Std deviation of FDTD results			0.0002	0.0000	0.0002	0.0001				
M1	1.80845	0.03170	0.0632	0.0329	0.0303	0.0568	-16	-27	0	-7
M2	1.79364	0.00983	0.0415	0.0320	0.0095	0.0563	-45	-29	-69	-8
M3	1.98561	0.03495	0.0748	0.0447	0.0302	0.0623	-1	-1	0	2
M1&3	2.26084	0.02535	0.0818	0.0630	0.0188	0.0725	9	40	-38	18
$< \varepsilon >$	2.54021	0.60285	0.4578	0.0904	0.3674	0.0811	508	101	1115	32
$< m >$	2.17676	0.21615	0.2242	0.0588	0.1654	0.0691	198	31	447	13
$< \varepsilon^{1/3} >$	2.09725	0.14297	0.1677	0.0527	0.1150	0.0663	123	17	280	8
BR	1.98034	0.03100	0.0711	0.0443	0.0268	0.0621	-5	-2	-11	1
MG	1.95844	0.02226	0.0624	0.0428	0.0195	0.0614	-17	-5	-35	0
IMG	2.33248	0.45001	0.3834	0.0738	0.3095	0.0739	409	64	924	20
EBR	1.98042	0.03105	0.0712	0.0443	0.0269	0.0621	-5	-2	-11	1
UEBR	1.98042	0.03105	0.0712	0.0443	0.0269	0.0621	-5	-2	-11	1
EMG	1.95847	0.02229	0.0624	0.0428	0.0196	0.0614	-17	-5	-35	0
UEMG	1.95847	0.02230	0.0624	0.0428	0.0196	0.0614	-17	-5	-35	0
EnBR	1.81673	0.02219	0.0546	0.0335	0.0211	0.0570	-27	-26	-30	-7
EnMG	1.81555	0.02155	0.0539	0.0334	0.0205	0.0569	-28	-26	-32	-7
EFA	1.94735	0.01986	0.0596	0.0421	0.0175	0.0610	-21	-6	-42	-1
QCA	1.95843	0.02226	0.0624	0.0428	0.0195	0.0614	-17	-5	-35	0
QCACPPY	1.99258	0.03693	0.0769	0.0451	0.0317	0.0625	2	0	5	2

Table 6.4: The same as Table 6.2, except the volume fraction of water f_w is 0.148.

	Effective Refractive Indices		Scattering Properties				Relative Error (%)			
	mr	mi	Qext	Qsca	Qabs	g	dQ_{ext}	dQ_{sca}	dQ_{abs}	dg
Mean of FDTD results			0.1479	0.0638	0.0840	0.0709	0.2	0.0	0.3	0.1
Std deviation of FDTD results			0.0002	0.0000	0.0002	0.0001				
M1	1.87194	0.09350	0.1231	0.0373	0.0858	0.0587	-17	-41	2	-17
M2	1.82444	0.02630	0.0589	0.0340	0.0249	0.0572	-60	-47	-70	-19
M3	2.25948	0.11320	0.1466	0.0631	0.0835	0.0726	-0.9	-1.0	-0.7	2.4
M1&3	0.06552	2.67119	0.8421	0.6963	0.1458	-0.0169	469	991	73	-124
$< \varepsilon >$	3.15439	0.96959	0.5835	0.1299	0.4536	0.1033	294	104	440	46
$< m >$	2.57352	0.42989	0.3513	0.0873	0.2641	0.0852	137	37	214	20
$< \varepsilon^{1/3} >$	2.42872	0.29785	0.2745	0.0760	0.1984	0.0794	86	19	136	12
BR	2.24204	0.09227	0.1306	0.0619	0.0688	0.0719	-12	-3	-18	1
MG	2.14535	0.04432	0.0903	0.0554	0.0349	0.0680	-39	-13	-58	-4
IMG	2.82575	0.76056	0.5133	0.1097	0.4037	0.0921	247	72	380	30
EBR	2.24222	0.09244	0.1308	0.0619	0.0689	0.0719	-12	-3	-18	1
UEBR	2.24222	0.09243	0.1308	0.0619	0.0689	0.0719	-12	-3	-18	1
EMG	2.14542	0.04438	0.0903	0.0554	0.0350	0.0680	-39	-13	-58	-4
UEMG	2.14540	0.04438	0.0903	0.0554	0.0350	0.0680	-39	-13	-58	-4
EnBR	1.85784	0.04434	0.0773	0.0362	0.0411	0.0582	-48	-43	-51	-18
EnMG	1.85246	0.04143	0.0744	0.0358	0.0386	0.0581	-50	-44	-54	-18
EFA	2.10152	0.03478	0.0805	0.0524	0.0281	0.0663	-46	-18	-67	-6
QCA	2.14534	0.04432	0.0903	0.0554	0.0349	0.0680	-39	-13	-58	-4
QCACPPY	2.29703	0.13305	0.1617	0.0657	0.0960	0.0741	9	3	14	5

The energy-based approaches using the Maxwell-Garnett model (EnMG) and the Bruggeman model (EnBR) show large relative errors. The errors can be as high as 50%. The difference between EMAs with and without the absorbing medium corrections is negligible due to the small size inclusion used.

The resulted phase functions are shown in Figs. 6.1-6.5. Because we have used a small host sphere $x_{ice} = 0.5$ the phase functions do not change considerably for different effective refractive indices. The relative errors in phase function are generally less than 5%.

We next study the effect of changing the size of the host particle. For this study we use a size parameter of the host particle $x_{ice} = 0.25$. We perform FDTD simulations for the same volume fraction as previous simulations. The results are shown in Tables 6.5 and 6.6. The effective refractive indices obtained from the analytical EMAs are the same as those in Tables 6.2 and 6.3 since the volume fractions and the inclusion sizes are the same. Small differences (less than about 1%) are noted for the refractive indices of the M1, M2, and M3. The refractive index of M1&3 is shown to be sensitive to the size parameter of host particle. It is found also here that the M3 results are very close to the FDTD results. The QCA-CP-PY gives relative errors less than about 2%.

The previous FDTD results have shown that the M3 gives accurate results for all efficiencies. A further comparison, as shown in Fig. 6.6, indicates the relative errors of the M3 are mostly less than 6%. Therefore we can consider the M3 to be the accurate method for obtaining effective refractive indices. We can use the M3 as a reference for comparison with other analytical EMAs. Figures 6.7 and 6.8 show the real and imaginary parts of effective refractive indices computed by the M3, the Bruggeman, the Maxwell-Garnett, and the QCA-CP-PY mixing rules. Here we did not show the extended EMAs, because the resulted effective refractive indices are very close to the Bruggeman and the Maxwell-Garnett method. Other mixing rules do not show an improvement over the Bruggeman or the Maxwell-Garnett results and therefore they are not considered here.

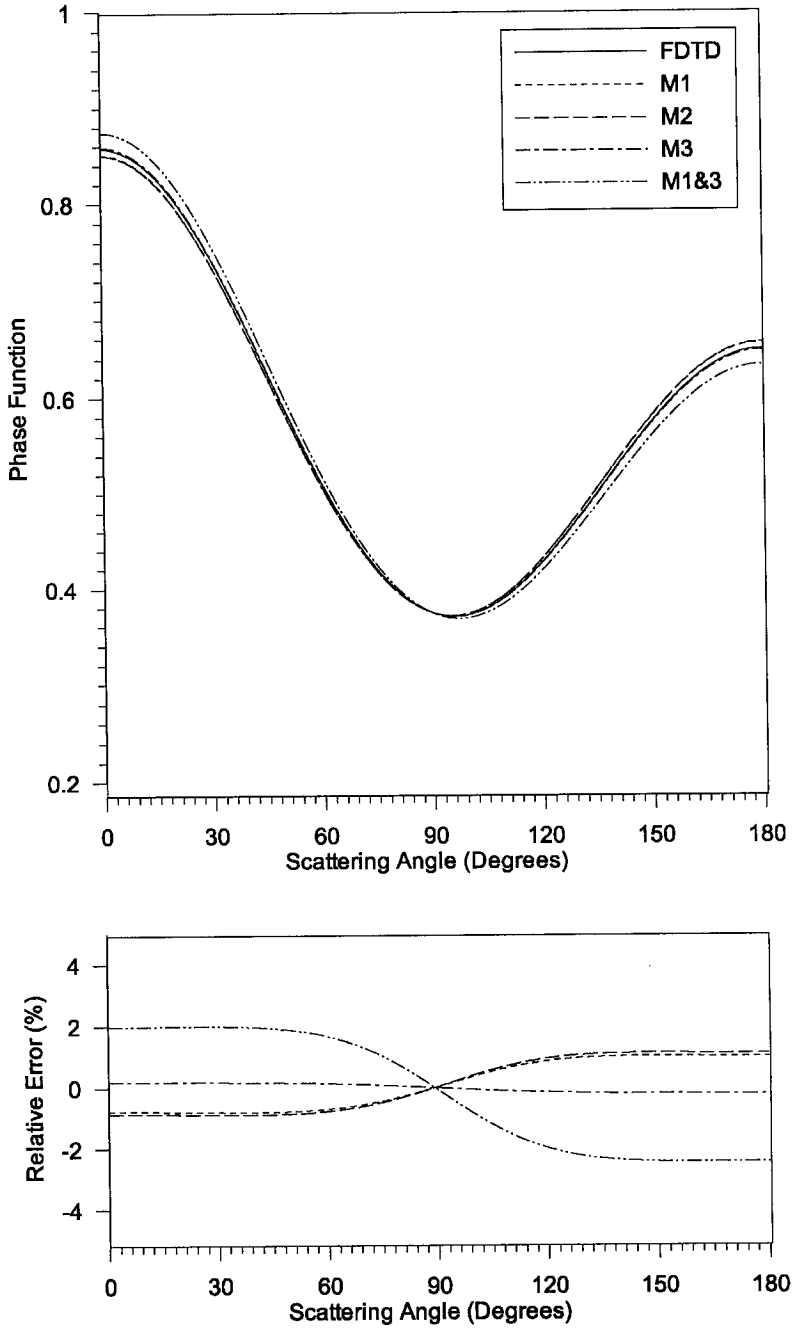

Figure 6.1: The phase function of ice sphere (size parameter 0.5) with 10,000 spherical water inclusions (size parameter $x_w \approx 0.00974$) or volume fraction 0.074, calculated by the FDTD method and Mie calculations with effective refractive indices obtained from the numerical mixing rules (method 1, 2, 3 (M1, 2, 3) and a combination of M1 and M3 (M1&3)).

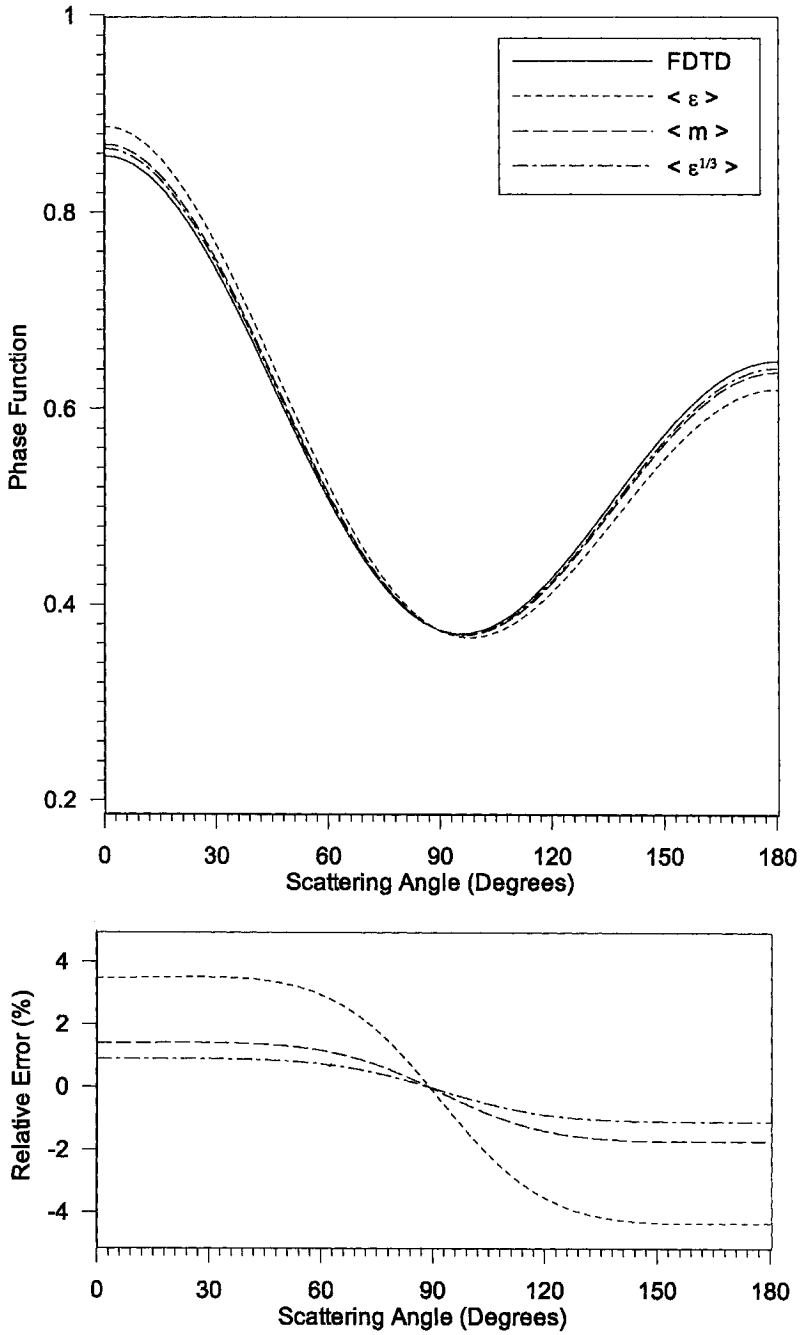

Figure 6.2: The same as Fig. 6.1 except the effective refractive indices are obtained from the volume average of dielectric constants $< \varepsilon >$, refractive indices $< m >$ and cube root of dielectric constant $< \varepsilon^{1/3} >$ mixing rules.

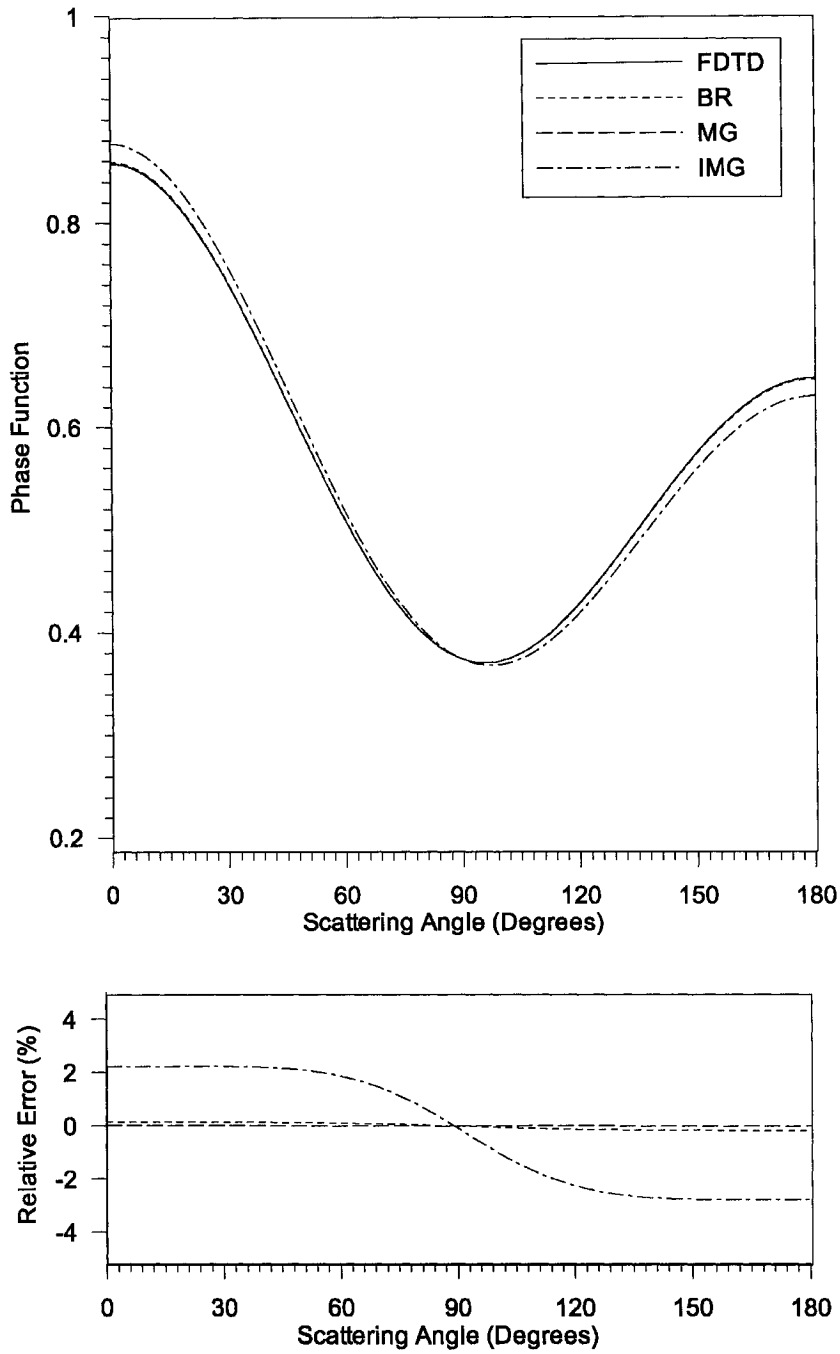

Figure 6.3: The same Fig. 6.1 except the effective refractive indices are obtained from the Maxwell-Garnett (MG), the Inverted MG, and the Bruggeman (BR). Note that the results for the extended MG and the extended BR are the same as MG and BR respectively.

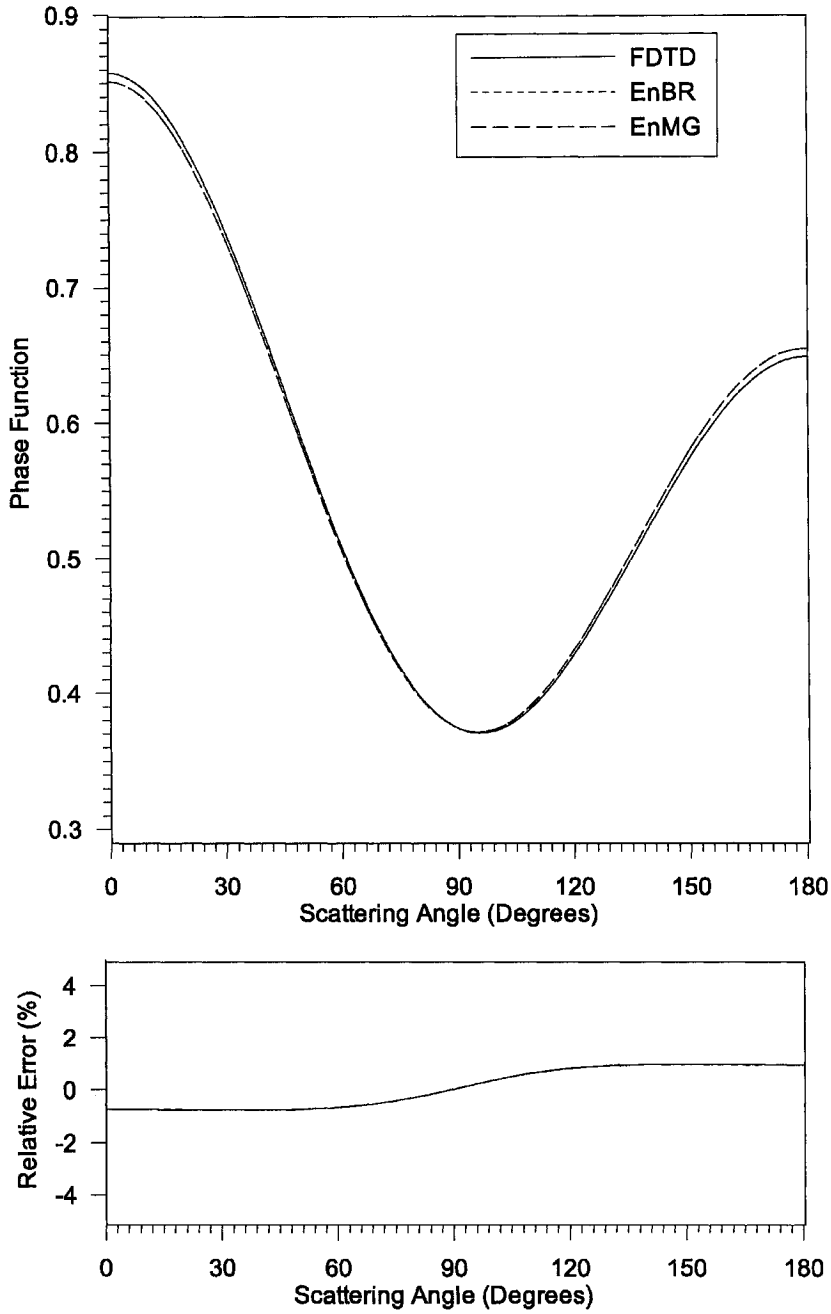

Figure 6.4: The same as Fig. 6.1 except the effective refractive indices are obtained from energy based EMAs (energy based Bruggeman model (EnBR) and energy based Maxwell-Garnett model (EnMG)).

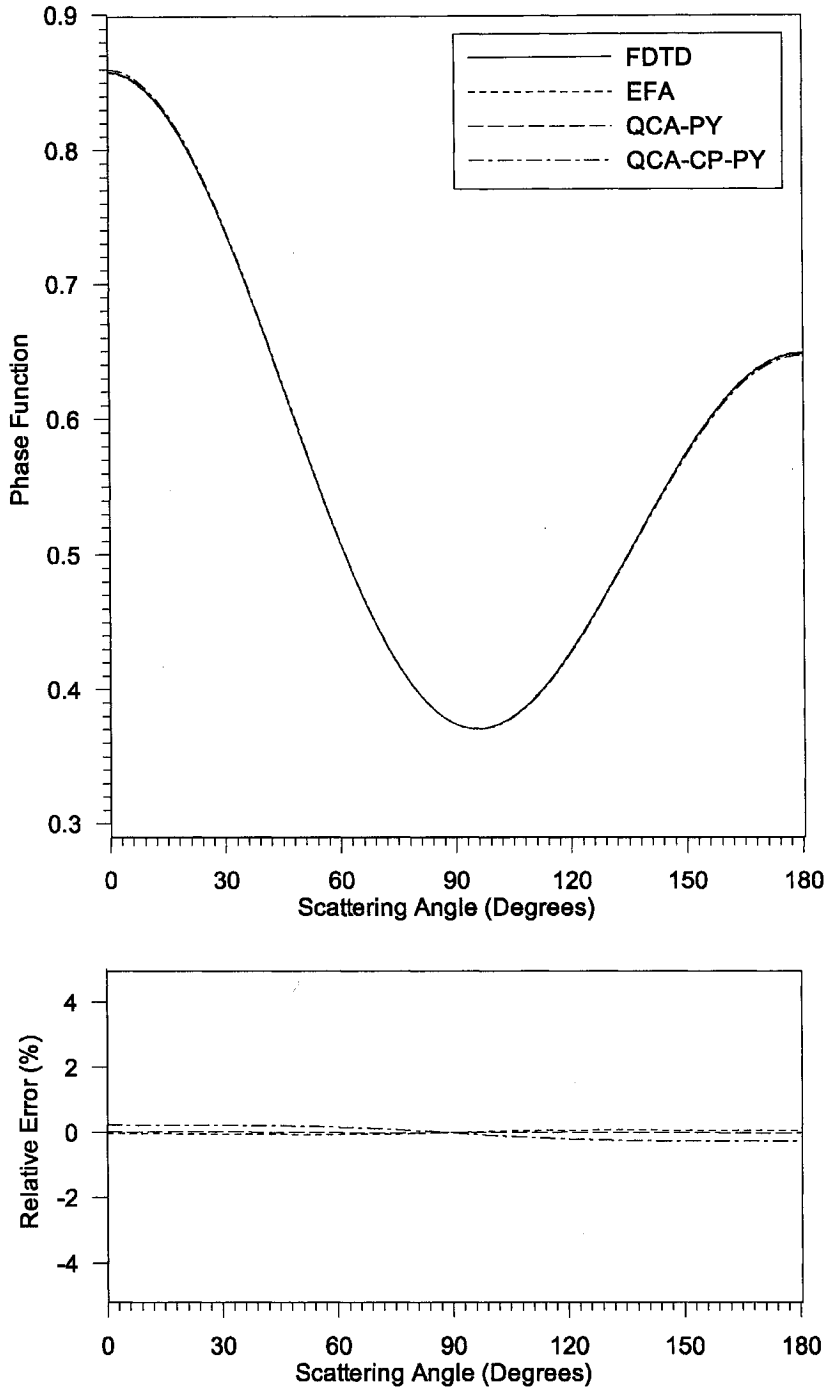

Figure 6.5: The same as Fig. 6.1 except the effective refractive indices are obtained from multiple scattering mixing rules (effective field approximation (EFA), quasi-crystalline approximation (QCA) with Percus-Yevick (PY) pair distribution, and QCA with coherent potential and Percus-Yevick pair distribution (QCA-CP-PY)).

Table 6.5: The same as Table 6.2, except the size parameter of host ice sphere is 0.25.

	Effective Refractive Indices		Scattering Properties				Relative Error (%)			
	mr	mi	Qext	Qsca	Qabs	g	δQ_{ext}	δQ_{sca}	δQ_{abs}	δg
Mean of FDTD results			0.0081	0.0022	0.0059	0.0145	1.7	0.2	2.2	0.3
Std deviation of FDTD results			0.0001	0.0000	0.0001	0.0000				
M1	1.79134	0.01416	0.0078	0.0019	0.0059	0.0142	-3	-14	0.7	-2
M2	1.78547	0.00535	0.0041	0.0019	0.0022	0.0142	-49	-15	-62	-2
M3	1.87484	0.01476	0.0080	0.0022	0.0058	0.0148	-1	-1	-1	2
M1&3	1.59757	0.01588	0.0089	0.0012	0.0076	0.0129	10	-45	30	-11
$< \varepsilon >$	2.18011	0.35219	0.1112	0.0036	0.1076	0.0171	1273	62	1732	18
$< m >$	1.97838	0.10927	0.0421	0.0026	0.0395	0.0156	420	18	573	7
$< \varepsilon^{1/3} >$	1.93682	0.07083	0.0289	0.0025	0.0265	0.0153	257	10	351	5
BR	1.87352	0.01400	0.0077	0.0022	0.0055	0.0148	-5	-1	-6	2
MG	1.86834	0.01212	0.0070	0.0022	0.0048	0.0148	-14	-2	-19	2
IMG	2.06274	0.25230	0.0880	0.0031	0.0850	0.0162	987	37	1347	12
EBR	1.87356	0.01402	0.0077	0.0022	0.0055	0.0148	-5	-1	-6	2
UEBR	1.87356	0.01402	0.0077	0.0022	0.0055	0.0148	-5	-1	-6	2
EMG	1.86836	0.01213	0.0070	0.0022	0.0048	0.0148	-14	-2	-19	2
UEMG	1.86834	0.01212	0.0070	0.0022	0.0048	0.0148	-14	-2	-19	2
EnBR	1.79788	0.01203	0.0069	0.0019	0.0050	0.0143	-14	-13	-15	-2
EnMG	1.79773	0.01195	0.0069	0.0019	0.0050	0.0143	-15	-13	-15	-2
EFA	1.86554	0.01151	0.0067	0.0022	0.0045	0.0148	-17	-2	-23	2
QCA	1.86834	0.01212	0.0070	0.0022	0.0048	0.0148	-14	-2	-19	2
QCACPPY	1.87628	0.01511	0.0081	0.0022	0.0059	0.0148	0.4	-0.4	0.7	2.1

Table 6.6: The same as Table 6.3, except the size parameter of host ice sphere is 0.25.

	Effective Refractive Indices		Scattering Properties				Relative Error (%)			
	mr	mi	Qext	Qsca	Qabs	g	dQ_{ext}	dQ_{sca}	dQ_{abs}	dg
Mean of FDTD results			0.0156	0.0026	0.0130	0.0152	3	0.2	3	0.6
Std deviation of FDTD results			0.0004	0.0000	0.0004	0.0001				
M1	1.80928	0.03243	0.0153	0.0020	0.0134	0.0144	-2	-25	3	-5
M2	1.79414	0.01001	0.0061	0.0019	0.0042	0.0142	-61	-28	-68	-6
M3	1.98641	0.03574	0.0155	0.0026	0.0129	0.0157	-1	-1	-1	3
M1&3	1.59888	0.03669	0.0189	0.0012	0.0176	0.0129	21	-53	36	-15
$< \varepsilon >$	2.54021	0.60285	0.1419	0.0051	0.1368	0.0201	809	93	955	32
$< m >$	2.17676	0.21615	0.0702	0.0034	0.0668	0.0172	350	29	415	14
$< \varepsilon^{1/3} >$	2.09725	0.14297	0.0502	0.0031	0.0471	0.0166	222	16	263	9
BR	1.98034	0.03100	0.0138	0.0026	0.0112	0.0157	-12	-2	-14	3
MG	1.95844	0.02226	0.0107	0.0025	0.0082	0.0155	-31	-5	-37	2
IMG	2.33248	0.45001	0.1255	0.0042	0.1213	0.0183	704	61	836	21
EBR	1.98042	0.03105	0.0138	0.0026	0.0112	0.0157	-11	-2	-13	3
UEBR	1.98042	0.03105	0.0138	0.0026	0.0112	0.0157	-11	-2	-13	3
EMG	1.95847	0.02229	0.0107	0.0025	0.0082	0.0155	-31	-5	-37	2
UEMG	1.95847	0.02230	0.0107	0.0025	0.0082	0.0155	-31	-5	-37	2
EnBR	1.81673	0.02219	0.0111	0.0020	0.0091	0.0144	-29	-24	-30	-5
EnMG	1.81555	0.02155	0.0108	0.0020	0.0088	0.0144	-31	-25	-32	-5
EFA	1.94735	0.01986	0.0098	0.0025	0.0074	0.0154	-37	-6	-43	1
QCA	1.95843	0.02226	0.0107	0.0025	0.0082	0.0155	-31	-5	-37	2
QCACPPY	1.99258	0.03693	0.0159	0.0026	0.0132	0.0158	2	0	2	4

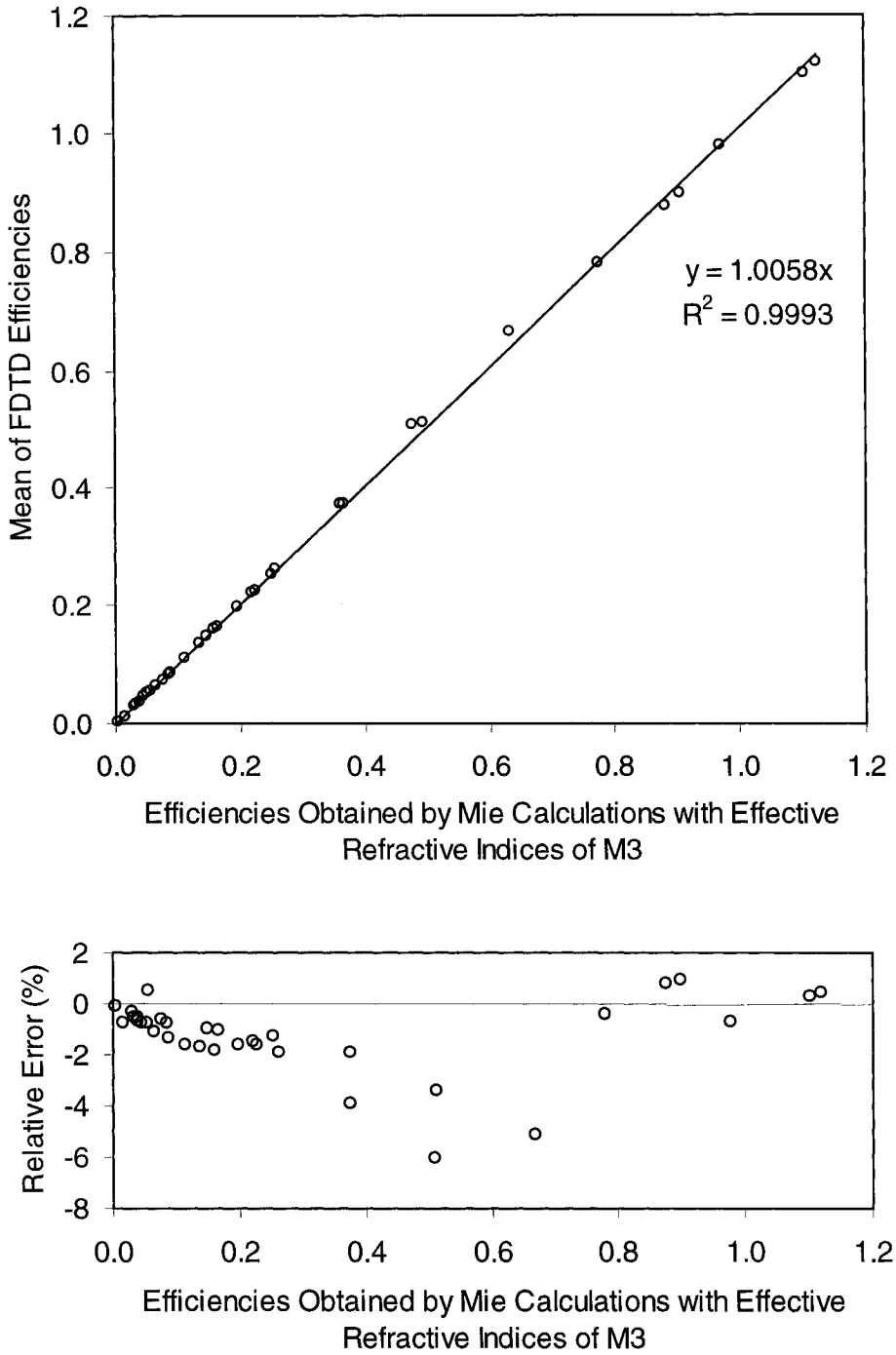

Figure 6.6: Mean of FDTD efficiencies of an ice sphere ($x_{ice} = 0.5$) with multiple spherical water inclusions ($x_w = 0.00974$) are compared to efficiencies obtained by Mie calculations with effective refractive indices of the numerical method 3 (M3) (see Figs. 6.7 and 6.8).

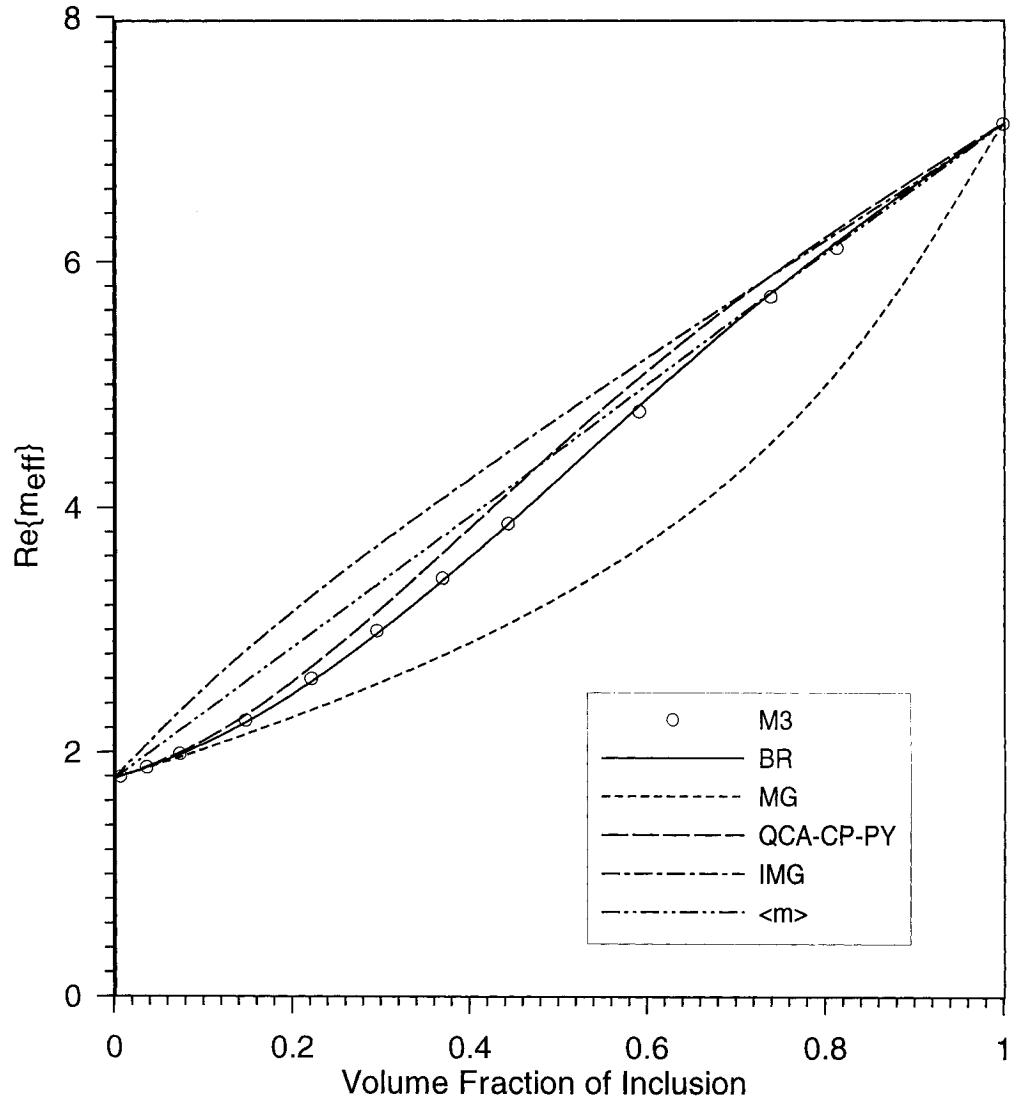

Figure 6.7: Real part of effective refractive indices obtained by the numerical method 3 (M3), the Bruggeman (BR), the Maxwell-Garnett (MG), and the quasi-crystalline approximation with coherent potential and Percus-Yevick pair distribution (QCACPPY) mixing rules as a function of the volume fraction of water inclusions. The size parameters of host and inclusion are 0.5 and 0.00974 respectively. Note that results of M3 are considered the accurate results.

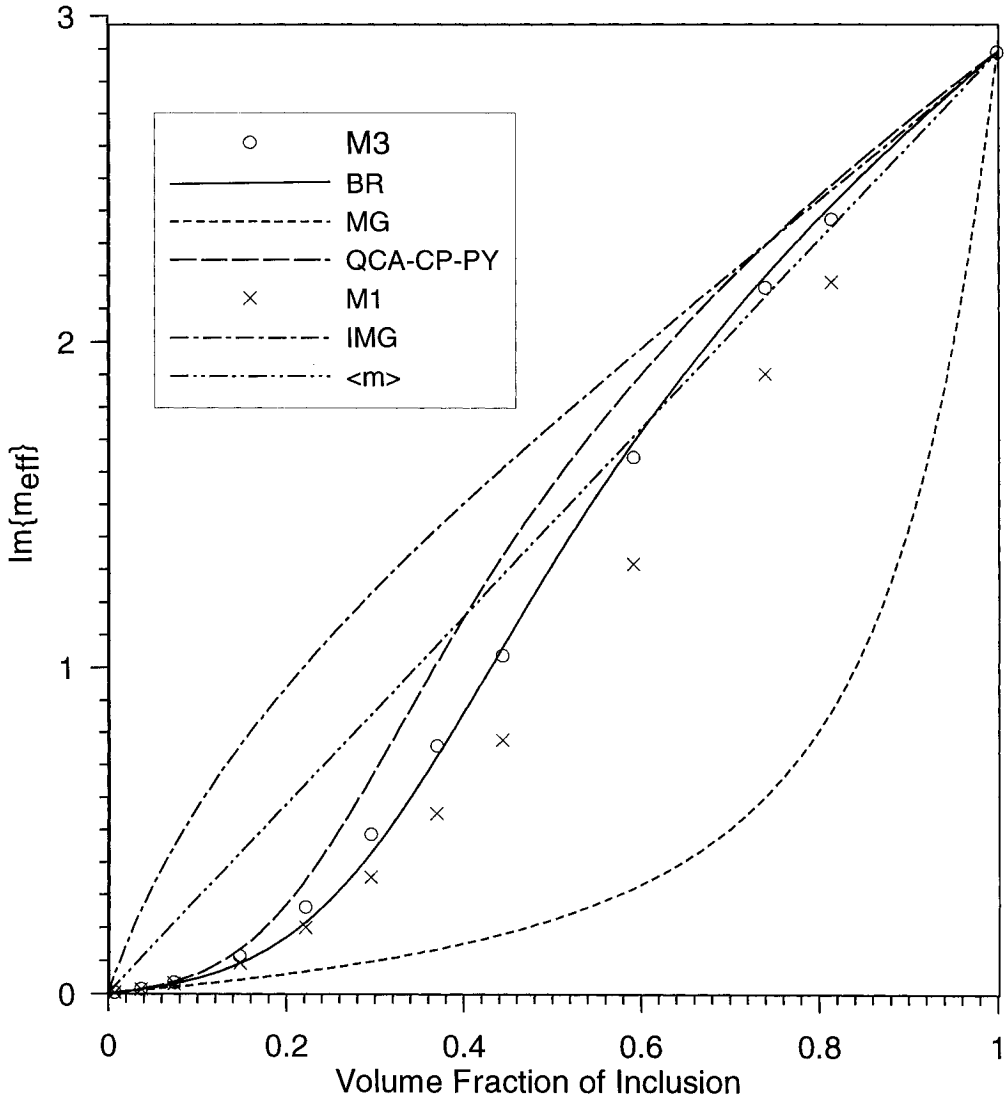

Figure 6.8: The same as Fig. 6.7 except that this is for imaginary part of effective refractive indices and the effective refractive indices obtained from the numerical method 1 (M1) are added.

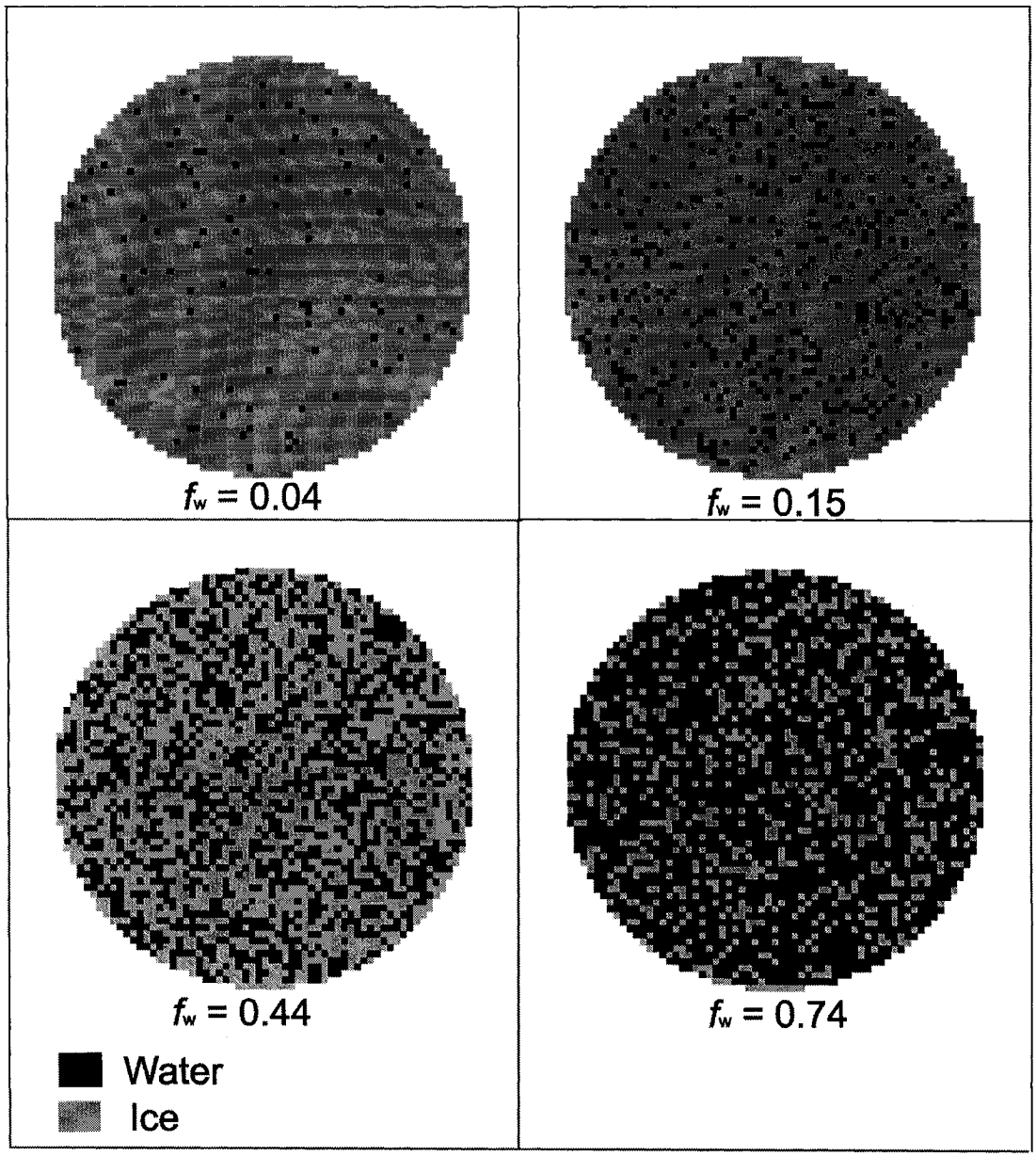

Figure 6.9: cross-sectional cuts through an ice sphere (in light grey, $x_{ice} = 0.5$) with multiple very small spherical water inclusions (in black color, $x_w = 0.00974$) for four volume fractions of the inclusion ($f_w = 0.04$, $f_w = 0.15$, $f_w = 0.44$ and $f_w = 0.74$)

We can note in Fig. 6.7 and 6.8 that the real and imaginary parts of the effective refractive indices obtained from the Bruggeman mixing rule show a good agreement with the M3 results for all volume fractions of the water inclusion. The Maxwell-Garnett and the QCA-CP-PY mixing rules give accurate results only for volume fractions less than 0.05. The M1 was previously shown to give accurate approximation of the absorption efficiency. Because the absorption a medium is related to the imaginary part of refractive index of the medium, we add the results for the M1 in Fig. 6.8. It is noted that the imaginary part refractive indices of the M1 are observed to be lower to those of the M3.

6.2 Case B: Finite Size Inclusions

To study the effect of inclusion size, another FDTD simulations are performed for larger size parameter of inclusions. We use inclusion size parameter $x_w = 0.05$ and the host size parameter $x_{ice} = 0.5$. Here the approximation using small FDTD cube, as used for small spherical particle, cannot be used here. Therefore we use the "in or out" approach for assigning the dielectric properties in our FDTD method. It is shown in chapter 2 that the relative error in scattering properties of sphere for size 0.05 is about 5% for all efficiencies when the FDTD parameter $\lambda / \Delta s = 400$ is used. Due to limited computational resources the FDTD simulations with a higher FDTD resolution cannot be done here.

The results of the FDTD simulations are given in Tables 6.7 and 6.8. The previous findings for smaller inclusions are also noted here. The method M3 is found to provide the most accurate results for all efficiencies. As previously noted that the M1 gives accurate results only for absorption efficiencies. It is also shown that some improvements in efficiencies are observed when the extended EMAs are used. The extended Bruggeman mixing rule shows a better accuracy than the extended Maxwell-Garnett mixing rule.

Similar to the previous results, the M3 gives correct values of all efficiencies with relative errors less than about 6%. Therefore the M3 is also used here as a reference for testing the validity of analytical EMAs. The results are shown in Figs. 6.11 and 6.12. It is shown for low volume fraction (less than 10%) the Bruggeman and the Maxwell-Garnett

rules give accurate effective refractive indices. As the volume fraction increases, the accurate values of effective refractive indices obtained by using the method M3 are in between those of the Bruggeman and the Maxwell-Garnett. This is different from the previous finding for very small inclusions. This difference can be explained by considering the geometrical structure of the ice-water mixture. In the previous case the small spherical waters (approximated by small cubes) can fill up the space of the host sphere as seen in Fig. 6.9. This means that the water inclusions can also act as a host medium provided that the volume fraction is large ($f_w > 0.1$). Therefore there is no preference which of the materials is the host material. In other words we have an aggregate structure (or Bruggeman type structure). This is the reason why the Bruggeman mixing rule shows an agreement with the numerical results.

For the case of inclusion size parameter $x_w = 0.05$, we have finite size inclusions. This means that the water inclusions cannot fill up the host sphere. The cross-sectional cuts of the sphere with multiple spherical inclusions are shown in Fig. 6.10. The inclusions are all the same size. But because Fig. 6.10 is the cross-sectional cut, it seems that there are various sizes of inclusions. We note that the inclusions are well confined inside the host sphere. This implies that the spherical inclusions always be inside the host sphere. Therefore we can definitely say that the ice is the host and the water is the inclusion. In other words, we have a separated grain structure or Maxwell-Garnett type. However, when the volume fraction increases, the water inclusions start to aggregate. This is clearly seen in Fig. 6.10 that some spheres form an aggregate of two- or more-spheres. Therefore we have the Bruggeman type structure inside the host sphere. Therefore both Bruggeman and Maxwell-Garnett structures exist in the ice-water mixture. This is the reason why the numerical results for effective refractive indices of the M3 are in between those of the Bruggeman and the Maxwell-Garnett. A combination of the Bruggeman and Maxwell-Garnett model (BR&MG) would be appropriate for this case. If we assume that the probability of occurrence of the Bruggeman type structure is the same as the probability of Maxwell-Garnett type, then following the derivation in chapter 5, we can obtain the BR&MG mixing rule in the form of

$$f\frac{\varepsilon_i-\varepsilon_{eff}}{\varepsilon_i+2\varepsilon_{eff}}+(1-f)\frac{\varepsilon_h-\varepsilon_{eff}}{\varepsilon_h+2\varepsilon_{eff}}+\frac{(\varepsilon_h-\varepsilon_{eff})(\varepsilon_i+2\varepsilon_h)+f(2\varepsilon_h+\varepsilon_{eff})(\varepsilon_i-\varepsilon_h)}{(\varepsilon_h+2\varepsilon_{eff})(\varepsilon_i+2\varepsilon_h)+2f(2\varepsilon_h-\varepsilon_{eff})(\varepsilon_i-\varepsilon_h)}=0 \tag{6.4}$$

where ε_i and f are the dielectric constant and volume fraction of inclusion sphere respectively, ε_h is the dielectric constant of host sphere. A similar mixing rule is also given by Chýlek et al. (1991). It is shown in Fig. 6.11 that the BR&MG gives a good approximation for real part of refractive indices. However, it is shown in Fig. 6.12 that the BR&MG rule underestimates the imaginary part of refractive indices. This may be because the BR& MG rule does not include the size dependence of the inclusion. The BR&MG can be extended by using the extended Bruggeman and the extended Maxwell-Garnett rules (EBR&EMG). It is shown in Fig. 6.12 that an improvement is noted when the EBR&EMG is used.

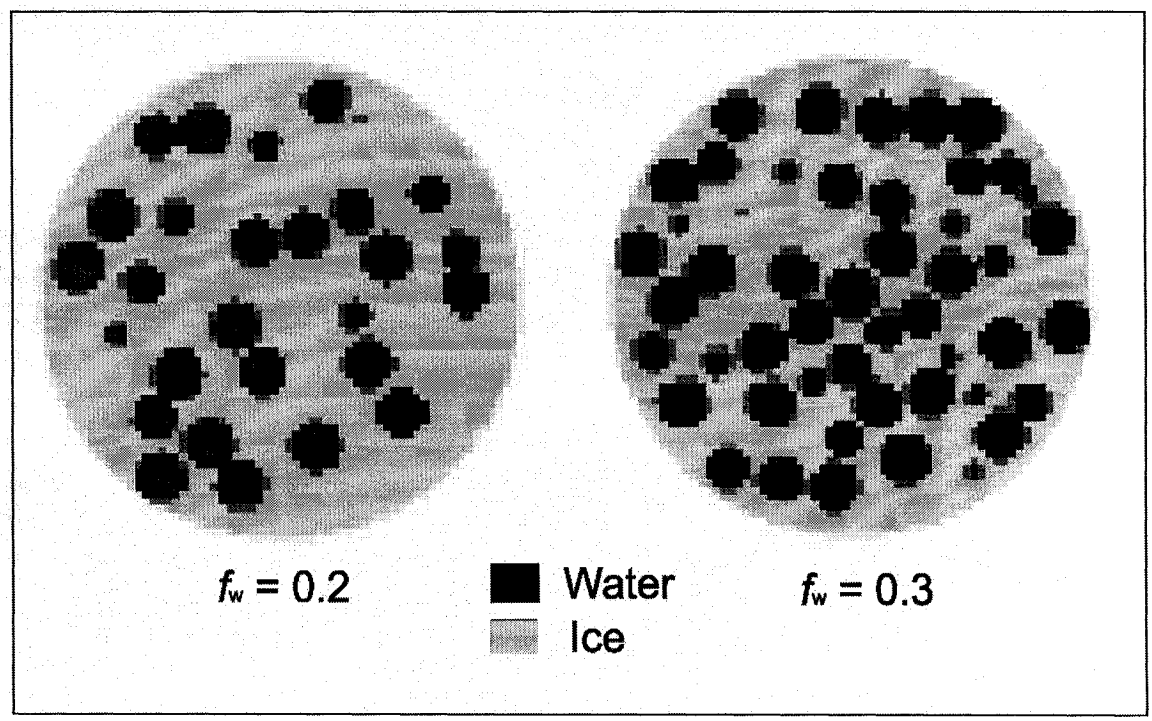

Figure 6.10: cross-sectional cuts through an ice sphere (in light grey, $x_{ice}=0.5$) with multiple spherical water inclusions (in black color, $x_w=0.05$) for two volume fractions of the inclusion ($f_w=0.2$ and $f_w=0.3$)

Table 6.7: The same as Table 6.2, except size parameter of inclusions $x_w = 0.05$ and the volume fraction of inclusions is 0.02.

	Effective Refractive Indices		Scattering Properties				Relative Error (%)			
	mr	mi	Qext	Qsca	Qabs	g	δQ_{ext}	δQ_{sca}	δQ_{abs}	δg
Mean of FDTD results			0.0439	0.0352	0.0087	0.0566	1	0	3	0
Std deviation of FDTD results			0.0003	0.0001	0.0002	0.0001				
M1	1.78616	0.00896	0.0402	0.0315	0.0087	0.0561	-8	-10	0.00	-1
M2	1.78287	0.00404	0.0352	0.0313	0.0039	0.0560	-20	-11	-55	-1
M3	1.83153	0.00944	0.0434	0.0344	0.0089	0.0574	-1	-2	3	1
M1&3	1.85419	0.00864	0.0440	0.0359	0.0080	0.0580	0	2	-7	3
$< \varepsilon >$	2.00025	0.20841	0.2233	0.0471	0.1761	0.0628	409	34	1928	11
$< m >$	1.88720	0.06015	0.0930	0.0382	0.0548	0.0592	112	8	531	5
$< \varepsilon^{1/3} >$	1.86429	0.03891	0.0726	0.0366	0.0360	0.0584	65	4	314	3
BR	1.82901	0.00812	0.0420	0.0343	0.0077	0.0573	-4	-3	-12	1
MG	1.82754	0.00760	0.0414	0.0342	0.0072	0.0573	-6	-3	-17	1
IMG	1.93376	0.14563	0.1703	0.0419	0.1285	0.0607	288	19	1379	7
EBR	1.82943	0.00841	0.0423	0.0343	0.0080	0.0573	-4	-2	-8	1
UEBR	1.82943	0.00841	0.0423	0.0343	0.0080	0.0573	-4	-2	-8	1
EMG	1.82782	0.00783	0.0416	0.0342	0.0074	0.0573	-5	-3	-15	1
UEMG	1.82782	0.00783	0.0416	0.0342	0.0074	0.0573	-5	-3	-15	1
EnBR	1.78998	0.00778	0.0393	0.0318	0.0075	0.0562	-10	-10	-13	-1
EnMG	1.79001	0.00779	0.0393	0.0318	0.0075	0.0562	-10	-10	-13	-1
EFA	1.82670	0.00749	0.0412	0.0341	0.0071	0.0572	-6	-3	-18	1
QCA	1.82752	0.00766	0.0414	0.0342	0.0073	0.0573	-6	-3	-16	1
QCACPPY	1.82976	0.00847	0.0423	0.0343	0.0080	0.0573	-3	-2	-8	1

Table 6.8: The same as Table 6.2, except size parameter of inclusions $x_w = 0.05$ and the volume fraction of inclusions is 0.04.

	Effective Refractive Indices		Scattering Properties				Relative Error (%)			
	mr	mi	Qext	Qsca	Qabs	g	δQ_{ext}	δQ_{sca}	δQ_{abs}	δg
Mean of FDTD results			0.0540	0.0388	0.0152	0.0573	1	0.3	4	1
Std deviation of FDTD results			0.0006	0.0001	0.0005	0.0006				
M1	1.79281	0.01582	0.0472	0.0319	0.0153	0.0563	-13	-18	0.2	-2
M2	1.78609	0.00577	0.0371	0.0315	0.0056	0.0560	-31	-19	-63	-2
M3	1.88415	0.01684	0.0533	0.0379	0.0154	0.0590	-1	-2	1	3
M1&3	1.94640	0.01457	0.0549	0.0420	0.0129	0.0609	2	8	-15	6
$< \varepsilon >$	2.21078	0.37520	0.3419	0.0643	0.2776	0.0696	533	66	1723	22
$< m >$	1.99440	0.11790	0.1463	0.0456	0.1007	0.0627	171	18	561	9
$< \varepsilon^{1/3} >$	1.94964	0.07652	0.1096	0.0424	0.0672	0.0612	103	9	342	7
BR	1.88163	0.01515	0.0516	0.0377	0.0139	0.0589	-4	-3	-9	3
MG	1.87554	0.01292	0.0492	0.0373	0.0119	0.0587	-9	-4	-22	2
IMG	2.08512	0.26986	0.2700	0.0538	0.2162	0.0655	400	39	1320	14
EBR	1.88252	0.01580	0.0523	0.0378	0.0145	0.0589	-3	-3	-5	3
UEBR	1.88252	0.01579	0.0523	0.0378	0.0145	0.0589	-3	-3	-5	3
EMG	1.87606	0.01337	0.0497	0.0374	0.0123	0.0587	-8	-4	-19	3
UEMG	1.87606	0.01336	0.0497	0.0374	0.0123	0.0587	-8	-4	-19	3
EnBR	1.80026	0.01331	0.0452	0.0324	0.0128	0.0565	-16	-16	-16	-1
EnMG	1.80006	0.01321	0.0451	0.0324	0.0127	0.0565	-16	-16	-17	-1
EFA	1.87225	0.01234	0.0485	0.0371	0.0114	0.0586	-10	-4	-25	2
QCA-PY	1.87552	0.01302	0.0493	0.0373	0.0120	0.0587	-9	-4	-21	2
QCA-CP-PY	1.88484	0.01660	0.0531	0.0379	0.0152	0.0590	-2	-2	-0.2	3

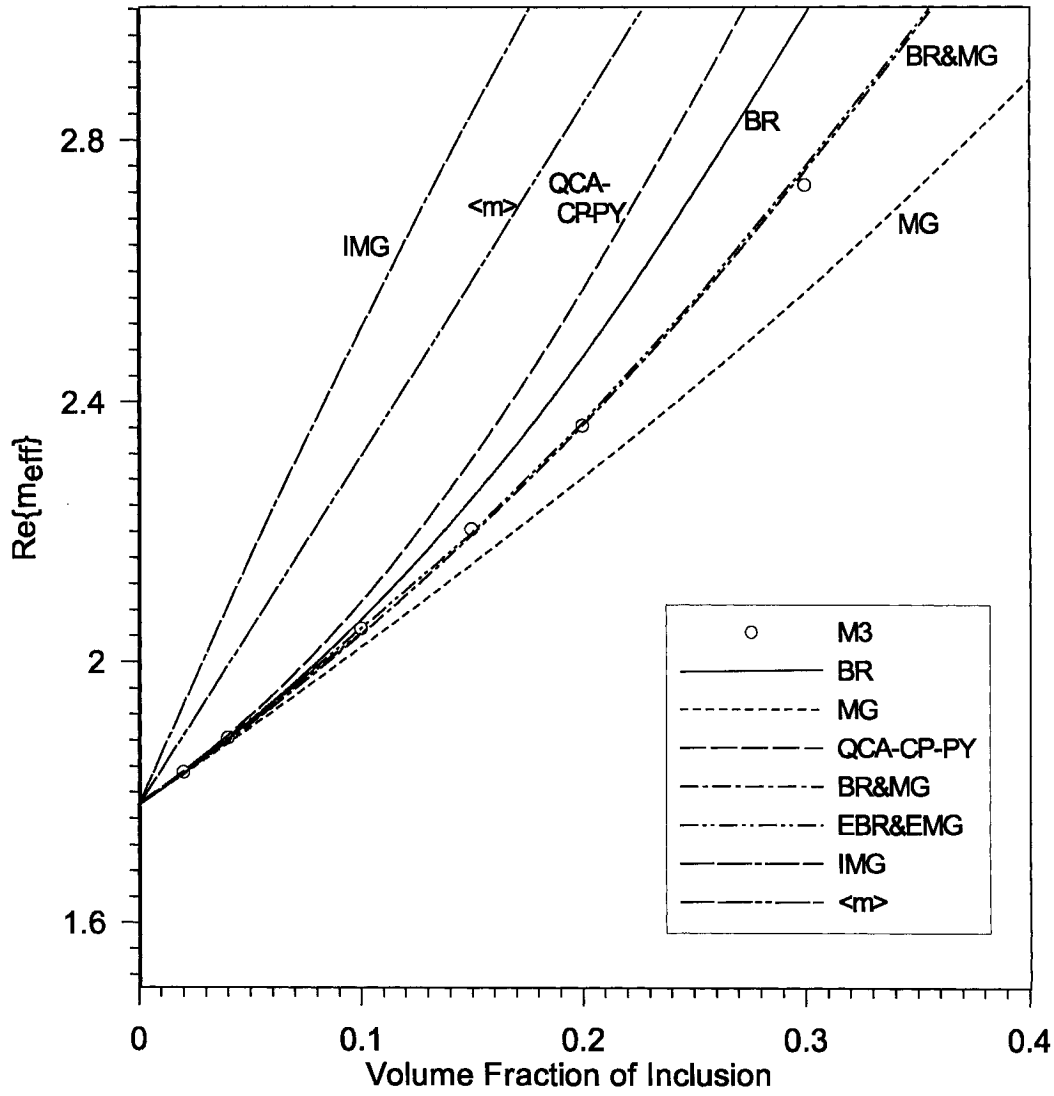

Figure 6.11: Real part of effective refractive indices obtained by the numerical method 3 (M3), the Bruggeman (BR), the Maxwell-Garnett (MG), and the quasi-crystalline approximation with coherent potential and Percus-Yevick pair distribution (QCACPPY), and a combination of BR and MG (BR&MG) mixing rules as a function of the volume fraction of water inclusions. The size parameters of host and inclusion are 0.5 and 0.05 respectively.

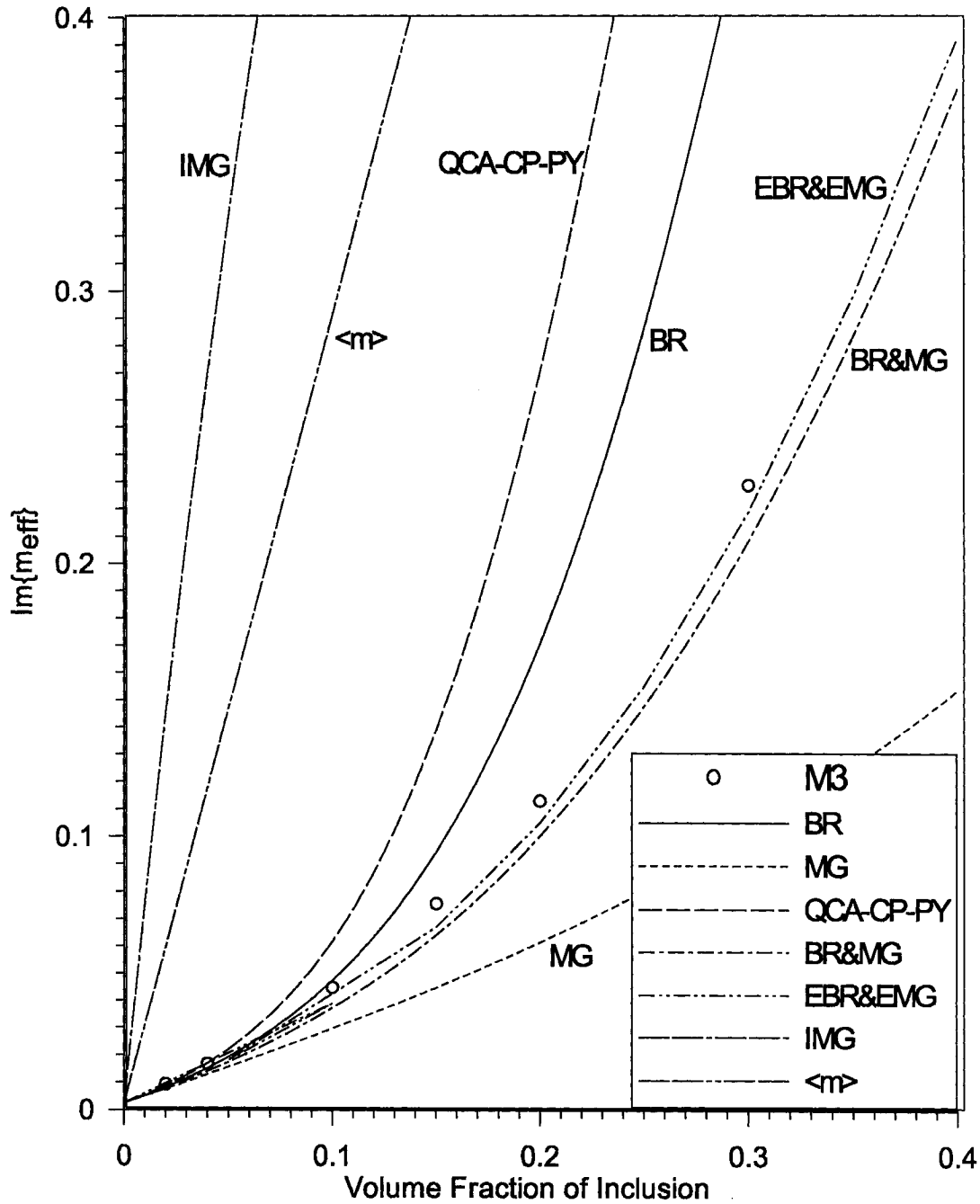

Figure 6.12: The same as Fig. 6.11 except that this is for the imaginary part of effective refractive indices.

6.3 Case C: Only One Inclusion

To consider further the effect of inclusion size we performed more simulations with inclusion size parameter 0.2 and 0.3. Only one water inclusion in the host ice sphere is considered here. The results are shown in Table 6.9 and 6.10. The results show that the M3 does not produce accurate results as for the very small inclusions. The Bruggeman and the extended Bruggeman and the Maxwell-Garnett mixing rules give large relative errors, larger than 10%. Here the extended Bruggeman does not show any improvement over the Bruggeman method. Instead, the extended Bruggeman worsen the relative errors. It is also found that the solution of effective refractive index of the uncorrected EBR, sometimes, can not be obtained using a numerical root finding.

The reason for the inability of extended Bruggeman can be explained since the topology of the particle is the Maxwell-Garnett type structure. This is the reason why the extended Maxwell-Garnett results show excellent agreements with the FDTD results for all efficiencies. Its relative errors are within the standard deviation for $x_w = 0.2$ and about 5% for $x_w = 0.3$. It is also shown that the results using the QCA-CP-PY are very close to the FDTD results for size parameter $x_w = 0.2$. This implies that the QCA-CP-PY is appropriate only for small size inclusions $x_w < 0.3$.

The absorbing medium correction of the extended MG does show an improvement in the efficiencies for size parameter $x_w = 0.3$. For a smaller size $x_w = 0.2$, the effect is negligible. This implies that the effect of absorbing medium is important only for large inclusions.

Table 6.9: The same as Table 6.2, except size parameter of inclusion is $x_w = 0.2$ and the volume fraction of inclusions is 0.064.

	Effective Refractive Indices		Scattering Properties				Relative Error (%)			
	mr	mi	Qext	Qsca	Qabs	g	dQ_{ext}	dQ_{sca}	dQ_{abs}	dg
Mean of FDTD results			0.0723	0.0426	0.0297	0.0576	2	1	4	1
Std deviation of FDTD results			0.0018	0.0005	0.0013	0.0004				
M1	1.80718	0.03042	0.0619	0.0329	0.0291	0.0567	-14	-23	-2	-2
M2	1.79306	0.00950	0.0411	0.0319	0.0092	0.0563	-43	-25	-69	-2
M3	1.94226	0.02875	0.0672	0.0418	0.0254	0.0608	-7	-2	-14	6
M1&3	1.95874	0.02807	0.0675	0.0429	0.0246	0.0614	-7	1	-17	7
$< \varepsilon >$	2.44681	0.54136	0.4309	0.0833	0.3477	0.0778	496	95	1072	35
$< m >$	2.12304	0.18721	0.2028	0.0549	0.1479	0.0672	180	29	399	17
$< \varepsilon^{1/3} >$	2.05345	0.12308	0.1512	0.0496	0.1016	0.0647	109	16	243	12
BR	1.94998	0.02573	0.0650	0.0423	0.0227	0.0611	-10	-1	-24	6
MG	1.93384	0.01946	0.0585	0.0412	0.0173	0.0606	-19	-3	-42	5
IMG	2.26105	0.40027	0.3556	0.0681	0.2875	0.0714	392	60	869	24
EBR	1.97054	0.05578	0.0922	0.0437	0.0485	0.0618	27	2	64	7
UEBR	1.97085	0.05498	0.0915	0.0437	0.0478	0.0618	27	3	61	7
EMG	1.94560	0.03450	0.0724	0.0420	0.0305	0.0610	0	-2	3	6
UEMG	1.94576	0.03368	0.0717	0.0420	0.0297	0.0610	-1	-1	0	6
EnBR	1.84335	0.03653	0.0694	0.0352	0.0342	0.0578	-4	-17	15	0
EnMG	1.84002	0.03474	0.0676	0.0350	0.0326	0.0577	-7	-18	10	0
EFA	1.92485	0.02094	0.0593	0.0406	0.0187	0.0603	-18	-5	-37	5
QCA	1.93335	0.02167	0.0605	0.0412	0.0193	0.0605	-16	-3	-35	5
QCACPPY	1.95746	0.03352	0.0722	0.0428	0.0294	0.0613	0	0	-1	6

Table 6.10: The same as Table 6.2, except size parameter of inclusion is $x_w = 0.3$ and the volume fraction of inclusions is 0.216.

	Effective Refractive Indices		Scattering Properties				Relative Error (%)			
	mr	mi	Qext	Qsca	Qabs	g	dQ_{ext}	dQ_{sca}	dQ_{abs}	dg
Mean of FDTD results			0.2386	0.0741	0.1644	0.0638	2	2	2	1
Std deviation of FDTD results			0.0048	0.0016	0.0032	0.0007				
M1	1.95383	0.16825	0.1899	0.0435	0.1465	0.0613	-20	-41	-11	-4
M2	1.86430	0.04781	0.0808	0.0366	0.0442	0.0584	-66	-51	-73	-8
M3	2.36324	0.15148	0.1756	0.0701	0.1055	0.0770	-26	-5	-36	21
M1&3	3.20679	0.10251	0.1707	0.1176	0.0531	0.1280	-28	59	-68	101
$<\varepsilon>$	3.63303	1.22774	0.6752	0.1530	0.5222	0.1168	183	106	218	83
$<m>$	2.93776	0.62612	0.4387	0.1109	0.3277	0.1019	84	50	99	60
$<\varepsilon^{1/3}>$	2.74517	0.45180	0.3552	0.0972	0.2580	0.0940	49	31	57	47
BR	2.54508	0.20310	0.2109	0.0818	0.1291	0.0855	-12	10	-21	34
MG	2.32701	0.06744	0.1155	0.0674	0.0481	0.0754	-52	-9	-71	18
IMG	3.23638	0.99183	0.5892	0.1336	0.4556	0.1072	147	80	177	68
EBR	2.32147	0.63782	0.5099	0.0801	0.4299	0.0710	114	8	162	11
UEBR	NA	NA								
EMG	2.35507	0.22404	0.2262	0.0703	0.1559	0.0765	-5	-5	-5	20
UEMG	2.35951	0.20008	0.2095	0.0703	0.1391	0.0767	-12	-5	-15	20
EnBR	2.31918	0.29287	0.2755	0.0692	0.2063	0.0746	15	-7	26	17
EnMG	2.17980	0.21779	0.2254	0.0590	0.1663	0.0693	-6	-20	1	9
EFA	2.22960	0.06836	0.1124	0.0610	0.0514	0.0713	-53	-18	-69	12
QCA	2.32562	0.07320	0.1195	0.0673	0.0522	0.0753	-50	-9	-68	18
QCACPPY	2.62023	0.33916	0.2942	0.0881	0.2061	0.0885	23	19	25	39

6.4 Case D: Clustering Effect

Previous cases used randomly positioned inclusions. As the volume fraction increases, some of the inclusions start to form clusters. We next study the effect of spatial arrangement of the inclusions in the host sphere. To study the effect of clustering to the scattering properties, we consider a host sphere with two or more closely packed inclusion spheres of the same sizes, which are line up in the direction of Cartesian axes. Here the incident wave is in the direction of positive z-axis and it is polarized in x-axis and y-axis. We first consider a simple case of two spheres in contact, called a bisphere. The results for efficiencies of a spherical ice with water bisphere inclusions, which are aligned in the x-axis, z-axis and random alignment in x-, y-, z-axes are shown in Table 6.11. We do not show the results for the bispheres aligned in y-axis because the results

are same as those for bispheres aligned in x-axis. We show results here only for three numerical methods of effective medium approximations. The M2 and other analytical methods show errors larger than 20%, except for the bispheres aligned in z-axis. This shows that spatial arrangement of inclusions inside the host medium affects greatly the applicability of the EMAs.

We notice in Table 6.11 that the efficiencies are affected by the alignment of the bispheres. When the alignment is in the direction of polarization of incident wave, for example in x-axis, the efficiencies increase compared to the separated spheres case. A large increase is observed in the absorption and the extinction efficiencies. A small increase is found for scattering efficiency. But when the bispheres are aligned in the direction of propagation of the incident wave (z-axis), the efficiencies slightly decrease. This is mainly due to a shadowing effect in which a sphere in the shadow region of another strongly absorbing sphere absorbs less energy. For randomly oriented bispheres, the absorption and extinction efficiencies are larger than those of the separated spheres case.

The effect of N number of closely packed spheres (N-spheres) is summarized in Fig. 6.13. It is shown that for N-spheres aligned randomly and in x-axis, the efficiencies show a linear increase. For the alignment in z-axis, the efficiencies remain constant. Similar to previous findings in this chapter the numerical method M1 is only suitable for calculating the absorption efficiency and the method M3 has performed accurately for all efficiencies with relative errors generally less than 5%.

Table 6.11: Effective refractive indices of various effective medium approximations, and calculated efficiencies and asymmetry factors of a spherical ice ($m_{ice} = 1.78 + 0.0024i$, $x_{ice} = 0.5$) with two closely packed spherical water inclusions (or bispheres) aligned in x-axis, z-axis and random axis ($m_w = 7.14 + 2.89\,i$, size parameter $x_w = 0.05$, water volume fraction $f_w = 0.04$) obtained from an FDTD method and Mie theory with effective refractive indices of numerical method 1-3 (M1-3), method 1&3. Note that the incident wave is in the positive z direction.

	$m_{eff} = m_R + m_I i$		Q_{ext}	Q_{sca}	Q_{abs}	g	δQ_{ext} (%)	δQ_{sca} (%)	δQ_{abs} (%)	δg (%)
Separated spheres (from Table 6.8):			0.0540	0.0388	0.0152	0.0573				
Bispheres aligned in x-axis:										
Mean of FDTD results			0.0675	0.0405	0.0269	0.0573				
Standard deviation			0.0019	0.0003	0.0017	0.0006				
M1	1.80480	0.02803	0.0595	0.0327	0.0268	0.0566	-12	-19.3	-0.3	-1.1
M3	1.90391	0.02929	0.0657	0.0392	0.0265	0.0596	-2.6	-3.3	-1.6	4.1
M1&3	2.02121	0.02503	0.0682	0.0470	0.0212	0.0635	1.1	16.1	-21	10.8
Bispheres aligned in z-axis:										
Mean of FDTD results			0.0524	0.0385	0.0140	0.0573				
Standard deviation			0.0010	0.0001	0.0008	0.0003				
M1	1.79142	0.01439	0.0457	0.0318	0.0139	0.0562	-13	-17.2	-0.5	-1.9
M3	1.87567	0.01442	0.0506	0.0373	0.0133	0.0587	-3.5	-2.9	-5.0	2.5
M1&3	1.89780	0.01359	0.0512	0.0388	0.0123	0.0594	-2.4	0.9	-12	3.7
Aligned randomly:										
Mean of FDTD results			0.0635	0.0399	0.0236	0.0573				
Standard deviation			0.0017	0.0003	0.0014	0.0009				
M1	1.80134	0.02453	0.0560	0.0325	0.0235	0.0565	-12	-19	0	-1
M3	1.89580	0.02602	0.0623	0.0387	0.0237	0.0594	-2	-3	0	4
M1&3	2.00755	0.02201	0.0649	0.0461	0.0188	0.0630	2	16	-21	10

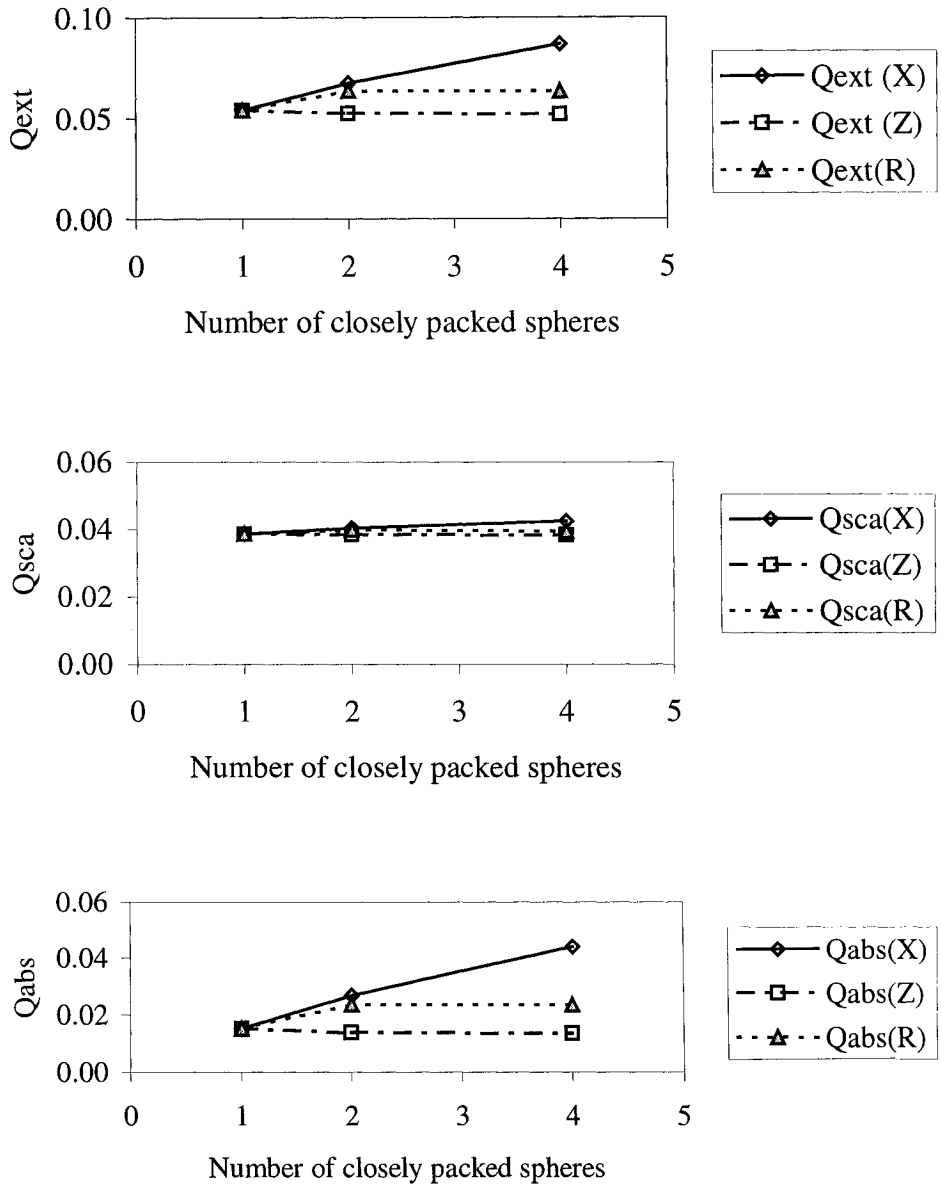

Figure 6.13: Efficiencies of a spherical ice particles ($x_{ice} = 0.5$) with N-closely packed spherical water inclusions ($x_w = 0.05$) for different number of N. Note that (X), (Y) and (Z) denotes the N-spheres aligned in x-axis, z-axis and random axis respectively. The volume fraction of inclusions is 0.04.

Chapter 7

Conclusions

The finite-difference time-domain (FDTD) method has been discussed and analyzed. The FDTD method is useful for solving light scattering by heterogeneous particles. A new absorbing boundary condition (ABC), which is called multiple absorbing surfaces (MAS), was also developed. The numerical results obtained from this computer program have shown good agreements with the Mie results.

The MAS method showed a comparable accuracy to the existing perfectly matched layer (PML) method. The MAS method is flexible, stable and efficient. Many long simulations have shown that the MAS method does not produce any instability. The MAS method uses computational resources comparable to the PML method. There are some advantages in using the MAS method over the PML method. The advantages include the application of the MAS method for various media such as lossy and dispersive medium and for various coordinate systems. The MAS method can also be used in combination with other ABCs in order to improve their performance.

The original formulation of the Mie theory can only be used for the case when the host medium is non-absorbing. It is of interest to consider the absorption of the medium. In this thesis, the reformulation of the Mie theory has been discussed and numerical results were given. It is shown that the effect of the absorbing host medium is significant

for large particles or for highly absorbing medium. For atmospheric applications, because of small size atmospheric particles and small absorption of the atmosphere, the effect is small and it can be neglected.

It is generally known that the large size limit of the extinction efficiency is two, however when the host medium is absorbing, the limit is found to be one. This reduction of extinction is due to the absence of diffraction at the edges of a sphere.

It was shown that the large size limit of the scattering efficiency approaches a reflectance of spherical surface for a non-absorbing medium. For absorbing medium, the scattering efficiency approaches a reflectance of a flat surface at perpendicular incidence.

To take account for the effect of the absorbing host medium, the effective medium approximation (EMA) is reformulated. The numerical results showed some reductions in relative errors of efficiencies obtained from the extended-EMA with the absorbing medium correction.

Using the FDTD method, various EMAs were tested. In this thesis, a composite particle was modeled by a spherical particle with multiple spherical inclusions. The numerical results showed the following findings:

- Numerical method 1 (M1), which is based on homogenization of internal energy $\varepsilon|\mathbf{E}|^2$, is generally good for calculating the absorption efficiency. ε is the permittivity of the medium, and $\mathbf{E}$ is the electric field in the medium.
- Numerical method 2 (M2), which is the average of refractive index weighted by the $|\mathbf{E}|^2$, gives relative errors in efficiencies larger than 15% for all the cases considered in this thesis.
- Numerical method 3 (M3), which is based on the extinction energy, generally approximates closely all efficiencies for small inclusions (size parameter much less than 1). Its relative errors are generally less than the standard deviation of the FDTD results. It can be considered the most accurate method for small inclusions.
- Numerical method 1 & 3 (a combination of M1 and M3) was constructed to minimize errors in all efficiencies. Because of numerical errors in the FDTD results, this method did not perform as expected.

- Volume average of dielectric constants, refractive indices and cube root of dielectric constants give large relative errors especially for absorption efficiencies. The relative errors are generally larger than 100% for extinction and absorption efficiencies. For the scattering efficiencies, the relative errors are larger than 15%.
- The Bruggeman and the Maxwell-Garnett Mixing rules showed good approximations for extinction and scattering efficiencies for inclusion size parameters less than 0.1. The Bruggeman mixing rule showed better results than the Maxwell-Garnett.
- The Inverted Maxwell-Garnett mixing rule produced the worst approximations for all efficiencies for small volume fraction of inclusions.
- The Bruggeman and the Maxwell-Garnet mixing rules can be improved by using the extended-EMA.
- The extended Bruggeman mixing rule showed better accuracy than the extended Maxwell-Garnett.
- Energy based EMAs do not show any improvement over the Bruggeman and the Maxwell-Garnett mixing rules.
- Of the multiple scattering approaches, the quasi-crystalline approximation with coherent potential with Percus-Yevick pair distribution (QCA-CP-PY) showed the best results. The QCA-CP-PY is shown to be more accurate than the Bruggeman method for a small volume fraction.
- The geometrical structure, the physical properties, and the arrangement of the inclusions are important to be considered for selecting appropriate EMAs for a particular problem. It was shown that when we have small inclusions (much smaller than the wavelength), the Bruggeman mixing rule and QCA-CP-PY should be used. For finite size inclusions (size parameter < 1), the QCA-CP-PY and the extended EMA should be employed for volume fraction less than 10%. For larger volume fraction a combination of the Bruggeman and the Maxwell-Garnett is appropriate. When there is only one particle in the host particle, the extended Maxwell-Garnett is suitable.

Examination of these findings leads to the conclusion that the selection of the most appropriate EMAs is highly dependent on the physical structure of the heterogeneous

particle. A set of rules can now be defined for selecting the most accurate EMAs for a given structure of particle. They are: (a) for very small inclusions it was shown that the Bruggeman mixing rule is in agreement with the FDTD results, (b) for finite size inclusions, a combination of the Bruggeman and the Maxwell-Garnett mixing rules was found to be appropriate, (c) for only one inclusion, it was shown that the extended Maxwell-Garnett rule is accurate. The spatial arrangement of the inclusions was also shown to be a determining factor for choosing the most appropriate EMAs. An increase in absorption was found when clusters of spheres are present in the structure.

In this thesis, a large difference in refractive index between the host and the inclusion materials was considered for testing the validity of various EMAs. We expect that the EMAs that showed good approximations for this case would be also appropriate for a smaller difference in refractive index. One such application of EMAs is for solving light scattering by a mixture of water and black carbon, and a mixture of black carbon and sulfate.

In this thesis, only spherical particles were considered for a scattering in an absorbing medium and for the EMAs. Further studies are needed to take account the effect of non-spherical shapes. A similar approach as given in this thesis may be used to reformulate the scattering by non-spherical particles in absorbing medium. To study the effect of non-spherical shapes of composite grains, the FDTD method may also be used.

It has been shown that the FDTD method has an inherent numerical error, which is mainly due to the staircasing approximation of a curved boundary. This error becomes large when the FDTD method is used to approximate a small particle. To overcome this problem some other methods that may be appropriate for small particles are a conformal mesh method, a subgridding method and a finite-volume method (Taflove, 1995; White et al., 2001; Yee and Chen, 1997).

Bibliography

Abeles, B., and J. I. Gittleman (1976). Composite material films: optical properties and applications. *Appl. Opt.* 15(10), 2328-2332.

Acquista, C., A. Cohen, J.A. Cooney, and J. Wimp (1980, August). Asymptotic behavior of the efficiencies in Mie scattering. *J. Opt. Soc. Am.* 70 (8), 1023-1025.

Aden, A. L., and M. Kerker (1951). Scattering of electromagnetic waves from two concentric spheres. *J. Appl. Phys.* 22(10), 1242-1246.

Ahrens, C. D. (1998). Essentials of meteorology: an invitation to the atmosphere. Belmont, California: Wadsworth Publishing Company.

Ao, C. O., and J. A. Kong (2002). Analytical approximations in multiple scattering of electromagnetic waves by aligned dielectric spheroids. *J. Opt. Soc. Am. A* 19(6), 1145-1156.

Asano, S., and G. Yamamoto (1975). Light scattering by a spheroidal particle. *J. Appl. Opt.* 14 (1),29-49.

Baran, A. J., P. Yang, and S. Havemann (2001). Calculation of the single-scattering properties of randomly oriented hexagonal ice columns: a comparison of the T-matrix and the finite-difference time-domain methods. *Appl. Opt.* 40(24), 4376-4386.

Berenger, J.-P. (1994). A perfectly matched layer for the absorption of electromagnetic waves. *J. Computat. Phys.* 114, 185-200.

Berenger, J.-P. (1996). Three-dimensional perfectly matched layer for the absorption of electromagnetic waves. *J. Computat. Phys.* 127, 363-379.

Bohren, C. F. (1986). Applicability of effective-medium theories to problems of scattering and absorption by nonhomogeneous atmospheric particles. *J. Atmos. Sci.* 43(5), 468-475.

Bohren, C. F., and B.M. Herman (1979, November). Asymptotic scattering efficiency of a large sphere. *J. Opt. Soc. Am.* 69(11), 1615-1616.

Bohren, C. F., and D. R. Huffman (1983). *Absorption and scattering of light by small particles*. New York: Wiley.

Bohren, C. F., and D. P. Gilra (1979). Extinction by a spherical particle in an absorbing medium. *J. Colloid interface Sci.* 72(2), 215-221.

Bohren, C. F., and L. J. Battan (1980). Radar backscattering by inhomogeneous precipitation particles. *J. Atmos. Sci.* 37, 1821-1827.

Borghese, F., P. Denti, R. Saija, and O. I. Sindoni (1992). Optical properties of spheres containing a spherical eccentric inclusion. *J. Opt. Soc. Am. A* 9(8), 1327-1335.

Bourrely, C., T. Lemaire, and P. Chiappetta (1991). A vectorial description of electromagnetic scattering by large bodies of spherical shape. *J. Mod. Opt.* 38(2), 305-315.

Bruscaglioni, P., A. Ismaeli, and G. Zaccanti (1993). A note on the definition of scattering cross sections and phase functions for spheres immersed in an absorbing medium. *Waves Random Media.* 3, 147-159.

Busch, K., and C.M. Soukoulis (1995). Transport properties of random media: An new effective medium theory. *Phys. Rev. Lett.* 75(19), 3442-3445.

Busch, K., and C.M. Soukoulis (1996). Transport properties of random media: An energy-density CPA approach. *Phys.Rev. B.* 54(2), 893-899.

Chýlek, P. (1973). Large-sphere limits of the Mie-scattering functions. *J. Opt. Soc. Am.* 63(6), 699-706.

Chýlek, P. (1975). Asymptotic limits of the Mie-scattering characteristics. *J. Opt. Soc. Am.* 65(11), 1316-1318,

Chýlek, P. (1976). Partial-wave resonances and the ripple structure in the Mie normalized extinction cross section. *J. Opt. Soc. Am.* 66(33), 285-287.

Chýlek, P. (1977). Light scattering by small particles in an absorbing medium. *J. Opt. Soc. Am.* 67(4), 561-563.

Chýlek, P., and J. Zhan (1989). Interference structure of the Mie extinction cross section. *J. Opt. Soc. Am.* A 6(12), 1846-1851.

Chýlek, P., and V. Srivastava (1983). Dielectric constant of a composite inhomogenous medium. *Phys. Rev. B* 27(8), 5098-5105.

Chýlek, P., G. B. Lesins, G. Videen, J. G. D. Wong, R. G. Pinnick, D. Ngo, and J. D. Klett (1996). Black carbon and absorption of solar radiation by clouds. *J. Geophys. Res.* 101(D18), 23,365-23,371.

Chýlek, P., G. Videen, D. J. W. Geldart, J. S. Dobbie, and H. C. W. Tso (2000). Effective medium approximation for heterogeneous particles. In Mishchenko, M. I., Hovenier, J. W., and Travis, L.D. (Ed.), *Light scattering by nonspherical particles: theory, measurements, and applications*, Chapter 9, pp. 273-308. San Diego: Academic Press.

Chýlek, P., G. Videen, D. Ngo, R. G. Pinnick, and J. D. Klett (1995). Effect of black carbon on the optical properties and climate forcing of sulfate aerosols. *J. Geophys. Res.* 100(D8), 16,325-16,332.

Chýlek, P., R. G. Pinnick, and V. Srivastava (1991). Effect of topology of water-ice mixture on radar backscattering by Hailstones. *J. Appl. Meteorology* 30: 954-959.

Chýlek, P., V. Srivastava, R. G. Pinnick, and R. T. Wang (1988). Scattering of electromagnetic waves by composite spherical particles: experiment and effective medium approximations. *Appl. Opt.* 27(12), 2396-2404.

Deirmendjian, D. (1969). *Electromagnetic scattering on spherical polydispersions.* pp. 34-37. New York: Elsevier,

Doicu, A. and Wriedth, T. (2001). Equivalent refractive index of a sphere with multiple spherical inclusions. *J. Opt. A: Pure Appl. Opt.* 3, 204-209.

Draine, B. T. (2000). The discrete dipole approximation for light scattering by irregular targets. In Mishchenko, M. I., Hovenier, J. W., and Travis, L.D. (Ed.), *Light scattering by nonspherical particles: theory, measurements, and applications*, Chapter 5, pp. 131-145. San Diego: Academic Press.

Engquist, B., and A. Majda (1977). Absorbing boundary conditions for numerical simulation of waves. *Math. Comp.* 31(139), 629-651.

Fang, J. (1994). Absorbing boundary conditions applied to model wave propagation in microwave integrated-circuit. *IEEE Trans. Microwave Theory Tech.* 42(8), 1506-1513.

Fang, J., and Z. Wu (1996). Closed-form expression of numerical reflection coefficient at PML interfaces and optimization of PML performance. *IEEE Microwave and Guided Wave Letters.* 6(9), 332-334.

Fikioris, J. G., and N. K. Uzunoglu (1979,Oct). Scattering from an eccentrically stratified dielectric sphere. *J. Opt. Soc. Am.* 69(10), 1359-1366.

Fu, Q., and W. Sun (2001). Mie theory for light scattering by a spherical particle in an absorbing medium. *Appl. Opt.* 40(9), 1354-1361.

Fujiki, N. M., D. J. W. Geldart, and P. Chýlek (1994). Effect of air bubbles on radar backscattering by hailstones. *J. Appl. Meteorol.* 33, 304-308.

Fuller, K. A. (1995). Scattering and absorption cross sections of compounded spheres. III. Spheres containing arbitrarily located spherical inhomogeneities. *J. Opt. Soc. Am. A* 12(5), 893-904.

Fuller, K. A., and D. W. Mackowski (2000). Electromagnetic scattering by compounded spherical particles. In Mishchenko, M. I., Hovenier, J. W., and Travis, L.D. (Ed.), *Light scattering by nonspherical particles: theory, measurements, and applications*, Chapter 8, pp. 225-272. San Diego: Academic Press.

Gedney, S. D. (1998). The perfectly matched layer absorbing medium. In A. Taflove, (Ed.), *Advances in computational electrodynamics: the finite-difference time-domain method.* Chapter 5, pp. 263-343. Boston: Artech House.

Griffiths, D.J. (1981). *Introduction to electrodynamics.* New Jersey: Prentice-Hall.

Harrington, R. F. (1961). *Time-harmonic electromagnetic fields.* New York: McGraw-Hill.

Haywood J., O. Boucher (2000). Estimates of the direct and indirect radiative forcing due to tropospheric aerosols: A review. *Rev. Geophys.* 38 (4): 513-543.

Haywood, J. M., D. L. Roberts, A. Slingo, J. M. Edwards and K. P. Shine (1997a). General circulation model calculations of the direct radiative forcing by anthropogenic sulfate and fossil-fuel soot aerosol. *J. Clim.* 10: 1562–1577.

Herman, M. (1962). Infra-red absorption, scattering, and total attenuation cross-sections for water spheres. *Quart. J. R. Meteorol. Soc.* 88, 143-150.

Higdon, R. L. (1986). Absorbing boundary conditions for difference approximations to the multi-dimensional wave equation. *Math. Comp.* 47(176), 437-459.

Higdon, R. L. (1987). Numerical absorbing boundary conditions for the wave equation. *Math. Comp.* 49(179), 65-90.

Holland, R., and J. W. Williams (1983). Total-field versus scattered-field finite-difference codes: a comparative assessment. *IEEE Trans. Nuclear Sci.* NS-30(6), 4583-4588.

Horvath, H. (1993). Atmospheric light-absorption – a review. *Atmos. Environment* 27A(3), 293-317.

Ioannidou, M. P., and D. P. Chrissoulidis (2002). Electromagnetic-wave scattering by a sphere with multiple spherical inclusions. *J. Opt. Soc. Am. A* 19(3), 505-512.

Jacobson, M. Z. (2000). A physically-based treatment of elemental carbon optics: Implications for global direct forcing of aerosols. *Geophys. Res. Lett.* 27: 217-220.

Jacobson M. Z. (2001). Strong radiative heating due to the mixing state of black carbon in atmospheric aerosols. *Nature.* 409 (6821): 695-697.

Jackson, J.D. (1999). *Classical electrodynamics* (Third ed.). New York: Wiley.

Juntunen, J. S., N.V. Kantartzis, and T.D. Tsiboukis (2001). Zero reflection coefficient in discretized PML. *IEEE Microwave and Wireless Components Letters.* 11(4),155-157.

Kahnert, F. M., J. J. Stamnes, and K. Stamnes (2001). Application of the boundary condition method to homogeneous particles with point-group symmetries. *Appl. Opt.* 40(18), 3110-3123.

Kantartzis, N. V., and T. D. Tsiboukis (1997). A comparative study of the Berenger perfectly matched layer, the superabsorption technique and several higher-order ABC's for the FDTD algorithm in two and three dimensional problems. IEEE Trans. Magnetics. 33(2), 1460-1463.

Kärkkäinen, K. K., A. H. Sihvola, and K. I. Nikoskinen (2000). Effective permittivity of mixtures: numerical validation by the FDTD method. *IEEE Trans. Geoscience Remote Sensing.* 38(3),1303-1308.

Kärkkäinen, K., A. Sihvola, and K. Nikoskinen (2001). Analysis of a three-dimensional dielectric mixture with finite difference method. *IEEE Trans. Geoscience and Remote Sensing.* 39(5): 1013-1018.

Kirchner, A., K. Busch and C. M. Soukoulis (1998). Transport properties of random arrays of dielectric cylinders. *Phys. Rev.* 57(1): 277-288.

Katz, D. S., E. T. Thiele, and A. Taflove (1994) Validation and extension to three dimensions of the Berenger PML absorbing boundary condition for FD-TD meshes. *IEEE Trans. Microwave and Guided Lett.* 4(8), 268-270.

Kerker, M. (1969). *The scattering of light and other electromagnetic radiation.* New York: Academic Press,

Kiehl, J. T., and H. Rodhe (1994). Modelling geographical and seasonal forcing due to aerosols. In R. J. Charlson and J. Heintzenberg (Eds.). *Aerosol forcing of climate.* Chichester: Wiley & Sons.

Kolokolova, L., and B. Å.S. Gustafson (2001). Scattering by inhomogenous particles: microwave analog experiments and comparison to effective medium theories. *J. Quant. Spect. Rad. Transfer.* 70, 611-625.

Landau, L. D., and E. M. Lifshitz (1960). *Electrodynamics of continuous media.* pp. 26-27. Oxford: Pergamon Press.

Lebedev, A.N., M. Gartz, U. Kreibig, and O. Stenzel (1999). Optical extinction by spherical particles in an absorbing medium: application to composite absorbing films. *J. Eur. Phys. D* 6, 365-373.

Lesins G, Chylek P, Lohmann U (2002). A study of internal and external mixing scenarios and its effect on aerosol optical properties and direct radiative forcing. *J. Geophys. Res. –Atmos.* 107 (D10): art. no. 4094

Liou, K.-N. (1980). An introduction to atmospheric radiation. San diego: Academic Press.

Macke, A., M. I. Mishchenko, and B. Cairns (1996). The influence of inclusions on light scattering by large ice particles. *J. Geophys. Res.* 101(D18), 23,311-23316.

Mackowski, D. W., and M. I. Mishchenko (1996). Calculation of the T matrix and the scattering matrix for ensembles of spheres. *J. Opt. Soc. Am. A* 13(11), 2266-2278.

Maloney, J. G., and G. S. Smith (1998). Modeling of Antennas. In A. Taflove (Ed.), *Advances in computational electrodynamics: the finite-difference time-domain method.* Chapter 7, pp.409-460.Boston: Artech House.

Merril, W. M., R. E. Diaz, M. M. LoRe, M. C. Squires, and N. G. Alexopoulos (1999). Effective medium theories for artificial materials composed of multiple sizes of spherical inclusions in a host continuum. *IEEE Trans. Antennas Propagation.* 47(1), 142-148.

Mie, G. (1908). Beiträge zur optik trüber medien, speziell kolloidaler metallösungen. *Ann. Phys.* 25, 377-445.

Mishchenko, M. I., and L. D. Travis (1998). Capabilities and limitations of a current fortran implementation of the T-matrix method for randomly oriented, rotationally symmetric scatterers. *J. Quant. Spectrosc. Radiat. Transfer* 60(3), 309-324.

Mishchenko, M. I., L. D. Travis, and A. A. Lacis (2002). Scattering, absorption, and emmision of light by small particles. Cambridge: Cambridge University Press.

Mishchenko, M. I., L. D. Travis, and A. Macke (2000). T-matrix method and its applications. In Mishchenko, M. I., Hovenier, J. W., and Travis, L.D. (Eds.), *Light*

scattering by nonspherical particles: theory, measurements, and applications, Chapter 6, pp.147-172. San Diego: Academic Press.

Mundy, W.C., J.A. Roux and A.M. Smith (1974). Mie scattering by spheres in an absorbing medium. *J. Opt. Soc. Am.* 64(12), 1593-1597.

Myhre, G., F. Stordal, K. Restad, and I. S. A. Isaksen (1998). Estimation of the direct radiative forcing due to sulfate and soot aerosols. *Tellus B* 50: 463-477.

Nanbu, Y., and M. Tateiba (1996). A comparative study of the effective dielectric constant of a medium containing randomly distributed dielectric spheres embedded in a homogeneous background medium. *Waves in Random Media.* 6: 347–360.

Niklasson, G. A., C. G. Granqvist, and O. Hunderi (1981). Effective medium models for the optical properties of inhomogenous materials. *Appl. Opt.* 20(1), 26-30.

Percus , J. K., and G. J. Yevick (1958).Analysis of classical statistical mechanics by means of collective coordinates. *Phys. Rev.* 110:1–13.

Perrin, J. –M., and P. L. Lamy (1990). On the validity of effective medium theories in the case of light extinction by inhomogeneous dust particles. Astrophys. J. 364:146-151.

Perrin, J.-M., and P. L. Lamy (1990). On the validity of the effective-medium theories in the case of light extinction by inhomogeneous dust particles. *Astrophys. J.* 364,146-151.

Prescott, D.T., and N.V. Shuley (1997). Reflection analysis of FDTD boundary conditions—Part I: time-space absorbing boundaries. *IEEE Trans. Microwave Theory Tech.* 45(8), 1162-1170.

Pruppacher, H. R., and J. D. Klett (1997*). Microphysics of clouds and precipitation.* Dordrecht; Boston: Kluwer Academic Publishers.

Quinten, M.,and J. Rostalski (1996). Lorenz-Mie theory for spheres immersed in an absorbing host medium. *Part. Part. Syst. Charact.* 13, 89-96.

Rengarajan, S. R. and Y. Rahmat-Samii (2000). The Field equivalence principle: Illustration of the establishment of the non-intuitive null fields. *IEEE Trans. Antennas and Propagation Magazine.* 42, 122-128.

Sadiku, M. N. O. (1992). Numerical techniques in electromagnetics. Publisher Boca Raton, FL : CRC Press, c1992.

Sareni, B., L. Krähenbühl, A. Beroual and C. Brosseau (1996). Effective dielectric constant of periodic composite materials. *J. Appl. Phys.* 80 (3): 1688-1696.

Seinfeld, J. H., and S. N. Pandis (1998). *Atmospheric chemistry and physics.* New York: Wiley & Sons.

Shlager, K. L., and J. B. Schneider (1998). A survey of the finite-difference time-domain literature. In A. Taflove (Ed.), *Advances in computational electrodynamics: the finite-difference time-domain method.* Chapter 1, pp. 1-62. Boston: Artech House.

Stephens, G. L. (1994). Remote sensing of the lower atmosphere. New York: Oxford University Press.

Stroud, D., and F. P. Pan (1978). Self-consistent approach to electromagnetic wave propagation in composite media: Application to model granular metals. *Phys. Rev. B* 17(4), 1602-1610.

Sudiarta, I. W., and P. Chýlek (2001a). Mie-scattering formalism for spherical particles embedded in an absorbing medium. *J. Opt. Soc. Am. A* 18(6): 1275-1278.

Sudiarta, I. W., and P. Chýlek (2001b). Mie scattering efficiency of a large spherical particle embedded in an absorbing medium. *J. Quant. Spectrosc. Radiat. Transfer* 70: 709-714.

Sudiarta, I.W. (2003a). Computer programs are provided at http://is2.dal.ca/~sudiarta or at http://fizz.phys.dal.ca/~wayan; a CD-ROM that contains computer programs used in this thesis can be found in the Dept. of Physics and Atmospheric Science, Dalhousie University, Halifax, Nova Scotia.

Sudiarta, I.W. (2003b). An absorbing boundary condition for FDTD truncation using multiple absorbing surfaces. *IEEE Trans. Antennas Propagat.*, accepted.

Sun, W., and Q. Fu (2000). Finite-difference time-domain solution of light scattering by dielectric particles with large complex refractive indices. *Appl. Opt.* 39(30), 5569-5578.

Sun, W., Q. Fu, and Z. Chen (1999). Finite-difference time-domain solution of light scattering by dielectric particles with a perfectly matched layer absorbing boundary condition. *Appl. Opt.* 38(15), 3141-3151.

Taflove, A. (1995). *Computational electrodynamics: the finite-difference time-domain method.* Boston: Artech House.

Trefethen, L. N., and L. Halpern (1986). Well-posedness of one-way wave equations and absorbing boundary conditions. *Math. Computat.* 47(176), 421-435.

Tsang, L., J. A. Kong and R. T. Shin (1985). *Theory of Microwave Remote Sensing.* New York: Wiley Interscience.

Tsang, L., and J. A. Kong (1980). Multiple scattering of electromagnetic waves by random distributions of discrete scatterers with coherent potential and quantum mechanical formulism. *J. Appl. Phys.* 51(7): 3465–3485.

Twersky, V. (1977). Coherent scalar field in pair-correlated random distributions of aligned scatterers. *J. Math. Phys.* 18: 2468–2486.

Twersky, V. (1978). Coherent electromagnetic waves in pair-correlated random distributions of aligned scatterers. *J. Math. Phys.* 19: 215–230.

van de Hulst, H. C. (1957). *Light scattering by small particles.* New York: Wiley & Sons.

Varadan, V. V., V. K. Varadan, Y. Ma, and W. A. Steele (1987). Effects of nonspherical statistics on EM wave propagation in discrete random media. *Radio Sci.* 22: 491–498.

Varadan, V. V., Y. Ma, and V. K. Varadan (1987). Anisotropic dielectric properties of media containing aligned nonspherical scatterers. *IEEE Trans. Antennas Propagation.* AP-33: 886–890.

Videen, G., D. Ngo, P. Chýlek, and R. G. Pinnick (1995). Light scattering from a sphere with an irregular inclusion. *J. Opt. Soc. Am. A* 12(5), 922-928.

White, M. J., Z. Yun and M. F. Iskander (2001). A new 3-D FDTD multigrid technique with dielectric traverse capabilities. *IEEE Trans. Microwave Theory Tech.* 49(3): 422-430.

Winton, S. C. and C. M. Rappaport (2000). Specifying PML conductivities by considering numerical reflection dependencies. *IEEE Trans. Antennas Propagat.* 48(7), 1055-1063.

Wiscombe, W. J. (1980). Improved Mie scattering algorithms. *Appl. Opt.* 19(9), 1505-1509.

Wu, F., and K. W. Whites (2001). Quasi-static effective permittivity of periodic composites containing complex shaped dielectric particles. *IEEE Trans. Antennas Propagation.* 49(8), 1174-1182.

Xu, Y.-L. (1995). Electromagnetic scattering by an aggregate of spheres. *Appl. Opt.* 34(21), 4573-4588.

Yang, P. and K. N. Liou (2000). Finite difference time domain method for light scattering by nonspherical and inhomogeneous particles. In M. I. Mishchenko, J. W. Hovenier and L. D. Travis (Ed.), *Light scattering by nonspherical particles: theory, measurements, and applications.* Chapter 7, pp. 173-221. San Diego: Academic Press.

Yang, P., and K. N. Liou (1996). Finite-difference time domain method for light scattering by small ice crystals in three-dimensional space. *J. Opt. Soc. Am. A* 13(10), 2072-2089.

Yang, P., K. N. Liou, M. I. Mishchenko, and B.-C. Gao (2000). Efficient finite-difference time-domain scheme for light scattering by dielectric particles: application to aerosols. *Appl. Opt.* 39(21), 3727-3737.

Yee, K.S. (1966). Numerical solution of initial boundary value problems involving Maxwell's equations in isotropic media. *IEEE Trans. Antennas and Propagation.* AP-14(3), 302-307.

Yee, K. S. and J. S. Chen (1997). The Finite-Difference Time-Domain (FDTD) and the Finite-Volume Time-Domain (FVTD) methods in solving Maxwell's equations. *IEEE Trans. Antennas and Propagation.* 45(3), 354-363.